Investigation of a Pressure Wave Supercharger for an Industrial Diesel Engine

THESIS

Brian A. Beasley, Capt, USAF

AFIT-ENY-MS-18-S-055

DEPARTMENT OF THE AIR FORCE
AIR UNIVERSITY

AIR FORCE INSTITUTE OF TECHNOLOGY

Wright-Patterson Air Force Base, Ohio

AFIT-ENY-MS-18-S-055

INVESTIGATION OF A PRESSURE WAVE SUPERCHARGER FOR AN INDUSTRIAL DIESEL ENGINE:

THESIS

Presented to the Faculty

Department of Aeronautics and Astronautics

Graduate School of Engineering and Management

Air Force Institute of Technology

Air University

Air Education and Training Command

in Partial Fulfillment of the Requirements for the

Degree of Master of Science in Aeronautical Engineering

Brian A. Beasley, BSAE

Capt, USAF

August 30, 2018

AFIT-ENY-MS-18-S-055

INVESTIGATION OF A PRESSURE WAVE SUPERCHARGER FOR AN INDUSTRIAL DIESEL ENGINE:

THESIS

Brian A. Beasley, BSAE
Capt, USAF

Committee Membership:

Dr. Marc D. Polanka
Chair

Dr. Fred R. Schauer
Member

Maj Levi M. Thomas, PhD
Member

Abstract

Internal combustion engines suffer from decreased performance as altitude is increased. This performance decrease can be overcome by increasing the pressure in the engine's intake manifold. Typically, this is accomplished with a turbocharger or supercharger. However, mechanical compression devices such as these suffer from decrease compression efficiency as the size of the device decreases. The size of the compression device scales with the amount of mass flow through the device, and the amount of mass flow is proportional to the size of the engine. This means a small turbocharger for a small engine is less efficient than a larger turbocharger coupled with a larger engine. An alternative means to compress fresh air sent to the engine is a wave rotor. The wave rotor avoids the efficiency loss of small mechanical compression devices by transferring energy from the exhaust gas to the fresh air by means of pressure waves. This research characterized the performance of a wave rotor sized for a 898cc industrial diesel engine. The wave rotor was initially tested while coupled to a burner instead of an engine in order to match and compare with previous testing. The results showed that the wave rotor had a maximum compression efficiency of 60% and that the efficiency depended on the exhaust temperature and rotor speed. The efficiency also depended heavily on the relationship between exhaust temperature and rotor speed since the rotor performance depends on the proper matching of these properties. Three different endwall configurations were also tested and compared. The results of the endwall comparison show that adding pockets to the endwalls increases the efficiency of the wave rotor at both on design and off design point conditions.

Acknowledgements

Thank you to everyone in D-Bay for all your support and advice. I greatly appreciate you allowing me to use your space and tools to do my research. Thank you to Dr. Dan Paxson for your instrumental work getting this project off the ground. You're advice, experience, and expertise that you shared were instrumental to this project's success. Thank you to my adviser Dr. Marc Polanka for all your guidance and support. Your patience with the many edits is immensely appreciated. Finally, thank you to my family for your continuous love and support. I couldn't have done it without any of you.

Brian A. Beasley

Table of Contents

Page

List of Figures

List of Symbols

List of Abbreviations

INVESTIGATION OF A PRESSURE WAVE SUPERCHARGER FOR AN INDUSTRIAL DIESEL ENGINE:

I. Introduction

1.1 General Issue

The demand for increased performance and efficiency from internal combustion engines has recently increased. Concerns about rising fuel costs and tightening emissions regulations while maintaining or increasing the engine's power are driving manufactures to research new methods of reaching performance, efficiency, and emissions goals. The technology of the engine itself has reached a level where the engine is about as good as it will get, so manufacturers are looking at alternate methods to meet their goals. These methods include precisely controlling the spark timing and fuel flow with sophisticated engine control software, adding turbochargers or superchargers to the engine, and developing alternate cycles such as a hybrid spark ignition/compression ignition cycle.

Precisely controlling the spark timing and fuel flow allows the engine control computer to minimize the fuel used to produce a given amount of power by igniting the fuel at the optimal time as engine conditions change and by only using as much fuel as needed to produce the required power. Adding a turbocharger or supercharger increases the pressure in the engine's intake manifold. This allows the engine produce more power than naturally aspirated engine of the same size. While adding a turbocharger or supercharger will not increase the fuel efficiency of the engine, the increased power output means that a smaller engine can be used to achieve a give

required power, and using a smaller engine means less fuel required. Research into modified and alternate engine cycles promises to increase both power and efficiency, but is still a few years away from widespread production. Each of these solutions are focused on automobile engines and do not always scale well to applications requiring small, low cost engines such as the drone and UAV industry.

The UAV and drone industry requires small, lightweight powerplants with high efficiency and high energy density. Electric motors are common on the smallest vehicles. Electric motors have very high efficiency for converting electrical energy into power output. However, batteries are not energy dense and so the vehicles are limited in range and payload since the batteries take up a significant portion of the weight. Another option is to use small piston engines. Hydrocarbon fuels are much more energy dense than batteries. However, reciprocating engines suffer from low overall efficiency and they suffer from decreased performance at altitude due to the decrease in ambient air pressure and density. This decrease in performance can be overcome by increasing the pressure at the engine's intake.

For piston engines, the primary devices for increasing the pressure are superchargers and turbochargers. These devices must be sized accordingly with the engine size, so that a large engine would have a large turbocharger and a small engine would have a small turbocharger. For larger engines, a turbocharger or supercharger is an efficient method to increase the pressure at the engine's intake. However, for small engines, a turbocharger or supercharger may not be the most efficient method for overcoming the pressure loss doe to altitude. This is because the efficiency of small turbochargers is less than that of larger turbocharges due to the small size of the turbocharger components[1]. An alternative for small engines is to use a wave rotor to increase the pressure at the intake. When a wave rotor is used to charge a engine like this, it is called a Pressure Wave Supercharger (PWS). The PWS works by ex-

changing energy between the hot exhaust gases and the fresh intake air without the use of any mechanical devices to extract work from the hot exhaust or to do work on the fresh air.

1.2 Research Objectives

This research aimed to characterize a PWS for an industrial diesel engine as a first step towards using the PWS to supercharge the engine. The research compared different endwalls to determine the effect of the different designs. The performance of each configuration will be determined by finding the compression efficiency of the PWS as it compresses the fresh air fed to the engine. In order to calculate the efficiency, the pressure and temperature are measured at each port. The mass flows through each port are also measured. For this research, the burner built by McClearn [7] was used as the heat source. To accomplish this overall research goal, the following objectives were accomplished.

1. Establish baseline performance using the plain endwall to fill in gaps in previous open loop testing and confirm that the test rig worked as intended

2. Study the impact on performance of the re-entry port endwall configuration and compare to the plain endwall to determine if the re-entry port increases the performance compared to the baseline configuration

3. Understand the performance impact of the pocket endwall configuration to the plain endwall to determine if the pockets increase the performance compared to the baseline configuration

1.3 Methodology

The testing of the wave rotors compared the performance of three different types of endwalls: the plain endwall, the endwall with re-entry ports, and the endwall with pockets. The performance of the wave rotor was measured by calculating the compression efficiency as the air is compressed between the inlet and outlet ports. The efficiency calculation uses the pressure ratio and temperature between the inlet and outlet port. If there is a significant amount of exhaust gas recirculation, it can artificially increase the temperature ratio and reduce the calculated compression efficiency. This is discussed in detail in Section 2.4. Overall, the type of wave rotor cycle researched here was designed for minimal exhaust gas recirculation, so the impact of the exhaust on the outlet temperature was assumed to be negligible. Since the purpose of a wave rotor in the context of this research is to compress air before it is fed to an engine, the compression efficiency and pressure ratio were chosen as the useful parameters to compare the performance of the tested wave rotors. The testing consisted of varying the rotor speed and exhaust temperature for each endwall type. The data was then analyzed and the results are reported in Chapter IV.

The first endwall was a plain style endwall and served as a baseline for comparing the other two configurations. The baseline results are discussed in Section 4.2. The second configuration incorporated pockets in the endwalls, which are discussed in Section 2.3.3. These pockets are designed to improve off design point performance and the results are discussed in Section 4.4. The third endwall configuration was known as a re-entry port endwall. It used additional ports to connect the high pressure air outlet to the low pressure air inlet. These ports are intended to provide some pre-compression of the low pressure air and increase the efficiency of the wave rotor and is discussed in Section 2.3.4. The results of re-entry port configuration are discussed in Section 4.5. Each of these designs were compared by compression efficiency and pressure ratio.

II. Literature Review

2.1 Background and Motivation

There is a need to improve the efficiency of small Unmanned Aerial Vehicle (UAV) engines.[15] Efficiency of small internal combustion engines for aircraft has not been an issue in the past, since engines of this size have been used for lawn mowers and small hobby Remote Controlled (RC) aircraft where efficiency is not a factor. However, to increase the range and endurance, and therefore effectiveness, of small UAV aircraft used by the Air Force, the efficiency of these engines will need improved.

One way to improve the efficiency is with of a supercharger or turbocharger. However, at the small mass flow and small physical size of a turbocharger that is appropriately sized for the small engine, the efficiency is significantly less than larger turbochargers and superchargers. Figure 1 plots the Reynolds number based on the rotor diameter against one minus the efficiency with 1-efficiency on the y-axis and Reynolds number of the x-axis. It can be seen that as the Reynolds number decreases, the efficiency also decreases. The Reynolds number decreases either due to slow flow through the turbocharger or, in the case of small turbochargers, the decrease in Reynolds number is due to the physically small size of the turbocharger components and the small characteristic length used to define the Reynolds number.

Examining the Reynolds number relationship in Figure 1 show that for a given speed, a small Reynolds number means a physically smaller compressor, and leads to decreased efficiency. Similarly, for a given size of compressor, as the rotor speed, and consequentially mass flow, decreases, the Re decreases and therefore the efficiency also decreases. The data in Figure 1 is for centrifugal compressors, which are the same type as what are found in turbochargers.

One way around the efficiency loss due to decreased size is to use compression

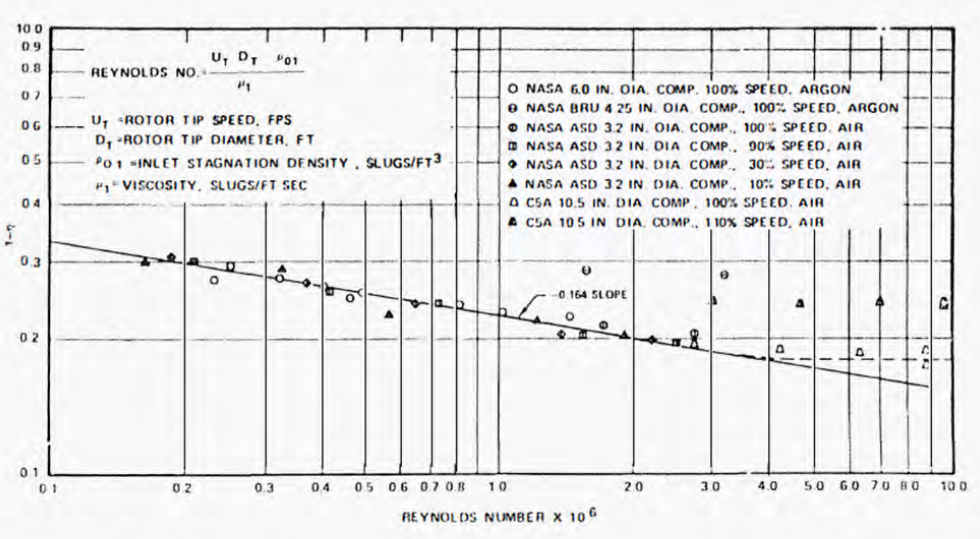

Figure 1. Relationship Between Efficiency and Reynolds Number[1]

waves to compress the flow. As shown in Figure 2, compression efficiency for shock waves is greater than the compression efficiency of both diffusers and mechanical compressors for moderate compression ratios[2].

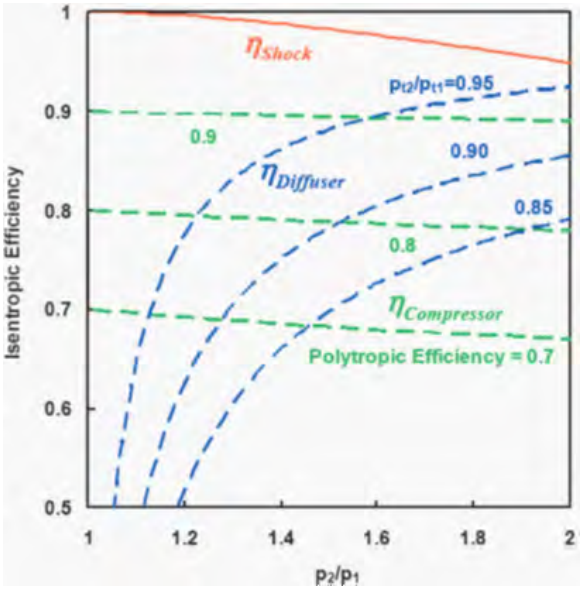

Figure 2. Efficiency of Types of Compression[2]

Wave rotors take advantage of this better efficiency by using shock waves in narrow channels to compress the air and offer an alternative to turbochargers that does not

suffer from the same type of losses as small turbochargers because a wave rotor uses shock waves generated by the sudden opening of the exhaust in port to compress the air that is fed to the engine[6].

For the relatively low pressure ratios of 1.5 -2.5 typical for boosting automobile engines and needed to compensate for the pressure loss at altitude (compared to four to ten per stage for an axial compressor on a jet engine), Figure 2 shows that shock compression is more efficient than using a compressor. Since a wave rotor avoids the efficiency losses due to small size that is typical with turbochargers, wave rotors are a viable, and possibly optimal, choice to boost an internal combustion engine and are the focus of this research. This chapter will introduce the wave rotor cycle in Section 2.2.3 and a brief history of wave rotors as they relate to Pressure Wave Supercharger (PWS) is provided in Section 2.3. This chapter also will discuss methods for determining the efficiency of wave rotors in Section 2.3.1 and Section 2.4 will look at some of the recent research efforts to understand and characterize wave rotors and the unsteady wave process that governs wave rotor performance.

2.2 Wave Rotors as Pressure Wave Superchargers

Wave rotors are devices that use energy from hot exhaust gases from a combustor or internal combustion engine to compress incoming fresh air before the fresh air is fed to the combustor or engine. When a wave rotor is used to charge and internal combustion engine, it is typically referred to as a PWS. Generally, wave rotors fall into one of two categories, through-flow type wave rotors and reverse-flow type wave rotors. PWSs generally fall in to the reverse-flow category and are the focus of this study.

2.2.1 Through Flow and Reverse Flow Cycles.

Through-flow and reverse flow wave rotors are named based on the way fluids flow in the rotor. In a through flow type wave rotor, the fresh air enters the rotor on one side and passes through the rotor to exit out the opposite side, as seen on the left in Figure 3. The exhaust gases will also enter the rotor through a different port on the same side that the fresh air enters and passes through the rotor before exiting out the opposite side. Because the working fluids pass through the wave rotor in a uniform direction, this configuration is called a through-flow wave rotor. Through-flow wave rotors have the advantage of improved self cooling, since the cooler fresh air passes through the rotor during each cycle, cooling the rotor so the rotor material doesn't reach the temperature of the hot exhaust gases that also pass through. However, through-flow wave rotors have a significant amount of unavoidable Exhaust Gas Recirculation (EGR), which can be problematic for internal combustion engines, though combustors in jet engines are less sensitive to EGR.

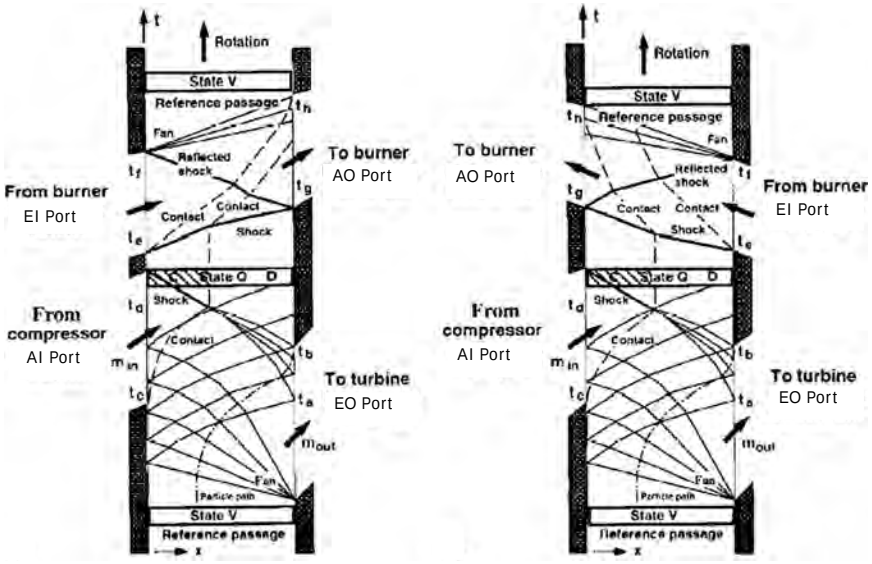

Figure 3. Through-flow and Reverse-flow Wave Rotors[2]

The wave rotor on the right in Figure 3 is a reverse-flow type wave rotor. The flow in a reverse-flow wave rotor reverses direction inside the rotor. The fresh air

enters on what is known as the cold side then reverses direction and exits on the same side it entered, while the exhaust gases enter and exit on the opposite side known as the hot side. Reverse flow wave rotors have the advantage of being able to completely eliminate EGR when properly tuned and to keep EGR low even at off design operation. However, because the hot exhaust gases and cooler fresh air do not pass through the rotor, a reverse flow wave rotor can have uneven heating and cooling loads, causing uneven thermal growth and possibly causing structural problems.

The different cooling and EGR properties of through-flow and reverse-flow wave rotors make them useful for different applications. Through-flow wave rotors are typically used as topping cycles for jet engines where cooling is very important and the combustor is less sensitive to EGR, while reverse flow wave rotors are normally used to boost internal combustion engines that are more sensitive to EGR but the exhaust gas temperatures are less extreme so that cooling is less important, though it is possible to use either type of wave rotor for either application[2].

Both wave rotors in Figure 3 are shown as applied to a gas turbine topping application where the fresh air in comes from a compressor and the exhaust out goes to a turbine. The port nomenclature in Figures 3 and 5 is used throughout this paper where the Air In (AI) port is where the fresh cool air enters the rotor, the Air Out (AO) port is where the compressed fresh air exits the rotor, the Exhaust In (EI) port is where the hot high pressure exhaust enters the rotor, and the Exhaust Out (EO) port is where the hot exhaust gases exit the rotor. These port labels are used in this paper independent of where the air or gases go after exiting the rotor.

2.2.2 PWS versus Turbocharger Performance.

A pressure wave supercharger has advantages over conventional turbochargers other than avoiding the scaling losses. For example, the PWS almost completely

eliminates tubo-lag since it uses pressure waves to transfer the energy from the exhaust to the fresh air instead of mechanical components, which is a significant advantage over turbochargers when comparing the drivability of a boosted engine[3][8]. Figure 4 shows on the right hand set of plots the manifold pressure and engine speed versus time for the Comprex® and a turbocharger. The manifold pressure in the Comprex® increases to near the maximum value almost two seconds faster than the turbocharger, reflecting the reduced turbo lag of the Comprex®. This faster increase in manifold pressure corresponds to torque being applied to the wheels sooner and less of a feeling of turbo lag. The PWS also increases Brake Mean Effective Pressure (BMEP), which can be seen in the chart on the middle left in Figure 4. This chart also shows how an intercooler increases the BMEP with the Comprex®, and presumably the intercooler would have the same effect with a regular turbocharger. Intercoolers are discussed further in Section 2.6.2. The notable part of the chart in Figure 4 is how the Comprex® increases the BMEP above that of a turbocharge for low engine speeds. The increased BMEP indicated the PWS's better performance than a turbocharger in this range.

2.2.3 The PWS Cycle.

When a wave rotor is used as a PWS, it is incorporated into the engine by routing the AO port to the engine's intake and routing the engine's exhaust gas to the EI port. Figure 5 shows how the PWS is integrated with a simple single piston engine. The ambient air enters at the AI port at the bottom of the figure and then is compressed by the hot exhaust gas as the rotor spins. The compressed air is then forced out the AO port and the exhaust expands out the EO port[16].

Figure 6 shows the basic wave structure that moves the flow in a reverse-flow type wave rotor. The PWS cycle is described in detail in Gyarmathy's 1983 paper[16].

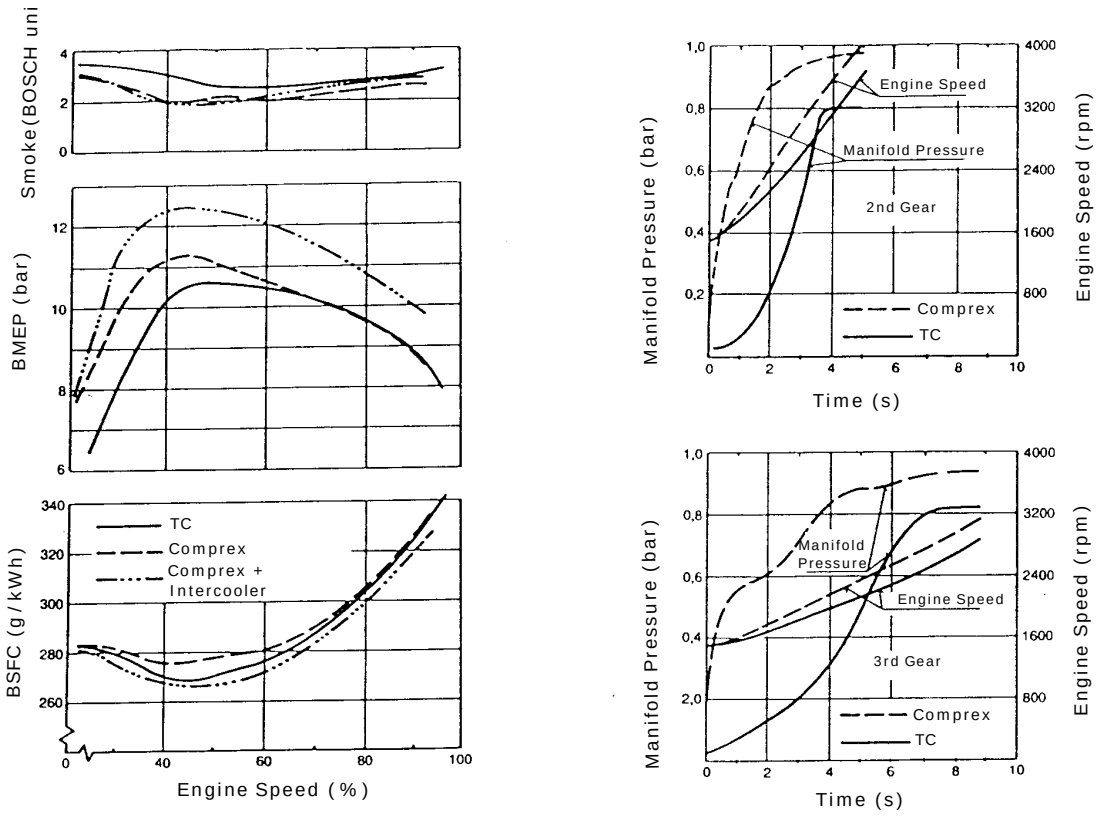

Figure 4. The performance of the Comprex vs. a Turbocharger [3]

The cycle starts at the bottom of the figure with exhaust gases at high pressure and temperature in the channel. The side from which the hot exhaust gases enter and exit is called the hot side, and the side where the colder fresh air enters and exits is called the cold side. At Point One, the EO port opens to the lower pressure in the exhaust ducting and an expansion wave is generated that travels to the opposite side of the channel and starts the flow of exhaust gases out the EO port. At Point Two, the expansion wave hits the opposite wall and is reflected back to the original side. Right at this reflection, the AI port opens and draws in fresh air, driven by the expansion waves and the flow of fluid out the EO port. During the relatively long time that the AI and EO ports are open the expansion wave travels back to the open EO port and is reflected off the open port as a wave of the opposite type, which is compression in this case. The compression wave travels back to the open AI port and

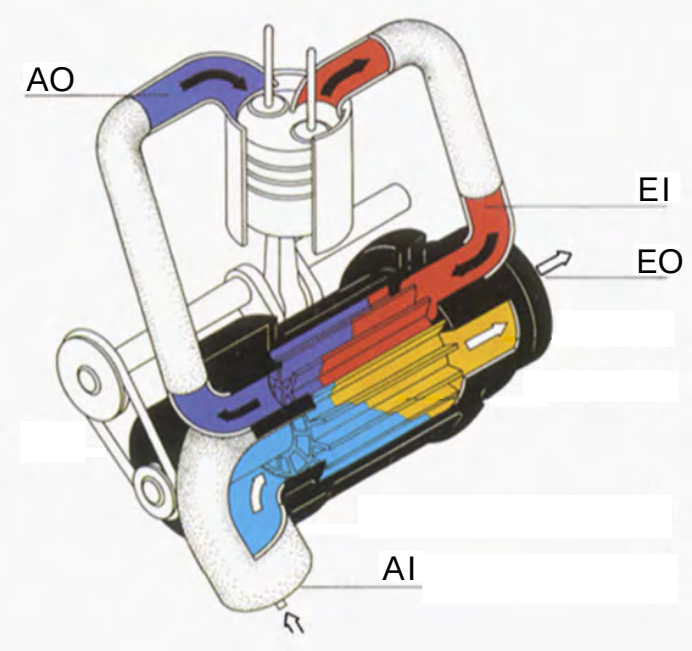

Figure 5. Flow in a Reverse-Flow PWS and Pistion Engine[4]

is again reflected as a wave of the opposite type.

These waves and reflections travel back and forth several times before the EO port closes at Point Three. Also, during the time that the AI and EO ports are open, exhaust gases and fresh air are flowing from the AI port to the EO port. During on design point operation, the AI and EO ports are open long enough that the channel is completely exhausted of exhaust gases and fresh air is scavenged through the entire

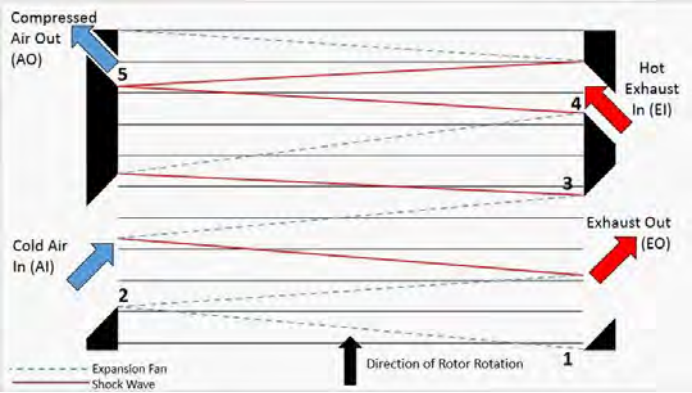

Figure 6. Wave Structure and Port Labeling in a Reverse-Flow PWS[5]

length of the channel, cooling the wave rotor. When the EO port closes in Figure 6, a hammer shock is generated, stopping the flow out the EO port. The shock travels the length of the channel and reaches the opposite side just as the AI port closes. Both ends of the wave rotor are now closed, and the channel is filled with fresh air at ambient pressure and temperature. There are still some residual compression and expansion waves traveling back and forth in the channel, but these are neglected in the analysis because the net effect of the waves is nearly zero.[16].

The next part of the cycle in Figure 6 process happens at Point four, when the EI port from the engine opens to the hot, high pressure exhaust gases in the exhaust manifold. The sudden opening of the EI port, and therefore sudden exposure of the low pressure air in the channel to the high pressure exhaust, causes a compression shock wave to be initiated and travel the length of the channel. This shock wave compresses the fresh air in the channel and starts it moving towards the AO port. This shock wave is how energy is transferred from the exhaust to the fresh air. When the shock reaches the opposite side, it reflects and compresses the flow further. Just as the shock wave is reflected, the AO port opens, allowing compressed fresh air to flow through the intake manifold to the engine. When the reflected shock reaches the original side of rotor, the EI port closes, generating an expansion wave that stops the flow. The AO port closes just at the expansion wave from the closing EI port reaches that side of the rotor, and conditions in the channel now match those at the bottom of Figure 6, which is the beginning of the cycle, and the cycle repeats in this manner[16].

2.2.4 Note on Wave Speed as it Relates to Exhaust Temperature.

Some wave rotor research, including recent research at AFIT and AFRL, relates the speed the rotor must turn to the temperature of the hot gases entering through

the EI port[17, 6]. The speed of the rotor must be matched to the wave speed inside the rotor and the length of the rotor so that the primary compression wave from the EI port reaches the opposite endwall just as the AO port opens. This compression wave is shown circled in Figure 7. However, the temperature of the gases entering through the EI port do not directly influence this wave speed. As shown in Equation 1, the wave speed depends the pressure ratio of the fluids directly upstream and downstream of the compression wave and the speed of sound in the fluid it is traveling through[18]. As indicated by the solid red and blue dashed lines in Figure 7, the primary compression wave travels through the rotor ahead of the boundry between the exhaust and fresh air. Therefore, the wave speed is dependent on the temperature of the fresh air only, as shown in Equation 2. CFD work done by Haidinger et al. confirms the dependency of the wave speed on the pressure in the high pressure exhaust inlet port[8].

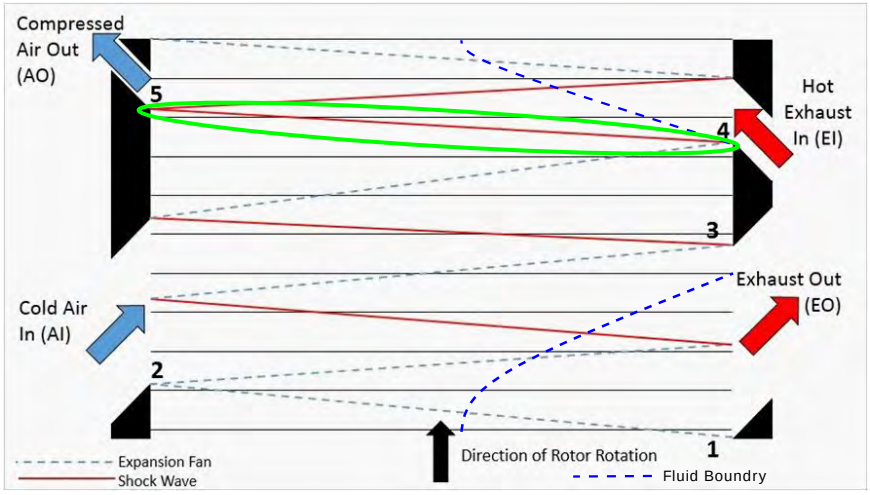

Figure 7. Wave Diagram with the Fluid Boundary and the Primary Timing Wave Circled, Adapted from [5]

$$W = a_1 \sqrt{\frac{\gamma + 1}{2\gamma} \left(\frac{p_2}{p_1} - 1 \right) + 1} \tag{1}$$

$$a = \sqrt{\gamma R T} \tag{2}$$

$$\frac{p_4}{p_1} = \frac{p_2}{p_1}\left\{1 - \frac{(\gamma_4 - 1)\left(\frac{a_1}{a_4}\right)\left(\frac{p_2}{p_1} - 1\right)}{\sqrt{2\gamma_1\left[2\gamma_1 + (\gamma_1 + 1)\left(\frac{p_2}{p_1} - 1\right)\right]}}\right\}^{\frac{-2\gamma_4}{(\gamma_4 - 1)}} \tag{3}$$

$$P = \rho RT \tag{4}$$

Equation 1 also shows that the wave speed depends on the pressure directly before and after of the wave, indicated by the ratio $\frac{p_2}{p_1}$. In a wave rotor, this is the pressure of the compressed fresh air to pressure of the uncompressed fresh air. By looking at Equation 3, it is seen that the pressure ratio of the fluids directly before and after the compression wave depend on the pressure ratio of the initial pressure in the high pressure fluid to the initial pressure in the low pressure fluid, which is $\frac{p_4}{p_1}$[18]. In a wave rotor, this is the pressure of the hot exhaust gases in the EI port over the pressure of the uncompressed fresh air. Thus, by adjusting the pressure of the exhaust gas that the wave speed in the rotor is changed and the proper speed of the rotor determined. However, the pressure at the EI port may not always be readily adjusted, depending on the test setup used. Also, since most wave rotor applications use hot exhaust from an engine or combustor to feed the EI port, having a high temperature gas at EI is more realistic. Since the volume of the ports on a wave rotor are fixed, the temperature and pressure of the fluid in the ports are proportional, as shown in Equation 4. This means that the pressure in the EI port is a function of the temperature at the EI port, and the EI temperature becomes the most convenient parameter to adjust when testing a wave rotor. Therefore, for this research, the EI temperature is adjusted in order to change the pressure in the EI port instead of directly adjusting the pressure.

2.3 History of the PWS

As early as 1928, the use of shock waves to exchange pressure between two fluids was proposed by Burghard, but the lack of understanding of unsteady wave mechanics prevented practical application of the technology. Understanding of unsteady wave motion in the 1940s allowed for the development of practical wave rotor devices. The Brown Boveri Company (BBC) got its start in wave rotors in the 1940s developing a through-flow type wave rotor for use on railway steam turbine engines. Though this wave rotor performed well on paper and in the lab, difficulties with the actual integration prevented the wave rotor from meeting expectations when installed in the field. The BBC also began developing a PWS for use in diesel engines in the 1950s, and this development culminated in the Comprex® PWS used on the Mazda 626 passenger diesel engine in the 1980s[2]. Several other vehicles were supercharged using the Comprex® PWS, though use of the Comprex® for passenger cars eventually faded due to improvements in spark ignited engines and the complexity of the Comprex® cycle. Interest in PWSs has grown due to performance of internal combustion engines plateauing and the increasing pressure for greater performance with better efficiency and fewer emissions.

2.3.1 Previous Work at AFIT and AFRL.

In 2012, Smith began work at AFIT and AFRL for a scaled down version of the Comprex® PWS. Smith's goal was to scale down the Comprex® to apply to a 100cc two-stroke engine[9]. A scaled down PWS was successfully designed and validated against CFD models, but the wave rotor cycle was never integrated with the two-stroke engine cycle. In 2014, Mataczynski continued research into boosting a small two stroke engine with a PWS[5]. Mataczynski also successfully designed a wave rotor cycle and validated the CFD model by comparing it with the Comprex®

performance data. However, the scaled down PWS designed by Mataczynski suffered from rotordynamic problems and was never fully integrated into the cycle.

The first iteration of pressure wave supercharger was a scaled down version of the Comprex pressure wave supercharger cycle for use in a 95cc engine [5]. This wave rotor design began with testing of a Comprex and comparing the test results to the quasi-one-dimensional simulation developed by Dr. Paxson at NASA Glen Research Center. The testing was conducted using the same test bench as described by Smith et al. [19], and the tests were conducted using an open-loop configuration. An open-loop configuration means that the AO port does not connect to the EI port as it would when integrated with a real engine. In contrast, a closed-loop configuration means that the AO port is connected and provided pressure to the EI port. The simulation matched the test results for the Comprex, therefore the simulation was assumed to be accurate for designing the scaled down wave rotor. Similar to the Comprex design, a cantilever rotor design was chosen where the rotor is mounted on a shaft that is supported on bearings in the cold endwall. Putting the bearings in the cold endwall reduced the amount of heat to which the bearings were exposed.

The scaled down wave rotor was then tested using the same test bench as the previous Comprex testing[20]. The rotor was only able to achieve 63% of the design rpm of 34,500 rpm due to limitations of the battery and speed controller used to power the electric motor. The pressure wave supercharger was able to achieve an efficiency of 54% with an EI temperature of 380 K and a rotor speed of 19,000 rpm, both of which are well below the design point of the scaled pressure wave supercharger which was 34,5000 rpm and 815 K. This efficiency was found with the gate valve on AO at 3% open, which is the most closed position [3]. Closing the AO valve provides back pressure that simulates the effect of a real engine, however, closing the AO valve also reduces the mass flow through AO so that the mass flows in AO and EI are not

balanced as they would be when the wave rotor is coupled to a real engine. The CFD simulation was also run at this test point, and the simulation results showed good agreement with the test results except for the mass flow at AI and the pressure ratio at AO. The simulation under predicted the AI mass flow by 33% and over predicted the AO pressure ratio by 19%; all the other compared values were within 7.1% between the simulation and the test results. This gave confidence to the simulation results for the wave rotor when operating much closer to the design point.

In parallel with the later work by Mataczynski, McClearn and Lapp designed through-flow type wave rotors to investigate scaling effects in wave rotors and to investigate the performance of a wave rotor used to produce shaft power[15][7]. Both Lapp and McClearn applied the lessons learned by Mataczynski and successfully designed rotors that avoided rotordynamic issues, however, they both had difficulty getting the cycle started and up to design operating speed and temperature. McClearn also designed and fabricated the test rig used by him and Lapp to test the rotors. Lapp's test results showed that the wave structure did not set up correctly, causing exhaust to come out the inlet. Future work could include a method to prevent the backflow through the inlet in order to set up the proper wave structure in the rotor.

After the tests presented in [20], the electric motor and speed controller were changed to be able to achieve the design point rotor speed. However, increasing the rotor speed revealed that this design suffered from vibrational modes that significantly decreased the life of the bearings [17]. In order to understand the rotational modes, Mataczynski et al. conducted a rotordynamics analysis. The analysis also revealed how to improve the shaft design so that the first mode was shifted to a rotational speed above the design point of the rotor. Also, at this point some other minor design changes were made to better align the electric motor with the shaft and to reduce leakage past the shaft into the endwall. The improved rotor design was tested using a

modified combustor from a T-63 helicopter engine to reach EI temperatures that had previously been unreachable. The higher EI temperature and increased maximum rotor speed of 636 K and 35,500 rpm allowed for testing much closer to the design point of the pressure wave supercharger. This testing showed improvement in the maximum efficiency over previous testing, with the maximum efficiency found to be 76% [17]. This is largely due to being able to operate the wave rotor nearer the design point.

In 2017, Mataczynski et al. published a design for a pressure wave supercharger sized for a 719cc diesel engine instead of the 95cc two-stroke engine [6]. The wave rotor for the diesel was designed using all the lessons learned in the previous testing, so that rotordynamic problems were avoided. The air side endwall where the bearings are mounted was also redesigned to eliminate leakage through the bearings. The same quasi-one-dimensional code that had been used previously was used to simulate the new wave rotor at a variety of operating conditions. This new wave rotor was tested using similar equipment and methods as the previous research, using an open-loop configuration, an electric heater to supply heated air to EI, and a gate valve to provide back pressure to AO. The simulation results were published in [6] while bench testing was still ongoing, therefore some of the bench testing results are presented in [21] along with the preliminary results of the diesel engine integration.

Reinhart continued Mataczynski's work with the pressure wave supercharger and integrated the wave rotor onto a 898cc diesel engine very similar to the engine designed for by Mataczynski, though slightly larger. Three different integration configurations were used, one open-loop and two closed-loop. Since the AO port was not connected to the EI port in the open-loop configuration, a gate valve was used to provide back pressure at the AO port. Figure 8 shows the test setup used to test the pressure wave supercharger that was designed for the diesel engine. The open loop setup was

used to be able to independently control the mass flows in the exhaust gas side and the fresh air side of the wave rotor, since the mass for on the exhaust gas side was controlled by the engine rpm and the mass flow on the fresh air side was primarily regulated by the AO gate valve.

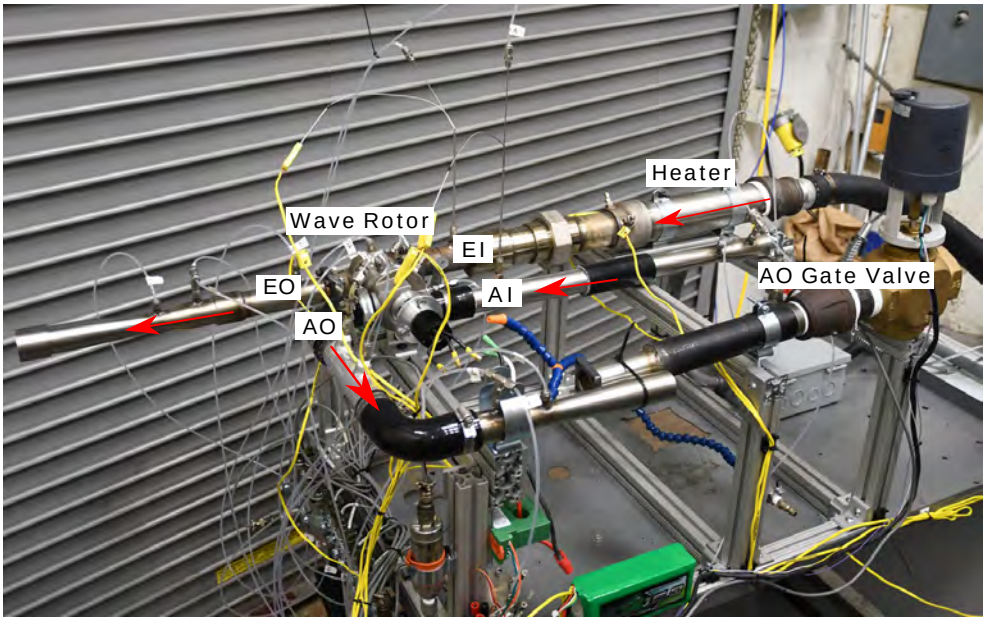

Figure 8. The Mataczynski PWS in the Test Rig[6]

An electric heater heated the air from the test facilities compressed air system. The heated compressed air was then fed to the EI port to simulate the hot exhaust gas from the engine. The air fed to the EI port ranged from 550 K to 880 K and 134,450 to 161,340 Pa. The gate valve on the AO port simulated the back pressure of about 124,100 to 206,800 Pa that would be seen at the AO if it were connected to an engine. This setup had venturis at the AI, AO, and EO ports to measure the mass flow, and the mass flow into the EI was measured with a sonic nozzle.

2.3.1.1 Burner History.

The primary heat source used in this research was the can-type combustor designed by McClearn, referred to as the burner in this document. The burner was designed to

support the research of a through-flow type wave rotor that was designed to output 3 kilowatts of power[7]. The burner design is shown in Figure 9. The overall flow of air and fuel in the burner is from left to right in Figure 9. The ethylene fuel is injected at the entrance to the swirler on the left of the figure while the hydrogen is injected through the torch the enters the combustor at the top of the image. The burner used the hydrogen torch to ignite the ethylene and then the hydrogen was shut off once a stable flame was achieved. The exit of the burner leads to a reducer that reduces the pipe diameter for connecting to the wave rotor. Further details about the design process of the burner can be found in McClearn's thesis[7].

2.3.2 Other Wave Rotor Research.

Wave rotor research was started by NASA at the Glen Research Center in 1988. The primary focus of the NASA research was for improving aircraft turbine engines. This research led to the development of a method to solve for the internal unsteady wave dynamics in 1992 by Dr. Paxson[22]. The code used a second order explicit Lax-Wendroff scheme based on the method of Roe to find a quasi-one-dimensional solution for the flow inside the rotor. The code uses the boundary conditions at the ports to generate pressure and temperature profiles inside the rotor that are non-dimensionalized by the conditions at the AI port. The current version of the

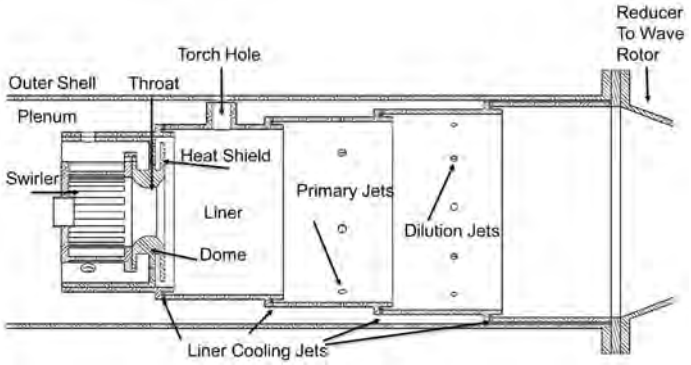

Figure 9. The Can Type Combustor designed by McClearn[7]

code accounts for leakages in the rotor, and has been verified against experimental data for use designing wave rotors for turbine topping cycles[23]. The code was modified to simulate the flow in reverse-flow wave rotors. This modified code was used by both Smith and Mataczynski to compare the simulation to experimental Comprex® data[19, 5]. Both of these research efforts showed good agreement between the simulation and the experimental data. The code was used again by Mataczynski to design a PWS for a small engine based on the Comprex® design. This design also showed good agreement between the experimental data and the simulation when the inputs to the simulation were set to match the test conditions[20, 17].

In 2009, Lei, Zhou, and Zhang took a turbocharged diesel engine and replaced the turbocharger with a Comprex PWS and compared the performance of the PWS boosted diesel to the turbocharger boosted diesel, as well as to CFD results[4]. Figure 10 shows the results achieved by Lei et al. Each chart shows a different measure of diesel engine performance plotted against engine speed. The PWS charged engine produced more power and torque than the turbocharged engine, and also reduced soot emissions and significantly reduced NO_x emissions. The reduced emissions is a function of the built in EGR that can occur in a PWS.

One notable result was that when the original Comprex was mounted onto the stock intake manifold of the engine, it did not perform as well as the turbocharger. Lei et al. then performed a sensitivity analysis comparing excessive air ratio, PWS speed, exhaust pressure, exhaust temperature, intake temperature, intake pressure, air flow, and engine speed to determine what design changes would improve the performance. The result was that the temperature at EI and the air flow were the most influential parameters. The test rig was then modified by increasing the size of the intake manifold to allow for an increased mass flow from $350\frac{kg}{hr}$ to $400\frac{kg}{hr}$ and insulating the exhaust manifold to keep the temperature at EI as high as possible,

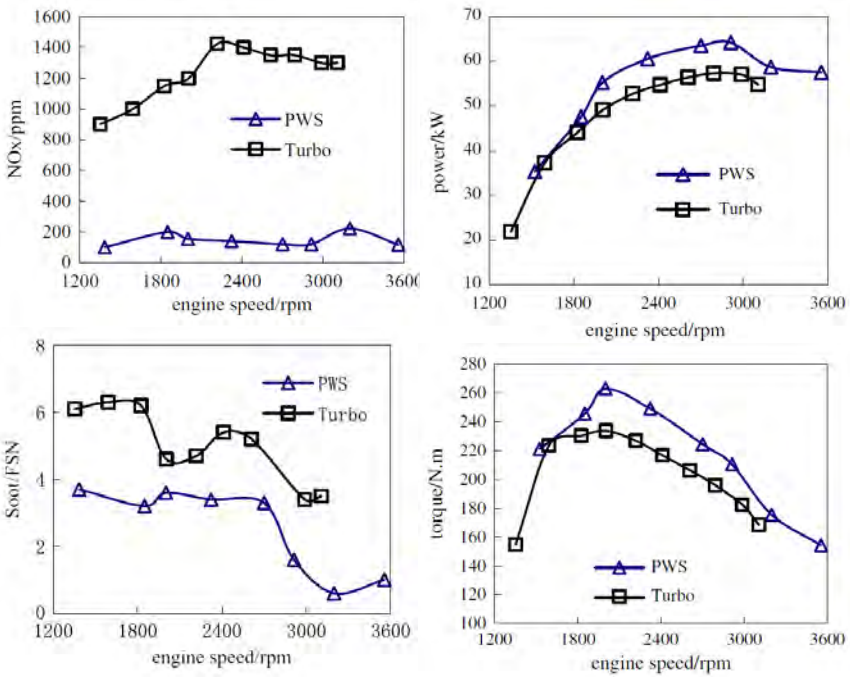

Figure 10. Performance Comparison of the Modified PWS to the Turbocharger[4]

between 800K and 1000K. The modification increased the performance of the PWS above that of the stock turbocharger, increasing the peak power by 12% and the peak torque by 13%, as seen in Figure 10.

Work has also been performed in 2016 by Kurec and Piechna at the Warsaw University of Technology to obtain detailed pressure measurements inside a rotor channel, and to match those measurements to CFD analysis[24]. The channel geometry differed greatly from the rotor used by Mataczynski[6] in the size of the rotor. The stationary channel used by Kurec and Piechna was 0.5 meters long, and the endwall rotated at 1500 rpm at design point. The rotor used by Mataczynski was only 0.056 meters and spun at 26,500 rpm. Despite the differences, both rotors operate correctly at their respective operating conditions, demonstrating that the wave dynamics depends only on the relationship between wave speed, the radial location of the ports on the endwalls, and the angular speed. However, in both the Mataczynski configuration and Kurec and Piechne configuration only achieved a pressure boost at the AO port

when a valve restricting the mass flow through the AO port, and both configurations only achieved a meaningful pressure rise at the AO port when this AO valve was closed or nearly closed, which meant that there was very little or no mass flow out the AO port. Since the purpose of a wave rotor is to provide pressurized air out the AO port, a wave rotor that only provided pressure when there is very little mass flow out AO doesn't have a practical application.

This trade off between pressure and mass flow at the AO port is a condition of open loop testing. Since the AO port does not connect to the EI port through a heat source, there is no built in mechanism to provide the needed back pressure at the AO port to properly set up the internal wave structure in the rotor. Therefore the gate valve on the AO port is necessary to provide the needed back pressure. In a closed loop setup where the AO port is connected to the EI port through a heat source such as an engine, a valve to provide back pressure is not needed since the EI port of the wave rotor is providing the back pressure so that the AO port has both the needed mass flow and pressure rise for practical wave rotor operation.

In 2017, Haidinger, Kriegler, and Millward-Sadler performed a CFD analysis to compare engine parameters and how they influenced the PWS performance[8]. The CFD was targeted at determining what influence the timing of the port opening and closing. This was done by finding the amount of time the shock wave took to travel the length of the rotor as the temperature at the inlet and pressure at the high pressure ports were varied. The CFD analysis revealed that varying the temperature at the EI port did not significantly influence the timing of the opening of the AO port, though it did influence the mass flow through the rotor. When the pressure in the EI port was varied, the opening time of AO port did change as seen in Figure 11. The AO port opened sooner when the pressure in the EI port was increased. This makes sense because the wave speed is dependent on the pressure difference between the working

fluids. Determining the opening time of the AO port is important because the AO port needs to open just as the wave reaches that side of the rotor so that the wave pushes air into the port.

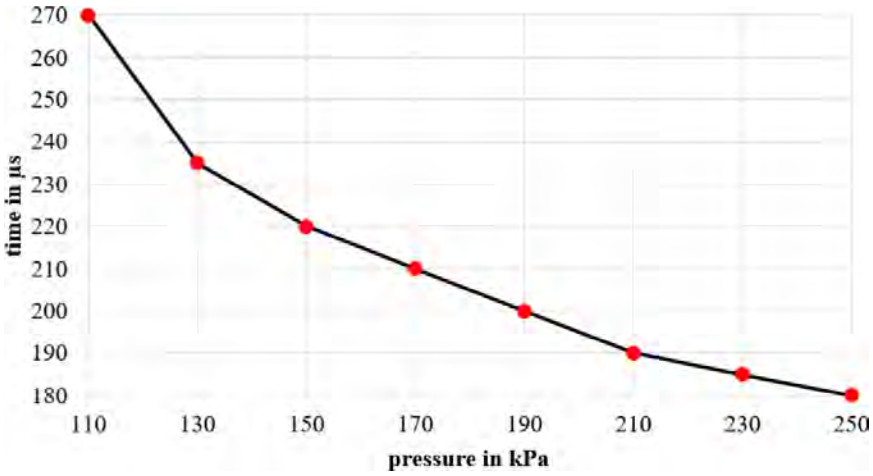

Figure 11. AO Opening Time as a Function of EI Pressure[8]

The study then applied CFD to design a practical PWS for a 600cc engine. Haidinger et al.'s goal for the PWS was to make it practical for use in recreational vehicles. Since the design planned to use an electric motor to rotate the rotor, it was necessary to keep the inertia of the rotating parts as small as possible. This was accomplished by using stationary channels instead of a rotor and rotating timing discs in the endwalls. Because both the ports and channels were stationary, two timing discs on each end were required to ensure that the channels were exposed to the proper pressure at the proper time. The new PWS configuration had not yet been tested, but the use of CFD tools to model the proposed configuration and by tuning to ensure that the channel length, timing disc speed, and EGT are matched should minimize any problems with performance. This design should produce sufficient boost for the recreational vehicle market.

2.3.3 Effect of Endwall Pockets.

The original design of the Comprex® included pockets dug out of the endwalls, as shown in Figure 12. These pockets reduced the reflections of shock waves when the reflection would degrade the performance of the PWS[16]. In effect, the pockets improve the performance when the PWS is operating off design point, especially for wave rotors that are intended to operate efficiently over a wide range of speeds and EI temperatures. For a PWS that is ideally tuned, the pockets were believed to have no effect since all of the waves are precisely in their ideal locations. However, even with rotor speed controlled independent of engine speed, the wave structure is never quite perfect. Therefore, pockets are useful for absorbing extra pressure waves even when the PWS is operating on design point and should be included in PWS designs[25].

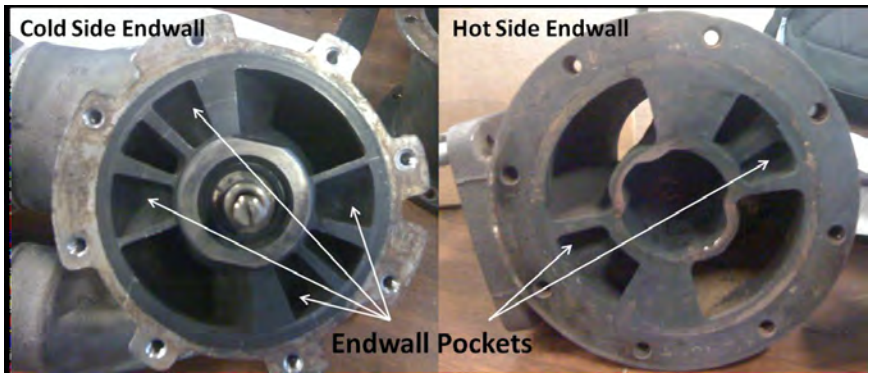

Figure 12. Endwall Pockets in the Comprex® PWS[9]

2.3.4 Effect of Endwall Re-Entry Ports.

The re-entry port endwalls were designed by Aerodyn Combustion for Innovative Scientific Solutions. Shown in Figure 13, this design used an additional port just after the AO port to feed compressed fresh air to a second additional port just before the AI port. The purpose of this port was to provide some pre-compression of the fresh air in the port. The intended effect is to increase the pressure provided to the engine through AO and to reduce the possibility of EGR[10].

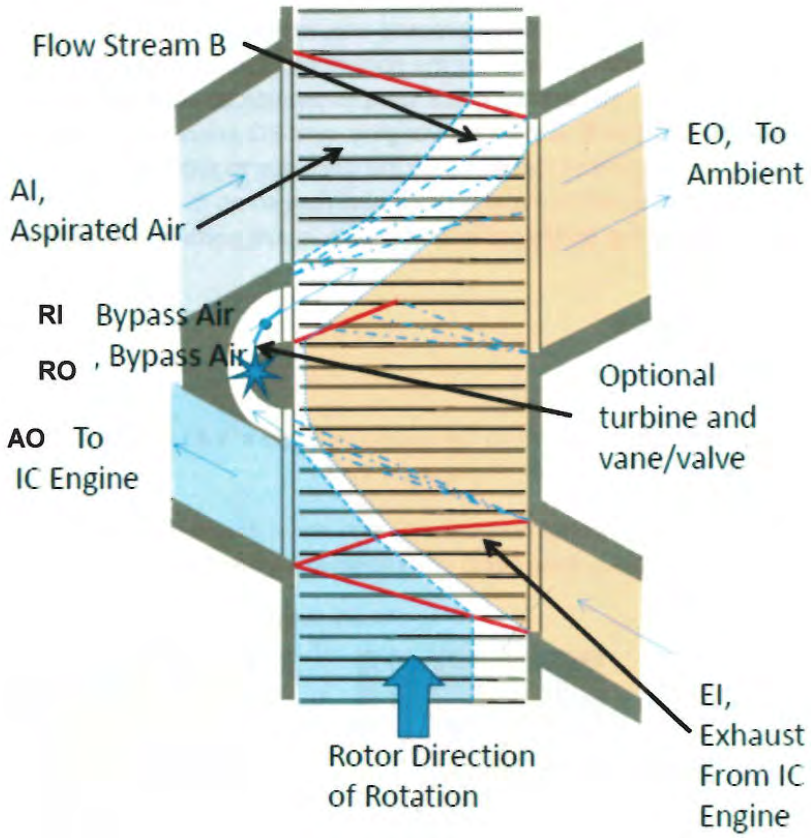

Figure 13. The Wave Structure Cycle in a Re-Entry Port Wave Rotor[10]

Aerodyn Combustion performed CFD analysis of the re-entry port configuration using code based on the wave rotor modeling code from Dr. Paxson of NASA. The wave structure diagrams from the simulation are shown in Figure 14. The CFD analysis showed improvements in the AO/AI pressure ratio (6.4%) and in the mass flow through the low pressure ports (20.6%). The significantly increased mass flow through the AI and EO low pressure ports means that the re-entry port design is much less likely to experience EGR[10], which was a design goal for the re-entry wave rotor. As the AI port pulls in more air relative to the baseline design while the AO port removes the same amount to send to the engine relative to the baseline design, the additional fresh air must exit out the EO port. The extra scavenging of the wave rotor helps to cool the rotor and prevent EGR[16].

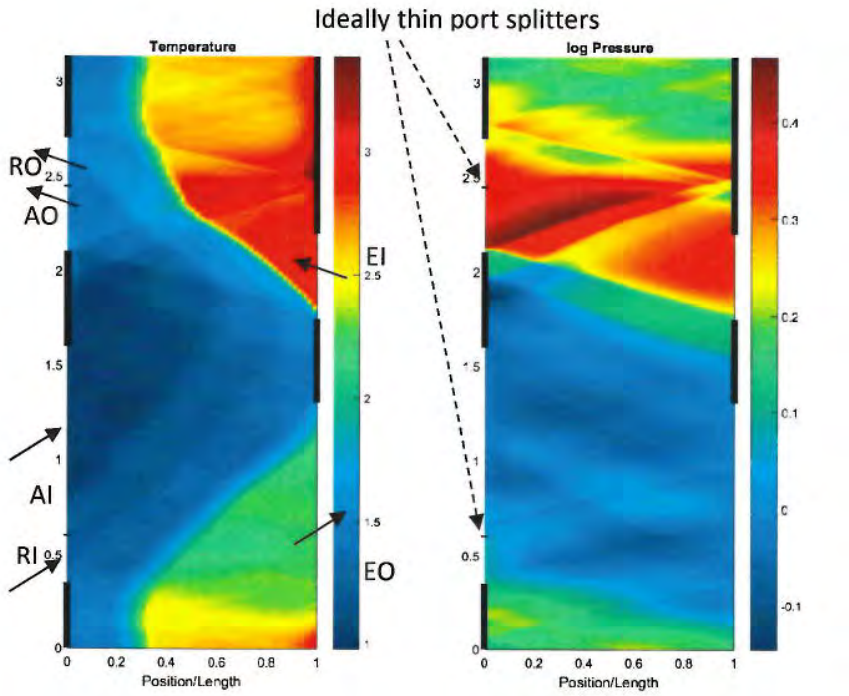

Figure 14. The CFD Results for the Re-Entry Endwall[10]

2.4 Wave Rotor Efficiency

2.4.1 Reverse-flow Efficiency.

In traditional turbomachinery, the efficiency is a straight-forward calculation based on the ideal work needed over the actual work performed for a given pressure rise. This straight-forward calculation is allowed because the fluid in the compressor or turbine is a uniform thermodynamic state. For a reverse-flow type wave rotor, the efficiency calculation is also typically straight-forward. Because there is typically little to no EGR in reverse flow wave rotors, especially when operating at design point, the efficiency is calculated the same way it is for a traditional compressor. The formula is given in Equation 5.

$$\eta_c = \frac{\left(\frac{P_{AO}}{P_{AI}}\right)^{(\gamma-1)/\gamma} - 1}{\frac{T_{AO}}{T_{AI}} - 1} \tag{5}$$

In Equation 5, η_c is the compressor efficiency of the reverse-flow wave rotor, and P_{AO} and T_{AO} are the stagnation pressure and temperature in the AO port, which is the port that feeds compressed air to the engine. P_{AI} and T_{AI} are the stagnation pressure and temperature at the AI port, which pulls in fresh air from ambient conditions. Reference to Figure 3 for the port labels.

Using the typical compressor efficiency definitions is valid for reverse flow wave rotor because the fluid being measured in the AI and AO ports consists only of the fresh air part of the cycle, similar to a traditional mechanical compressor. If significant amounts of EGR were to occur in the reverse flow wave rotor, such as in significantly off-design point operation, the accuracy of Equation 5 will drop due to the fact that the fluid properties being measured in the AO port are the properties of a mixture of exhaust gases and fresh air, and a method of calculating efficiency similar to a through-flow type wave rotor will need to be considered, which is discussed in the next section.

2.4.2 Through-flow Efficiency.

In a through-flow wave rotor, the fluid that enters the combustor, which would be equivalent to the fluid exiting the compressor in a turbine engine, is a mixture of fresh air and compressed exhaust gases. These two streams both exit the compression part of the wave rotor and must be accounted for. The method suggested by Chan, Liu, and Xing accounts for the different streams by defining control volumes in the rotor as shown in Figure 15 and tracking each stream as it enters and exits the control volume[11]. This method is similar to the methods used to determine the expansion efficiency of cooled turbines since those also must account for multiple streams at different thermodynamic properties.

The compression control volume in Figure 15 is drawn such that the control volume

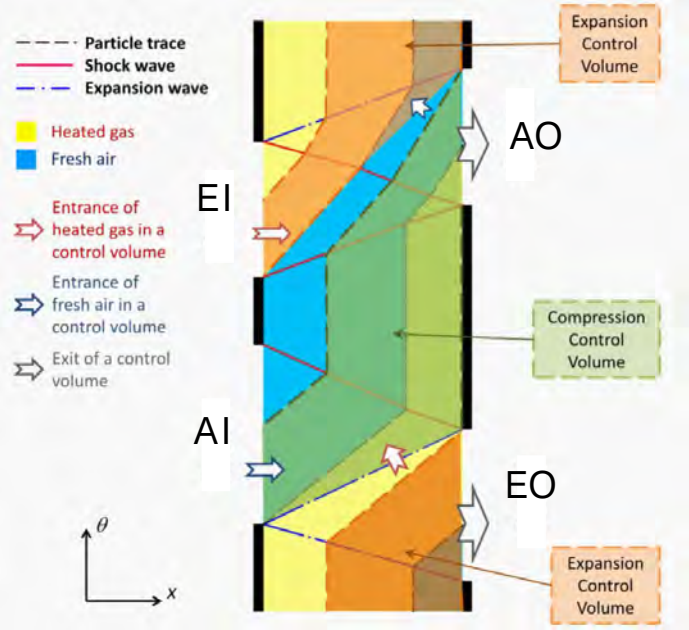

Figure 15. Control Volumes for Defining Compression and Expansion Efficiency[11]

exit covers the entire AO port. The control volume then traces the particle path for the fresh air that exits the AO port from the port back to the AI port where it came in, so that only the portion of fresh air that exits through the AO port is included in the control volume. The control volume also included the exhaust gases that exit through the AO port by extending the control volume from the opening of the AI port to the closing of the EO port such that all the exhaust gas that exits through the AO port enters the control volume through this line. The expansion control volume is drawn using the same process starting from the EO port.

In order to account for the different thermodynamic properties of the exhaust gas and fresh air streams that exit each port, the method of Chan et al. tracks the mass fraction of each fluid as it enters and exits each control volume and determines a weighted average temperature based on the mass fraction of each fluid[11]. In their method, the ratio of the mass of exhaust gas that enters the rotor to the ratio of fresh air that enters the rotor is defined as λ, and the mass of fresh air entering the rotor is set equal to one. This leads to the mass of exhaust gas that enters the rotor being

equal to λ. In addition to EGR, the term Fresh Air Exhaustion (FAE) is used to refer to fresh air that exits through the EO port with the exhaust gas. The efficiency can then be calculated using Equation 6[11].

$$\eta_c = \frac{c_{p,a}\left(1-\psi_{FAE}\right)\left(T_{AO,a,ideal}-T_{AI}\right)+\lambda\psi_{EGR}c_{p,g}\left(T_{AO,g,ideal}-T_{EO}\right)}{c_{p,a}\left(1-\psi_{FAE}\right)\left(T_{AO,a}-T_{AI}\right)+\lambda\psi_{EGR}c_{p,g}\left(T_{AO,g}-T_{EO}\right)} \tag{6}$$

The temperatures for the exhaust gas and fresh air at the AO port in Equation 6 could be found experimentally by finding the circumferential temperature distribution around the AO port. Alternatively, the temperatures could be found using CFD modeling. Using CFD to model the temperatures may be the most practical method to determine the circumferential temperature distribution due to the complex geometry and small size of the endwalls of the PWS.

2.5 Small Diesel Engines

The diesel engine used for this research is an indirect injection diesel engine. Figure 16 pictorially shows the difference between Indirect Injection (IDI) and Direct Injection (DI) engines. The IDI type of diesel has a pre-chamber where fuel is injected before the fuel and air mixture enters the primary combustion chamber in the cylinder with the piston. A glow-plug is fitted into the pre-chamber, and the ignition process starts here. As the pressure increases in the pre-chamber due to the beginning of combustion, the fuel and air mixture is forced into the primary combustion chamber where most of the fuel is burned. The remainder of the cycle is the same as it is for any four stroke internal combustion engine. By comparison, a DI diesel engine is more similar to a typical gasoline engine where the fuel is injected directly into the cylinder and there is no pre-chamber. For modern automobiles, DI diesel engines have replaced IDI engines due to the DI engine's greater power output, greater efficiency,

and reduced emissions. However, IDI engines still have some advantages, such as increased reliability and easier maintenance[26][12].

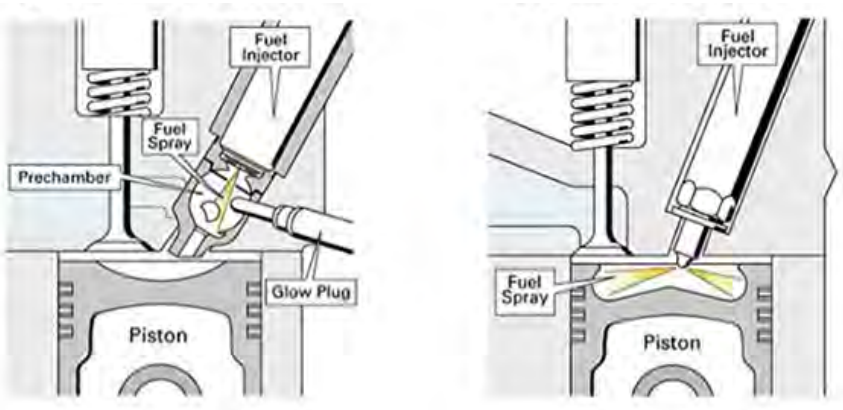

Figure 16. IDI Diesel Engine vs DI Diesel Engine[12]

2.5.1 Blow-By.

High pressure air and exhaust can leak into the crankcase past the piston rings. This air needs to be vented. Typically it is vented into the intake to be recycled through the engine. However that doesn't work for PWS since crankcase pressure must be less than ambient, and injecting the blow-by (air from crank case) before the PWS can cause blockages in the intercooler. However, injecting the blow-by after the intercooler doesn't work since the charge air is at a higher pressure than ambient. Since EGR through a PWS can cause soot to enter the intake system, the oil from the blow-by makes the soot sticky and can clog the air intake and intercooler. This isn't a problem for regular turbocharger since the exhaust and intake streams are separate in the turbocharger[13]. However if the exhaust gas for EGR is pulled before it goes through PWS, it will still be at high pressure and can be routed to intake downsream of intercooler very close to the engine to minimize blockage risk. Unfortunately, that doesn't allow for crankcase pressure to be below ambient. Another solution is to vent the blow-by downstream of the PWS EO port to an ejector that uses a small portion

of the compressed charge air as the driver for the ejector[13]. A filter can be added to the blow-by system if increased emissions are a concern. Schruf and Kollbrunner of BBC presented this solution in 1984 and compared the emissions of the ejector system to the emissions of the typical blow-by system and found that there was not a significant difference between the two systems in the amount of emissions released (less than 14% difference in hydrocarbon emission and less than 10% difference in NO_x, CO, and particulate)[13].

2.6 Turbocharger Integration

Turbochargers and PWSs integrate with the engine in very similar ways and can use the same control features to keep the engine within operating limits. A basic overview of a turbocharger is given in Section 2.6.1 in order to establish a baseline understanding. Both turbochargers and PWSs compress the air being fed to the engine, which increases the temperature of the charge air. The increased temperature of the intake air can cause problems for the engine, so the increase in temperature can be countered with an intercooler, as discussed in Section 2.6.2. Turbochargers and PWSs can both also provide too much pressure at some engine conditions and so can make use of a wastegate, which is discussed in Section 2.6.3. Figure 17 shows how a turbocharger or a PWS integrates with an engine and the location of some of the common control mechanisms. The turbocharger in Figure 17a could easily be replaced by a PWS where the intake feeds the AI port and the AO port goes to the intercooler, while the exhaust gases from the engine go to the EI port then out EO with the wastegate bypassing the EI port and venting exhaust directly to the exhaust system.

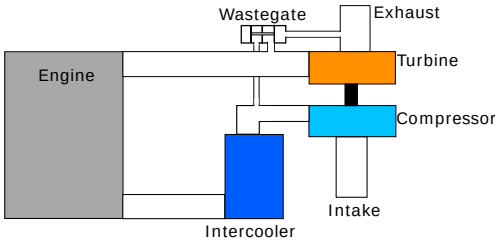

(a) A Turbocharger Integrated with an Engine

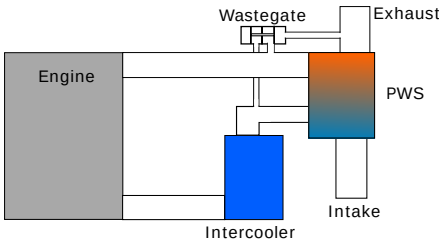

(b) A PWS Integrated with an Engine

Figure 17. How a PWS and Turbocharger Integrate with an Engine

2.6.1 Turbocharger Basics.

In a very generic sense, a turbocharger is a devices that uses a turbine to drive a compressor that in turn is used to increase the pressure of the charge air being fed to a device. The charged device is typically an internal combustion engine, but could also include air refrigeration cycles or fuel cells[27]. For automobile applications, the turbine and compressor in a turbocharger are centrifugal instead of axial due to the limited amount of space inside the engine compartment and the simpler design of a single stage centrifugal compressor and turbine instead of multistage axial components. A turbocharger uses the turbine to extract energy from the hot exhaust gases from the engine. The turbine powers the compressor that takes in ambient air and compresses it before sending the compressed air to the engine. The turbine and compressor are mounted on a shaft with bearings contained in a central housing between the turbine and compressor. The high rotational speeds of the turbocharger require that the bearings be cooled, and this is usually accomplished by a flow of engine oil through the central housing[27].

For an automobile engine, adding a turbocharger increases the power output of the engine. The goal of increasing the power outputs could simply be to get more power out of a given engine or it could be to recover the power lost due to an increase in altitude. However, adding a turbocharger also can increase fuel consumption com-

pared to a naturally aspirated engine of the same size[28]. However, a turbocharger allows for use of a smaller engine to achieve a given power output. The use of the smaller engine to have the same power output is how a turbocharger can reduce fuel requirements. There is a limit to how small the engine and turbocharger can get. As the size of the engine and turbocharger decrease, the efficiency drops due to the small scale of the turbocharger components[1, 15]. This is one area where a PWS can have a significant advantage over a turbocharger. Since the PWS does not use mechanical components to exchange energy between the exhaust and fresh air, it avoids the scaling efficiency losses encountered by the turbocharger which was discussed in Section 2.1.

2.6.2 Intercoolers.

As in all compressors, the temperature of the air exiting the compressor of the turbocharger is significantly higher than the temperature of the ambient air that is brought in, possibly by 360 Kelvin or more[28]. The increase in temperature of the charge air increases the risk of detonation and pre-ignition in the cylinder. One way to control the temperature of the intake air is by adding an intercooler. An intercooler is a heat exchangers that is inserted downstream of the compressor outlet, or the AO port in a wave rotor, and upstream of the engine that cools the intake air charge before it enters the engine. The cooling of the charge air also increases its density with the added benefit of increasing the power output of the engine slightly[28]. Both a turbocharger and a PWS would benefit from the use of an intercooler to cool the charge air that is sent to the engine since both will increase the temperature of the compressed air. Intercoolers are more important for spark ignited engines since pre-ignition of the fuel is a bigger problem than in diesel engines, though both types of engines would benefit from the increased charge air density provided by the

intercooler.

2.6.3 Wastegates.

For internal combustion engines, it is necessary to limit the maximum amount of boost pressure provided to the engine in order to avoid detonation, pre-ignition, and other problems that would lead to the destruction of the engine[28]. One of the most practical ways to control the maximum boost pressure is to use a wastegate. The wastegate works by using the pressure of charge air downstream of the compressor to control a valve that allows some of the exhaust gas to bypass the turbine. This is helpful for engine conditions where there is a lot of exhaust gas at high temperature passing though the turbine, which then causes the compressor to provide too much boost pressure to the engine, which can cause detonation, pre-ignition, and engine damage. By allowing some of the exhaust gas to bypass the turbine, there is less energy available for the turbine to extract. The turbine then slows down, which in turn causes the compressor to slow and provide less boost to the engine.

2.7 PWS Integration

A PWS integrates with an engine in a very similar way as a turbocharger. However, there are some additional considerations for PWS integration. One of these considerations is the flow restrictions caused by the intake and exhaust systems, specifically the pressure drop caused by pulling air in through the air filter and intake manifold and the pressure increase caused by pushing the exhaust out the exhaust system. The efficiency of the PWS operation is sensitive to these pressures, and these flow restrictions can be combined into a "total flow restriction coefficient" ζ_{14} described in Equation 7. In Equation 7, P_1 is the difference in static pressure across the air intake system, i.e. the pressure at the entrance to the air intake minus the

pressure at the AI port. P_4 is the difference in static pressure across the exhaust system, which is the pressure at the EO port minus the pressure at the tailpipe exit. In the denominator, ρ_1 is the density of the inlet air, and C_1 is the velocity of the inlet air at the inlet to the PWS[13]. Figure 18 shows how ζ_{14} affects the efficiency by plotting efficiency versus engine speed for two different ζ_{14} values. Lower ζ_{14} values mean that there is less pressure loss across the intake system and less back pressure on the exhaust system, which results in an increase in efficiency.

$$\zeta_{14} = \frac{P_1 + P_4}{\frac{\rho_1}{2} * C_1^2} \tag{7}$$

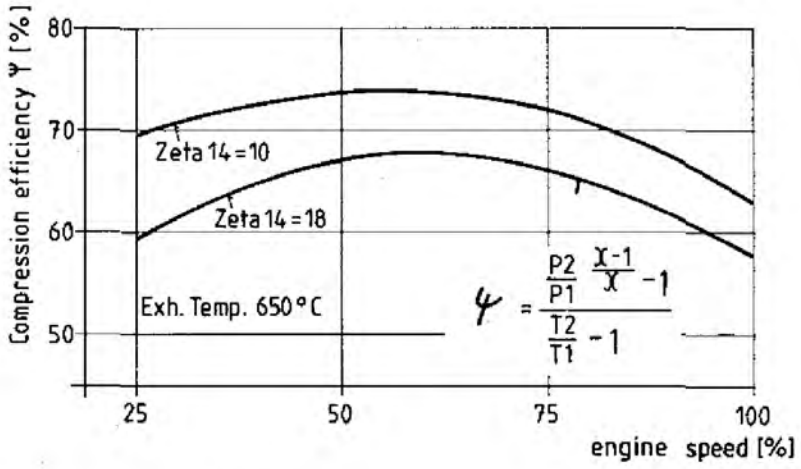

Figure 18. Efficiency vs. Engine Speed for Two Different ζ_{14} Values[13]

Another consideration is the effect that EGR through the PWS has on the air intake system, especially if an intercooler is used. Soot from EGR can build up in the intercooler and on the tubing in the intake, but for dry soot, the deposits flake off after some initial build so that the cooling efficiency of the intercooler and the flow restriction in the intake tubing stabilize after some break-in period[13]. However, if the EGR is contaminated with oil, such as from the crankcase ventilation system, the oil makes the soot sticky and can clog the intake system, as discussed previously in Section 2.5.1.

III. Experimental Setup

Two different test facilities were used to test the PWS. The first series of tests occurred in H-Bay with the purpose of understanding how the PWS performed when coupled with an actual engine. The test facility and the equipment that goes with it is discussed in Section 3.1. The integration of the PWS with the diesel engine is discussed in Section 3.4 and the instrumentation and data acquisition is discussed in Section 3.3. The second series of tests were conducted in D-Bay with the purpose of establishing baseline performance values for the PWS and comparing different endwall configurations. The D-Bay test facility is described in Section 3.5. The integration of the PWS into the test facility in D-Bay is discussed in Section 3.6.2. Most of the control programs and instrumentation for the wave rotor portion of the setup was common between the two facilities and is discussed in Section 3.2, while the control programs specific to each test facility are discussed in their respective test facility sections.

3.1 H-Bay Test Facility Configuration

The first test facility was located at AFRL at Wright-Patterson AFB in H-Bay. The facility is set up to test internal combustion engines and was configured with a diesel engine connected to a dynamometer and an altitude plenum. Each of these features are discussed in the following sections.

The test facility has the ability to simulate pressure at various altitudes by using a blower to pull air out of a plenum with a valve restricting the intake, reducing the pressure inside the plenum to a value less than the ambient pressure in the test cell, as seen in Figure 19. The plenum's intake is through an air filter and pulls air from the test cell, so the temperature of the intake air is nearly the same as the ambient air

in the test cell. The pressure inside the altitude plenum can be adjusted by increasing or decreasing the blower speed or by closing or opening the valve.

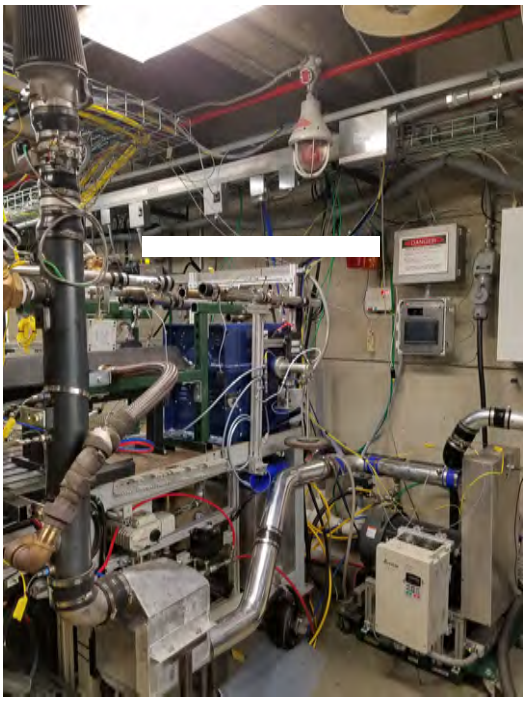

Figure 19. The Altitude Plenum and Other Test Facility Features

The engine used in this research is a three-cylinder,four stroke, IDI industrial diesel engine, shown in Figure 20. More information on diesel engines can be found in Section 2.5. This engine was chosen because it met the requirements for testing and also required minimal setup since its was already mounted on the test stand by AFRL. The engine used in this research had a displacement of 898cc and produced a maximum of 16kW at the maximum engine speed of 3,200 rpm[14]. Then engine was 18.4 inches long by 16.6 inches wide by 21.4 inches high and weighed 72 pounds. When the PWS is mounted on the engine, the exhaust is routed from the manifold to the EI port of the PWS with a flex line, which can be seen in Figure 32 in Section 3.4.3.

The engine's drive shaft is connected to a Dyne Systems DM 8060 eddy current dynamometer and can also be seen in Figure 19. The dynamometer is water cooled

Figure 20. The Kubota D902 Engine[14]

and has a limit of 75 horsepower and 12,000 rpm. The engine maximum rpm of 3200 and the maximum expected power of 40 horsepower are well within the limits of the dynamometer.

3.2 Data Reduction Process

There are two data acquisition programs used in this research. The first program was called "Brayton Rotor" and it monitored the burner status and recorded the fuel mass flow and burn inlet and exit temperatures. The Brayton Rotor program was loaded onto the docked laptop in the control room and was connected to a National Instruments cDAQ-9188 data acquisition board that was mounted onto the test cart. The instrumentation then connected to the cDAQ-9188 board. The second program was called "WaveRotor-Kubota Closed Loop4" and it controlled and monitored the performance of the wave rotor, which included the temperature at each port, the static pressures at each port, and the mass flows at the AI, AO, and EO ports. The original file for the wave rotor control program was loaded onto Apple computer.

However, this computer was simultaneously being used for two other experiments, so the control program was converted to an executable that could run on any computer that had the LabVIEW 2015 runtime environment and the NI Measurement and Automation Explorer loaded onto it. The executable was quickly loaded onto an available computer so that test could proceed. Any changes to the executable program require that the original file be edited and the executable rebuilt. The mass flow at the EI port was set as the mass flow through the burner and controlled with the facility control system.

The program that monitored the burner output data as an Excel file that could be transferred to other computers via an AFRL approved removed hard drive or removable cd drive. The output file includes a time stamp that was used to synchronize the file with the data output from the wave rotor control program.

The wave rotor control program output two types of data files. The first type of data file was a text file. This text file was populated by pressing the "Take Data" button in the control program. The data written to the file was a five second average for each parameter that is recorded. The data was received at a rate of 5 Hz, so 25 readings were averaged to generate one data point. The data was recorded in a tab delimited format that is easily imported into Excel. The other type of data file output by the wave rotor control program is a *.tdms file that was imported to Excel using the *.tdms imported add-in available from National Instruments. The *.tdms file was a continuous recording of all the recorded parameters from the time the program starts until the program was stopped. Both the text file output and the *.tdms file have a time stamp that was used to synchronize with the other data files. The data was then analyzed in Excel and Matlab.

The mass flow through the wave rotor ports was calculated by the wave rotor control program and output in the *.tdms file. However, it was not output in the text

file. The mass flow for the data points in the text file could either be easily pulled from the *.tdms file using the time stamps in each file or calculated directly using the pressure readings recorded in the text file by using Equation 8.

$$\dot{m} = A_{throat} C_d P_0 \pi^{1/\gamma} * \sqrt{\frac{2\gamma}{\gamma - 1} \frac{g_0}{RT} [1 - \pi^{(\gamma-1)/\gamma}]} * 60 \tag{8}$$

where $\pi = 1 - \frac{\Delta P}{P_0}$. The γ and R values are the ratio of specific heats and gas constant for the fluid flowing through the venturi. In this case γ and R are the properties of air if the venturi is attached to the AI or AO port and the properties of the exhaust gas if the venturi is attached to the EI or EO port. In Equation 8, g_0 is the acceleration due to gravity and T is the total temperature measured at the venturi entrance while P_0 is the total pressure of the flow through the venturi.

The pressure ratio of the AO port to the AI port is referred to as the Air Pressure Ratio (APR) and was calculated using Equation 9. The pressures in Equation 9 are total pressures measured with a pitot tube in the ducts connecting to each port. The compression efficiency was calculated using Equation 5 discussed in Section 2.4.1 and used the total pressures and RTD probe temperatures from the AI and AO ports.

$$APR = \frac{P_{t_{AO}}}{P_{t_{AI}}} \tag{9}$$

3.3 Instrumentation, Uncertainty, and Repeatability

The H-bay and D-Bay test facilities used the same data acquisition system that was described in Section 3.2. Two types of pressure transducers were used in the test setup, the Honeywell TJE with a 50 psi absolute range and the Omega PX429-050A5V that also had a 50 psi absolute range. The Honeywell TJE has an accuracy given by the manufacturer of 0.10% of full scale, and the Omega has a published accuracy of 0.08% Best Straight Line (BSL) maximum. The Omega transducers come calibrated

from the factory such that an output of 0 volts corresponds to 0 psi and an output of 5 volts, or the maximum voltage, corresponds to the maximum pressure rating of the transducer, in this case 50 psi absolute, or 344,700 Pa. The temperature measurements on the exhaust side were taken using Omega K-type thermocouples that had an accuracy of 2.2°C or 0.75%, whichever is greater. The temperatures on the air side were measured with Omega general purpose RTD probes that had an accuracy of $\pm(0.15+0.002*t)$ where t is the temperature in Celsius. The temperature and pressure measurements were then fed into Equations 5, 8, and 9 to calculate the compression efficiency, mass flow, and APR.

The accuracies of the compression efficiency, mass flow, and APR were determined using the perturbation method[29]. Each input to Equations 5, 8, and 9 were adjusted one at a time by the given accuracy of each instrument. A new value was then calculated using the perturbed input. Next the difference between the original and perturbed calculation was found for each perturbed input and the uncertainty calculated by finding the square root of the sum of the squares of the differences. A sample calculation is shown for the APR uncertainty in Equations 10 to 12. The uncertainty for the compression efficiency, mass flow, and APR were calculated for each data point in the repeatablility analysis and then averaged to determine an overall uncertainty for that calculation.

$$\frac{P_{t_{AO}} + \Delta P_{t_{AO}}}{P_{t_{AI}}} = \frac{(24.69 + 0.020)}{14.20} = 1.740 = APR_{P_{t_{AO}}} \tag{10}$$

$$\frac{P_{t_{AO}}}{P_{t_{AI}} + \Delta P_{t_{AI}}} = \frac{24.69}{(14.20 + 0.011)} = 1.739 = APR_{P_{t_{AI}}} \tag{11}$$

$$\begin{aligned} APR\ Uncertainty &= \sqrt{\left(APR - APR_{P_{t_{AO}}}\right)^2 + \left(APR - APR_{P_{t_{AI}}}\right)^2} \\ &= \sqrt{(1.738 - 1.740)^2 + (1.738 - 1.739)^2} = 0.00197 \end{aligned} \tag{12}$$

The efficiency calculation used data from the RTD probes in the AI and AO ports

as well as the total pressure sensors in each port. Equation 13 shows one of the perturbations used to calculate the uncertainty in the compression efficiency. The efficiency equation was perturbed by adjusting each of the temperature or pressure measurements by the instrument's accuracy, and the amount of the perturbation was referred to as ΔP or ΔT, as appropriate. Sample calculations for ΔP_{AO} and ΔT_{AI} are shown in Equation 14. The other Δs were found using the same equations but with the appropriate sensor measurement substituted. After determining the uncertainty for the repeatability data points, the uncertainties were averaged for each calculation to determine an average uncertainty. The average uncertainty in the APR calculation was 0.0016 psi and the average uncertainty for the compression efficiency was 0.08%.

$$\eta = \frac{\left(\frac{P_{AO}+\Delta P_{AO}}{P_{AI}}\right)^{(\gamma-1)/\gamma}}{T_{AO}} \tag{13}$$

$$\begin{aligned} \Delta P_{AO} &= 0.0008 * P_{AO} \\ \Delta T_{AI} &= 0.15 + 0.002 * T_{AI} \end{aligned} \tag{14}$$

During each plain endwall test run, data was taken at a TEI of 811K, a rotor speed of 26,000 rpm, and an AO valve position of 1 to determine the repeatability of the test runs. These parameters were chosen for the repeatability analysis since they were also the main parameters used to measure wave rotor performance. Figure 21 shows the compression efficiency, APR and AO mass flow for each repeated data point. The compression efficiency, mass flow, and APR were calculated using the equations and inputs described in Section 3.2. In Figure 21a, there is a noticeable change in the efficiency value between points two and three. For points one and two, the rotor speed was about 500 rpm higher than the rotor speed for points three through five. The bin size used in the data analysis for the rotor speed was 1,000 rpm wide so that data included in the 26,000 bin could range from 25,500 to 26,500. Therefore, it was not

uncommon for the rotor speed to vary somewhat within a "constant" rotor speed bin, and more precise uncertainty calculations may be made by reducing the rpm bin size. Based on Figure 21a, the change in the efficiency due to the rotor speed change was only about 2%. This is a small change compared to the magnitude of the changes in compression efficiency that occurred during the parameter sweeps conducted during testing. Similar results were seen in the plot of the APR for the repeated data points, shown in Figure 21b, where there is a jump in the APR value when the rotor speed changes. For both the efficiency and APR charts, the rotor speed only varies by about 50 rpm within the two sets of constant rpm values.

For the AO mass flow calculation, the value varied by as much as 7.8% of the total AO mass flow for the constant rotor speed, TEI, and AO valve position. Also, the AO mass flow does not show the same jump between two different constant values when the rotor speed changed by 500 rpm as the efficiency and APR did. This suggests that the AO mass flow may be sensitive to a fourth parameter that was not captured or that the mass flow is very sensitive to minor changes in the other parameters that were captured. Upon examination of the mass flow data, it was determined that the pressure differential on the venturi was often at or below the published accuracy of the pressure transducer. This made the mass flow measurement much more sensitive to any noise in the system, whether it was variation in the flow through the venturi or electrical noise in the the signal cables. Therefore, the reliability of the mass flow calculations is reduced. This problem could be avoided by use of a smaller venturi or instruments with increased sensitivity.

3.4 Engine Integration

The PWS was integrated into the engine similarly to how a turbocharger would be integrated into the engine. The integration method was changed twice as under-

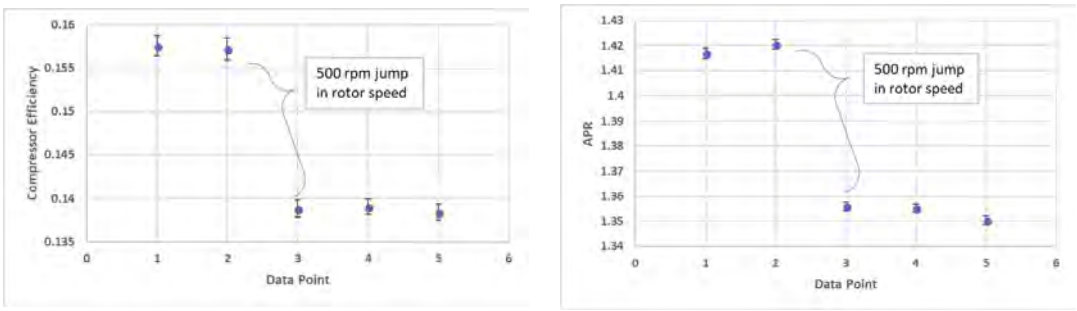

(a) Compressor Efficiency

(b) APR

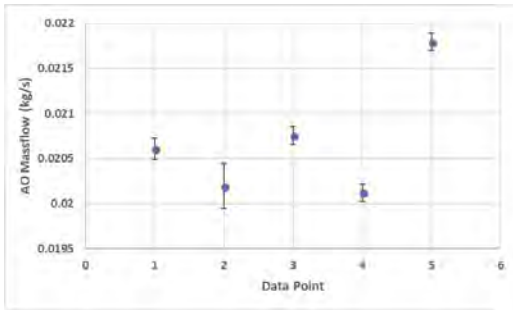

(c) AO Mass Flow (kg/s)

Figure 21. The Compression Efficiency, APR, and AO Mass Flow for the repeated data points

standing of the system increased. The first iteration was a Open Loop Configuration, discussed in Section 3.4.1. Second was an initial Closed Loop Configuration, discussed in Section 3.4.2. Finally additional sensors and controls were added and the layout was changed slightly. These changes are discussed in Section 3.4.3.

3.4.1 Open Loop Configuration.

Figure 22 shows the layout of the open loop configuration. In the open loop configuration, the charge air from the AO port did not go to the engine. Instead, it was routed through a gate valve that controls the back pressure. This was used to simulate the back pressure created by the engine in the closed loop configuration while allowing the engine to breathe naturally. By regulating the back pressure to the AO port, the mass flows into and out of the PWS can be balanced and the proper wave structure created. The AO gate valve was a W.E. Anderson GV121 globe valve

and was controlled by a W.E. Anderson EVA2 electric actuator. The globe valve has an internal disk that is raised or lowered by the electric actuator via a stem that connects the actuator assembly to the disk inside the valve. The disk sits on an opening inside the globe valve so that when the disk is lowered onto the opening the valve is closed and when the disk is raised the valve is opened. The electric actuator used in this research required a 24V power supply and a 0-10V control signal where 0V corresponded to the disk being fully lowered, which was the fully closed position, and 10V corresponded to the disk being fully raised, which was the full open position and the disk position linearly varying with the voltage input. The electric actuator could receive control inputs at 1/10V resolution, which meant that each 1/10V input corresponded to 1% change in the valve position.

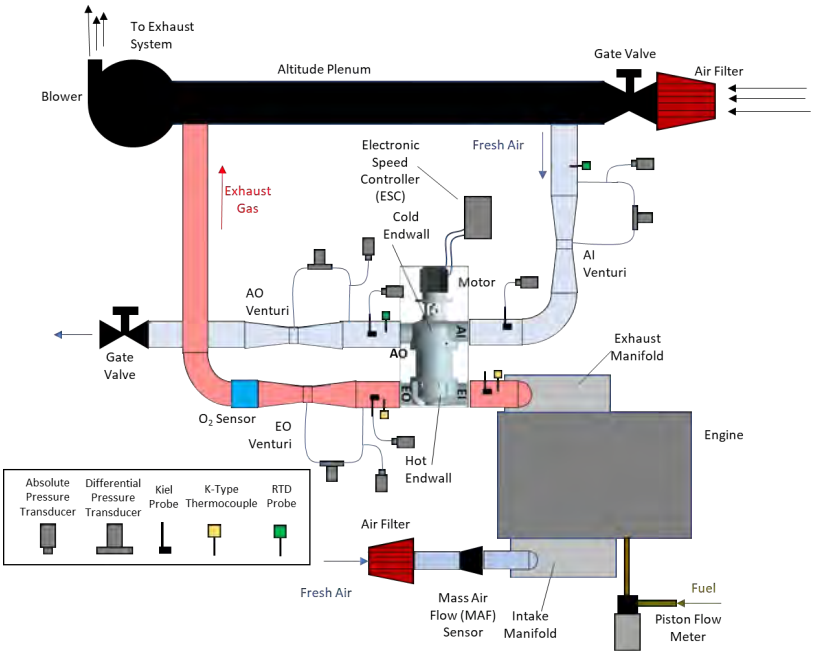

Figure 22. Schematic of the Open Loop Test Setup

In Figure 22, the AO port vents to the atmosphere through a valve that controls the back pressure at the AO port. The exhaust gas from the engine is routed directly to the EI port so that the temperature and pressure conditions in the EI port match

the design point conditions. For the open loop configuration, the engine air intake is separate from the PWS, and the engine intake mass flow is measured with a Mass Air Flow (MAF) sensor. The AI port of the PWS intakes air from the altitude plenum that is part of the test cell. The mass flow through the AI port is measured with a venturi. This configuration is called open loop because the AO port does not connect to the engine's intake manifold. Figure 22 also shows the pressure and temperature sensor locations used in the open loop configuration. The sensors are discussed further in Section 3.3.

3.4.1.1 Inital Open Loop Results.

The initial data collected by Mataczynski and presented by Reinhart in [21] was analyzed in more depth in preparation for this research. Figure 23 shows the efficiency plotted against the pressure ratio across the engine, which is P_{tEI}/P_{tAO}. The efficiency was calculated using Equation 6. By plotting the data this way, a general trend of increasing efficiency as the ratio approaches one can be seen. The data in this plot includes different parameter sweeps, so the next step is to bin the data by PWS speed and EI temperature.

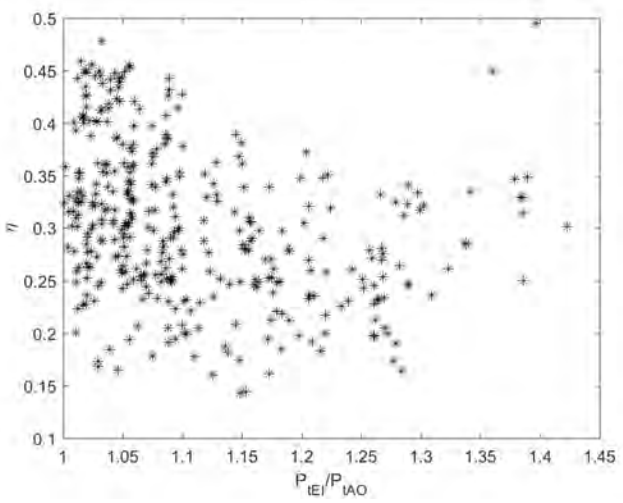

Figure 23. Efficiency vs. P_{tEO}/P_{tAI}

Figure 24 and Figure 25 show the same data as plotted in Figure 23 binned by PWS speed and by EI temperature. By looking at the EI temperature bins in Figure 24, it can be seen how there are points of constant EI temperature where the efficiency is changing along a nearly vertical line. The temperature bins range from 616 K to 894 K, separated into bins of 56 K. Figure 25 bins the data by rotor speed, with the bins ranging from 23,000 rpm to 30,000 rpm, separated into bins of 1,000 rpm. Binning the data allows for the identification of groups of data points with common parameters. By looking at the corresponding data points in Figure 25, it can be seen that the PWS speed changes along the line of constant EI temperature, with the efficiency increasing as the rotor speed increases. One of the corresponding patterns is circled in red on Figures 24 and 25. The data can then easily be organized into groups of constant EI temperature and pressure ratio and the efficiency plotted against the rotor speed, or grouped by constant rotor speed and pressure ratio and the efficiency plotted against EI temperature.

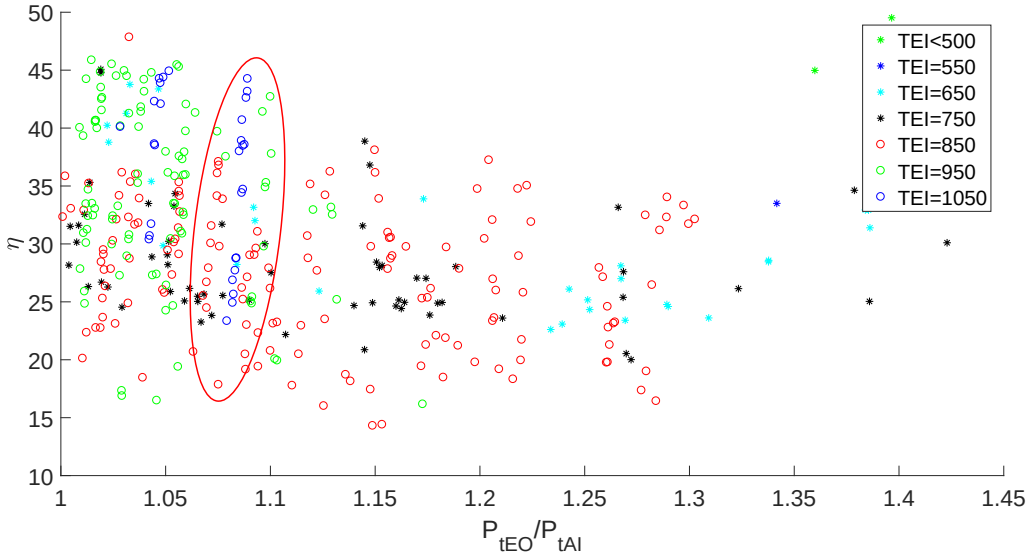

Figure 24. Efficiency vs. P_{tEI}/P_{tAO} Binned by Exhaust Temperature

Figures 26a and 26b show how compression efficiency changes with EI temperature for different constant rotor speeds and pressure ratios of P_{tEI}/P_{tAO}. These figures

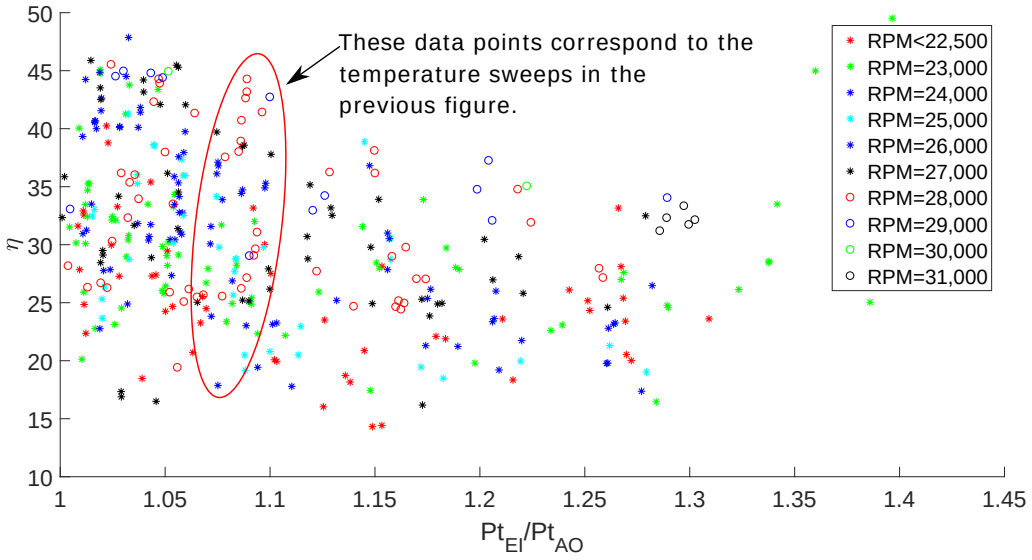

Figure 25. Efficiency vs. P_{tEI}/P_{tAO} Binned by Rotor Speed

allow for the comparison of the wave rotor performance as the EI temperature for different sets of constant rotor speed and pressure ratio. Figure 26a shows how the compression efficiency changes with EI temperature for $P_{tEI}/P_{tAO} = 1.1$, and Figure 26b shows the same thing for $P_{tEI}/P_{tAO} = 1.05$. In Figure 26a, it can be seen that for the lowest rotor speed bin, the efficiency is higher than for either higher rotor speed bin, but the efficiency decreases as EI temperature increases. Conversely, the higher EI temperature bins start at lower efficiencies, and the efficiency increases as EI temperature increases. The highest rotor speed bin reaches the highest efficiency at the highest EI temperature. Since the EI temperature influences the wave speed inside the rotor, it can be seen that matching the rotor speed to the EI temperature is important for peak PWS performance since the rotation of the rotor and the speed of the wave inside the rotor must be matched so that the wave impacts the opposite endwall with the correct timing.

The same importance of matching the rotor speed to the EI temperature is seen when the efficiency is plotted against the rotor speed for sets of constant EI temperature. Figures 27a and 27b show this relationship. In Figure 27, both charts show

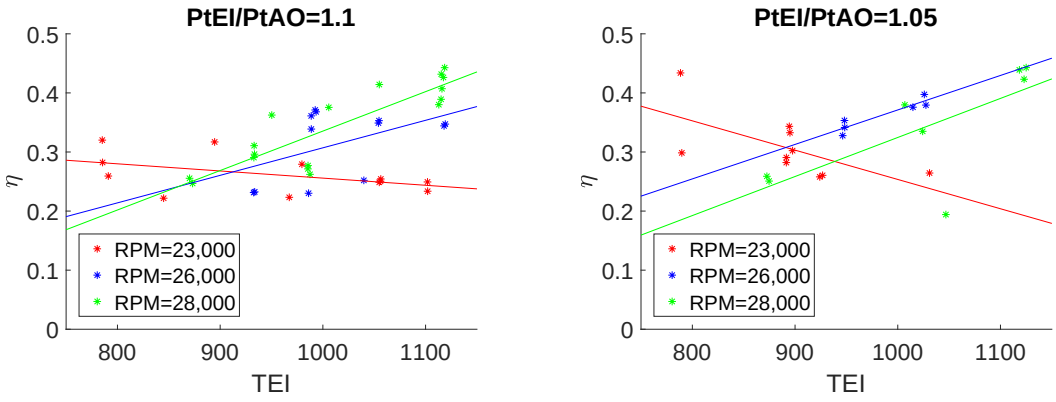

(a) $P_{tEI}/P_{tAO} = 1.1$ **(b)** $P_{tEI}/P_{tAO} = 1.05$

Figure 26. Compression Ratio vs. RPM for Different Pressure Ratios

how the lower EI temperature bin has higher efficiencies than the higher EI temperature bins, and how the efficiency of the lowest EI temperature bin decreases as rotor speed increases. Conversely, for the higher EI temperature bins, the efficiency starts lower and then increases as the rotor speed increases. Since a higher EI temperature corresponds to a higher wave speed, a higher rotor speed is needed to ensure that the wave structure is set up correctly. Presumably, the efficiencies of the higher EI temperature bins would reach a peak and then begin to decrease if the rotor speed continued to increase past the charted values in Figure 27.

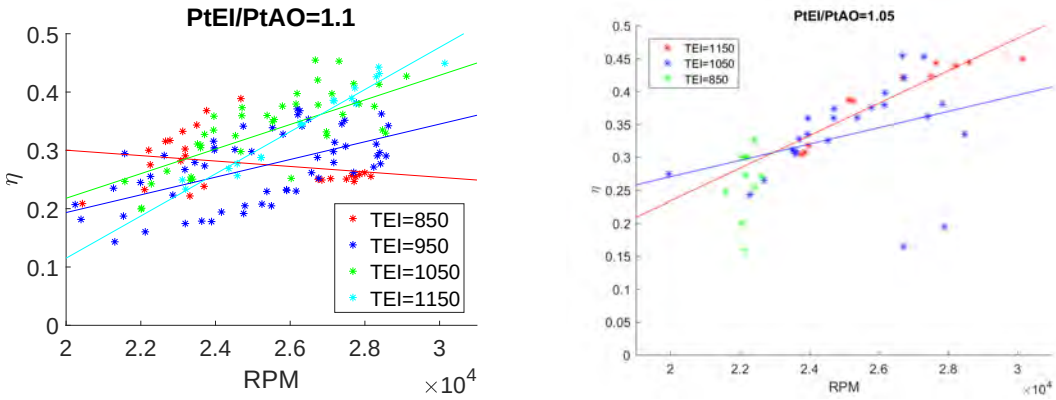

(a) $P_{tEI}/P_{tAO} = 1.1$ **(b)** $P_{tEI}/P_{tAO} = 1.05$

Figure 27. Compression Ratio vs. EI Temperature for Different Pressure Ration

Another way to plot the compression efficiency of the PWS is against the mass

flow through the EI port. This plot can be seen in Figure 28. When the data is plotted this way, clear lines of data binned by mass flow at the EI port present themselves. This data can then be binned by EI temperature and rotor speed and compared for different mass flows. The general trend of the data presented in Figure 28 shows the efficiency increasing for increased EI temperature and rotor speed, though further breaking down of the data makes this more clear.

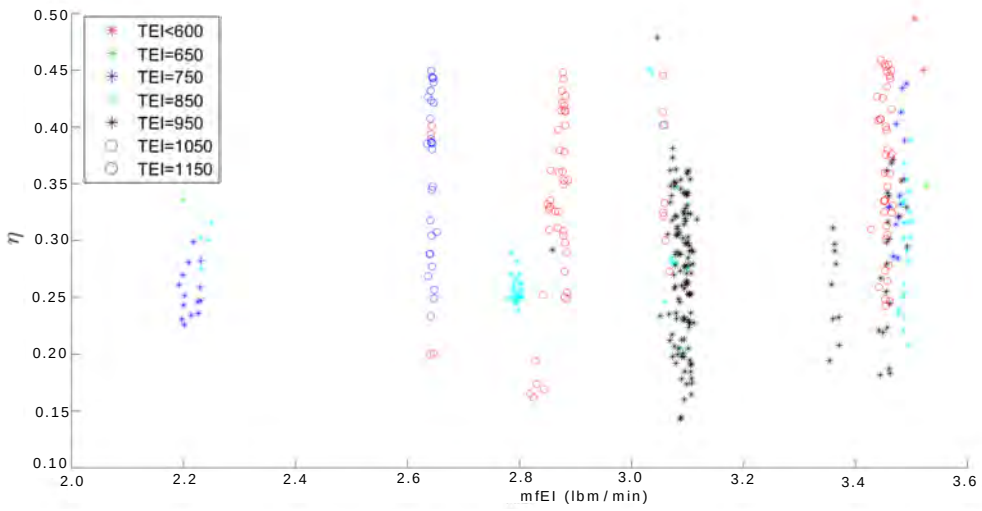

(a) Data Binned by T_{EI}

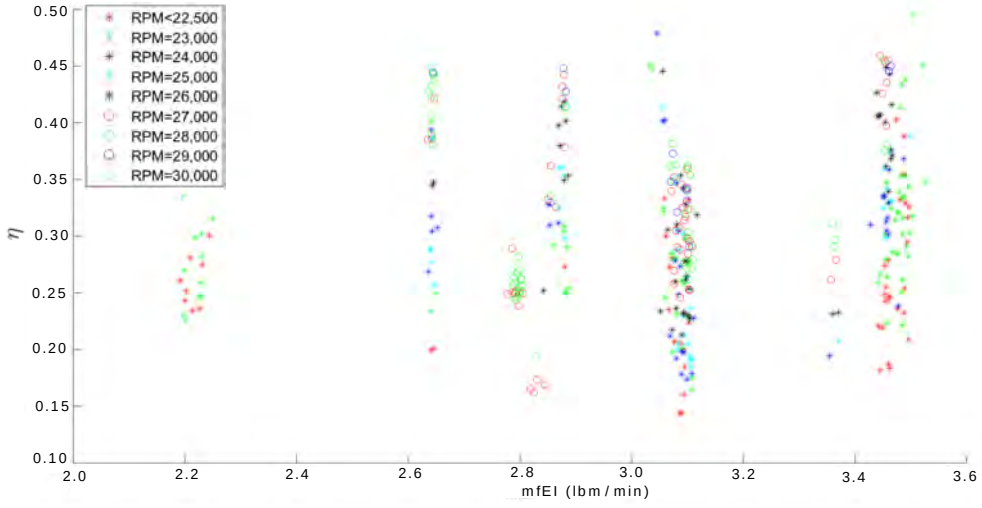

(b) Data Binned by Rotor Speed

Figure 28. Compression Efficiency vs. Mass Flow through EI

By looking at two different exhaust mass flows, the trends as efficiency changes

with rotor speed for different EI temperature bins can be compared. For both EI mass flow cases presented in Figure 29, the efficiency increases as the rotor speed increases, though the lowest temperature bin is still limited to data points with low rotor speed. Since there are no definite differences in the trends between the two exhaust in mass flows presented, it can be determined that the exhaust mass flow does not have a significant impact on the efficient operation of a PWS, assuming that the mass flows are balanced such that significant EGR is not occurring. As shown in Figure 29, the most efficient operation of operation of a PWS is with a high rotor speed with a matched high EI temperature.

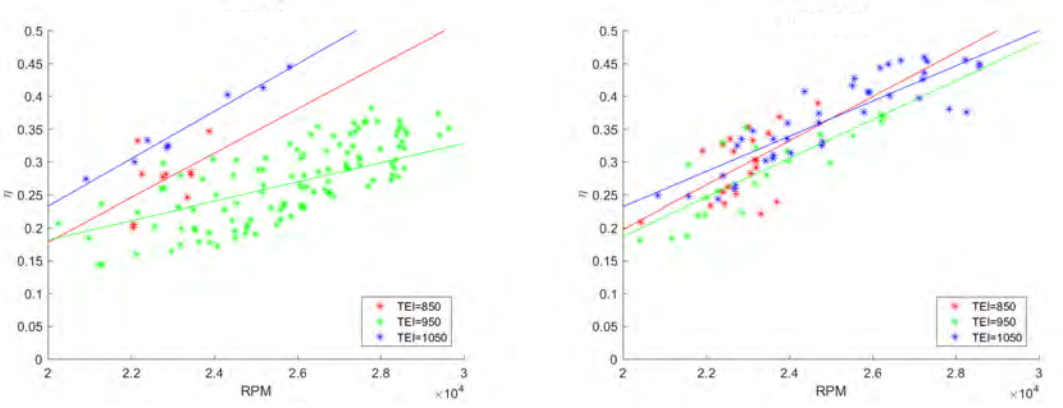

(a) Mass Flow Equals 3.1 lbm/min **(b) Mass Flow Equals 3.45 lbm/min**

Figure 29. Compression Efficiency vs. Rotor Speed for Different EI Mass Flows

3.4.2 First Closed Loop Configuration.

Figure 30 shows the layout of the closed loop configuration. In the closed loop configuration, the charge air from the AO port is fed to the engine so that the pressure inside the engine is boosted. Except for the extra ducting and data acquisition equipment, this configuration is nearly how it would be installed on a production engine. Additional components that could be included in a production engine are an intercooler or a wastegate.

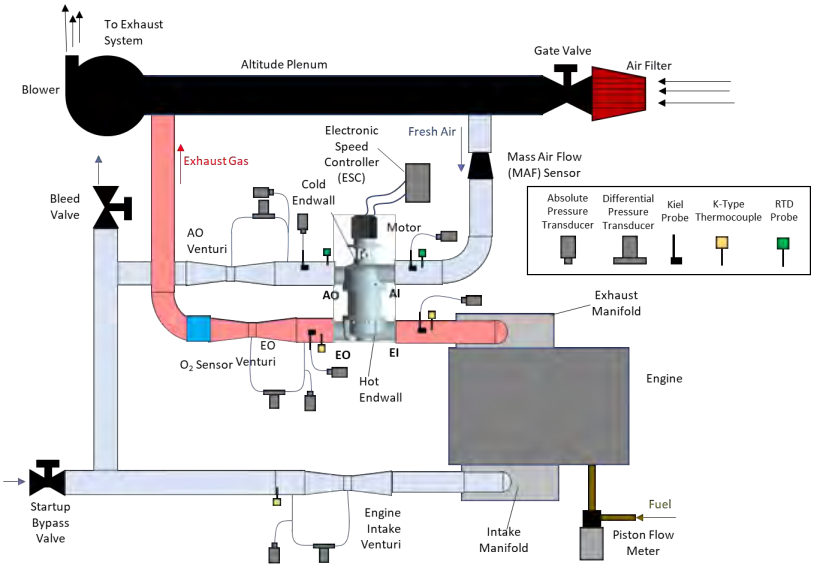

Figure 30. Schematic of the First Closed Loop Setup

In Figure 30, the AO port is connected to the engine's intake manifold, and the EO port is connected to the engine's exhaust manifold so that the only intake is through the PWS's AI port and the only exhaust is out the PWS's EO port. Both of these ports are connected to the lab's altitude plenum so that pressures at different altitudes can be simulated. The duct from the AO port to the engine has a valve that can function similar to a wastegate. Wastegates are discussed in Section 2.6.3. This valve is controlled by the testers whereas a wastegate on a production engine would function automatically. The duct between the AO port and the intake manifold also has a safety valve that prevents over pressurizing the engine. Figure 30 also shows the locations of the venturis that are used to measure the mass flows. The venturis measure the mass flows through the AO, EI, and EO ports, while the mass flow through the AI port was measured with a MAF sensor. The sensor locations for the temperature and pressure measurements are also shown in Figure 30. The temperature in the AO and AI ports were measure using Resistive Temperature Device (RTD) sensors while the temperatures at the EI and EO ports were measure using K-type thermocouples since the K-type thermocouples have a higher temperature tolerance

than RTDs.

3.4.3 Second Closed Loop Configuration.

Figure 31 shows the second orientation of the closed loop configuration. This configuration added oxygen sensors and a wastegate, and also rearranged some of the venturi locations. The oxygen sensors allowed for determining the Air to Fuel Ratio (AFR) of the intake or exhaust. By comparing the two oxygen sensor measurements, it can be qualitatively determined how much mixing of the intake and exhaust is occurring in the PWS. The venturis now measure the mass flow at the AO, EI, and EO port, while the mass flow to the AI port is measured with a MAF sensor. The AI port is also disconnected from the altitude plenum. This allows for the separate control of the pressures at the AI and EO ports. Independently controlling the pressures at the AI and EO ports allows for the control of the total flow coefficient, ζ_{14}, which is an important factor in PWS performance and was discussed further in Section 2.7. Figure 32 shows the PWS integrated with the diesel engine in the second closed loop configuration.

3.5 D-Bay Test Facility Configuration

The second series of tests were conducted at AFRL's Detonation Engine Research Facility known as D-Bay. The test facility includes several different tools for conducting a wide variety of tests. The relavent parts of the test facility are shown in Figure 33. This research made use of the facility compressed air supply and the can combustor designed by McClearn[7]. The can combustor, or burner, is discussed in more detail in Section 3.6.1. The compressed air supply runs from the facility compressor to piping which feeds compressed air to several different test rigs. This research used the feed line that routed to the T-63 test stand, though the modified T-63 engine was

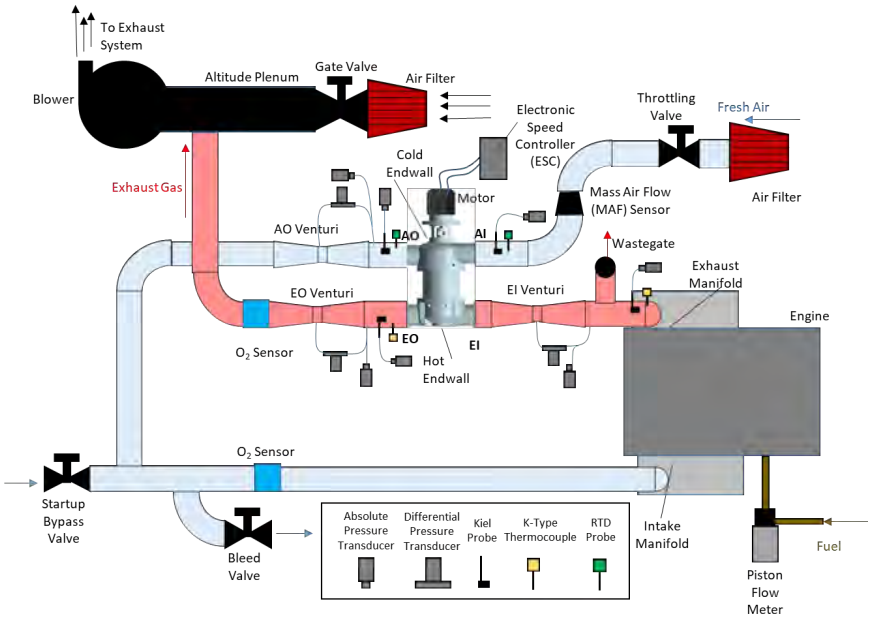

Figure 31. Schematic of the Second Closed Loop Setup

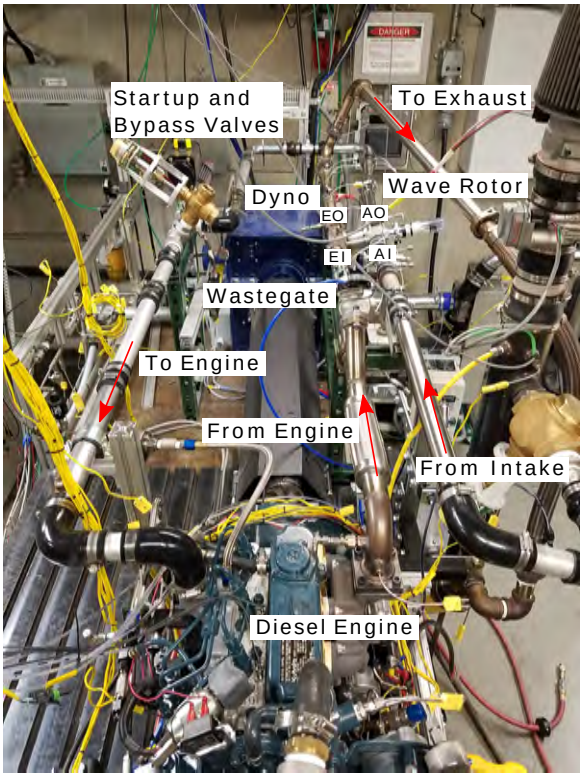

Figure 32. The PWS Integrated with the Diesel Engine in Closed Loop Configuration

not used for these tests. Since the air supply was routed through existing test stands, the existing control program for the test facility was used to control the air supply and the safety valves on the fuel lines.

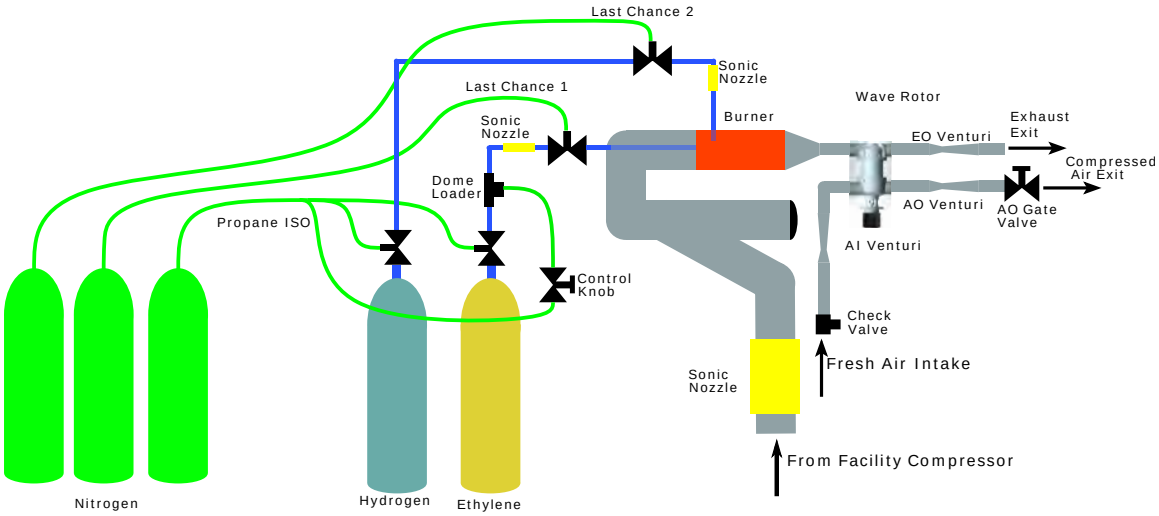

Figure 33. The Test Facility in D-Bay

The fuels used in these tests were ethylene and hydrogen. The fuel was stored in pressurized bottles and was routed to the test stand with metal 1/4-inch tubing. Two safety valves were used on each fuel line and were interlocked with the test bay door so that no fuel could flow while the door was open. One safety valve was located on each fuel line at the connection to the fuel bottle. The safety valves were connected to the PROPANE ISO safety valve button in the control room. The second pair of safety valves were located on the test stand near the test rig, one on each fuel line. The secondary safety valves were connected to the NOMAD/LAST CHANCE 1 and 2 safety valve lines. These lines were controlled by the facility control program as well as having a physical button that needed to be turned on in the control room.

The ethylene line had a third valve that is used to control the pressure in the ethylene line, and therefore the flow rate of the ethylene fuel. This control valve used pressure from the PROPANE ISO line to feed a manual control knob in the control room. This control knob regulated the pressure to a dome loader pressure regulator

that would take the input pressure from the control room and allow a corresponding pressure into the ethylene line. Effectively, this controlled the mass flow of ethylene fuel by controlling the pressure in the ethylene fuel line. The ethylene control line in the control room also had a manual shutoff valve that needed to be opened before pressure could be applied to the dome loader to increase the fuel flow. If the manual shutoff valve was opened while the control knob was set to allow pressure to flow to the dome loader, the pressure to the dome loader would increase suddenly, which in turn would cause a sudden increase in fuel flow rate to the burner. This condition should be avoided and requires that the control knob be checked in the off position before the manual shutoff valve was opened.

3.6 Burner Open Loop Configuration

Primary testing of the wave rotor was accomplished using the setup shown in Figure 35. This configuration was an open loop configuration and can be converted to closed loop by connecting the AO port to the burner inlet. The hot exhaust gases were supplied from the burner used by McClearn and Lapp that used facility air to burn a mixture of ethylene and hydrogen. The burner setup is described in Section 3.6.1, and the wave rotor setup with the burner is described in Section 3.6.2

3.6.1 Burner Setup.

The burner used in this research was the same that was built by McClearn and used by Lapp. The burner was set up and tested to confirm that it would operate in the required range before the wave rotor was integrated. The burner setup is shown in Figure 34. The burner test setup used air supplied from the facility. Ethylene was the primary fuel with a small amount of hydrogen added to aid with flame stability, about 5.57e-5 kg/s. For this setup, the hydrogen torch served the dual purpase of

initial ignition of the fuel and the injection of the hydrogen for flame stability. In Figure 34, the path of the air through the burner is shown by the red arrows. The air from the facility compressor enters on the left then was routed to the burner. The ethylene injector enters the setup upstream of the burner and extends inside the duct to the burner inlet. Not pictured in Figure 34 is the reducer that reduces the pipe diameter to match the wave rotor connections. More information about the burner itself can be found in Section 2.3.1.1 and in McClearn's thesis[7].

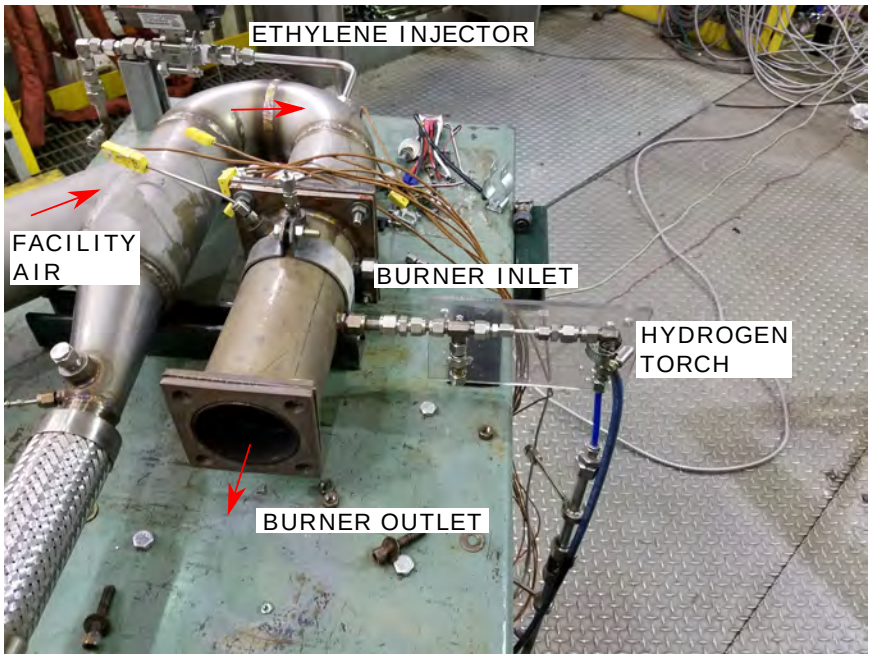

Figure 34. Setup for the Burner Test

The burner was tested independently before the wave rotor was connected in order to confirm that the burner would operate in the desired range of air mass flows and exit temperatures and to gain a general understanding of how the burner operated. The range of air mass flows tested was from 0.015 to 0.030 kg/s. The range of ethylene fuel flow rates was from 0.00075 to 0.00083 kg/s. The fuel and air mass flows into the burner were measured and regulated with sonic nozzles. It was determined during the testing that the combustion was not stable when ethylene was used alone, but

that stable combustion could be obtained by adding a small amount of hydrogen. The amount of hydrogen added corresponded with a bottle pressure of 413685 Pa (60 psi). Therefore, subsequent testing was conducted using both ethylene and hydrogen fuels.

3.6.2 Wave Rotor Integration with the Burner.

Operation of the test rig required a test team of two people, one to run the wave rotor control program and monitor the burner program and one to run the facility control that controlled the burner air flow and the fuel safety valves since the computers that run the programs are physically separated. For this research, the author ran the wave rotor and burner programs while the facility control was operated by an AFRL member who worked at the facility.

After the burner was tested, the wave rotor was integrated in an open loop configuration. Figure 35 shows how the wave rotor was connected to the burner with the major components labeled in red. Like Figure 34, the air flow path is shown with red arrows. The open loop configuration used a valve to back pressure the the AO port instead of connecting the AO port to the burner. The valve can be seen near the top of Figure 35. Both the facility air to run the burner and the air intake to the AI port are on the right in Figure 35.

Initial tests with the coupled test setup revealed some procedural problems with the start-up process. During the first test, the fuel flow of ethylene was set at some level above zero. When the ethylene valve was opened, the sudden increase in fuel caused a sudden increase in the temperature at the EI port. This sudden increase in the temperature caused a sudden increase in the strength of the pressure waves inside the wave rotor. As a result, the motor decoupled from the rotor shaft and the rotor began free-spinning. This condition was quickly noticed and the test was stopped

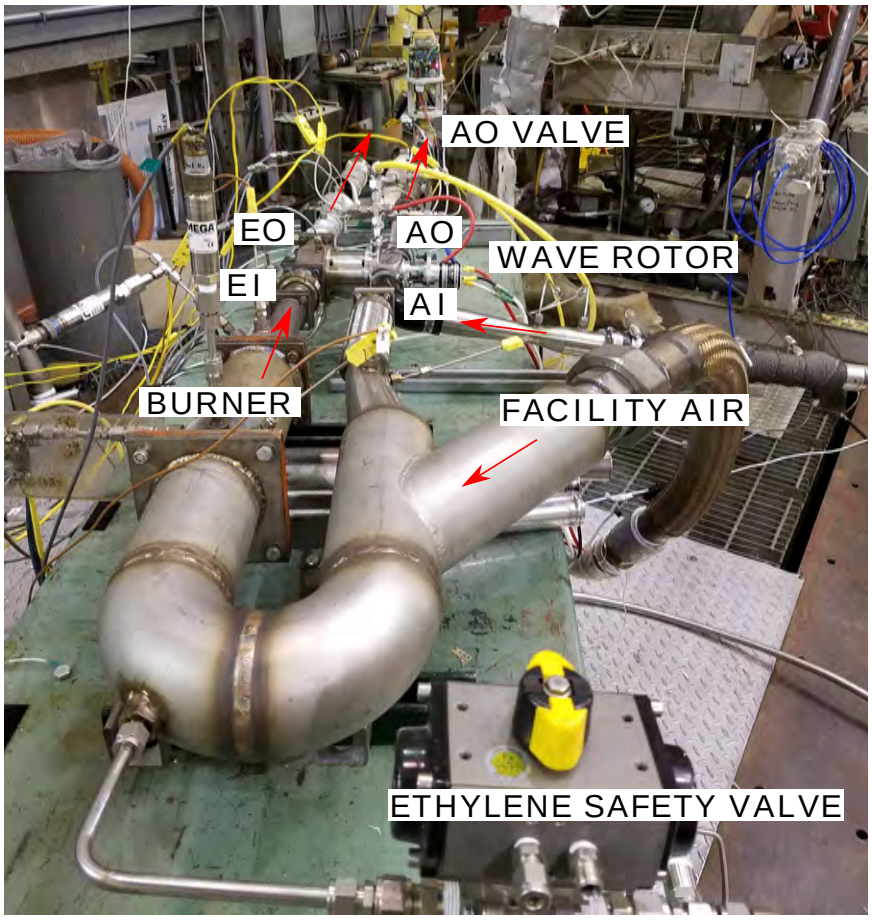

Figure 35. Wave Rotor with Burner Open Loop Configuration

in order to prevent damage to the test rig or the wave rotor. The initial inspection revealed that the Lovejoy coupling that connected the motor to the rotor shaft had separated. The wave rotor was then disassembled and inspected for damage. The electric motor was also inspected for damage and was test spun while decoupled from the rotor shaft. No damage was found on the wave rotor or the motor, so the rig was reassembled so that testing could continue. Further testing procedures confirmed that the ethylene fuel flow was set to zero when the valve was initially opened and the fuel flow rate increased gradually.

3.7 Inclusion of Endwall Pockets

When the PWS tested here was first designed, it was designed without endwall pockets. This design choice was made because the rotor was designed to be driven by an electric motor. This would imply that precise control of the rotor speed should be possible so that the rotor speed would be always matched to the exhaust temperature. This plain endwall design is shown in Figure 36. However, in practice the rotor speed is rarely steady enough to hold the precisely matched rotor speed. The control program showed the rotor speed varying by several hundreds of rpms, when varying by tens of rpms or less would be needed to maintain a matched condition. The variation in rotor speed is likely due to the load on the motor changing faster than the controller can adjust the voltage to the motor to compensate for the changed load. The unsteady rotor speed is why the original endwall design did not perform as expected.

The maximum pressure ratio achieved during the closed loop testing was 1.4, while the expected maximum pressure ratio was about 2.4 from Mataczynski's original design and CFD[6]. Dr. Paxson of NASA was consulted about the mismatch between the expected and actual performance of the wave rotor. In order to answer why the performance was not as expected, Dr. Paxson performed a CFD analysis of the wave rotor as tested, including running the model with and without pockets. When the

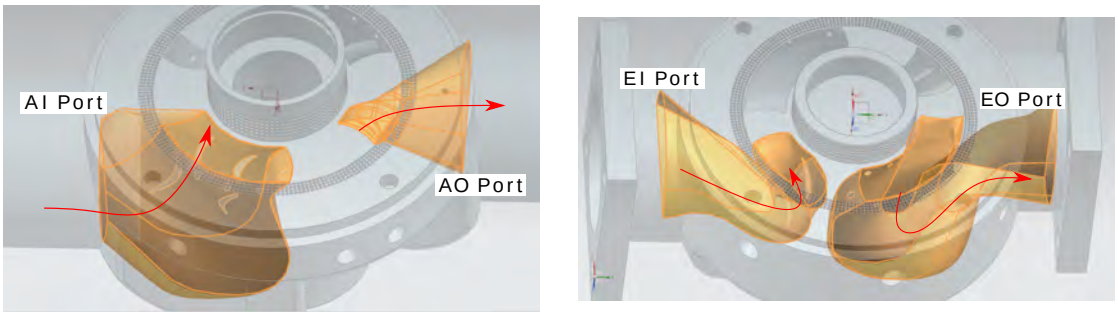

(a) AI and AO Ports of the Plain Endwall **(b) EI and EO Ports of the Plain Endwall**

Figure 36. The Plain Endwalls Designed by Mataczynki[6]

model was run without endwall pockets, the model showed similar results to the experimental results when the code inputs were set to match the test conditions. The difference between the model and experimental data is shown in Table 1. The difference in $P_{t_{AO}}$ between the experiment and model is consistent with the assumption of an 11% loss between the rotor face where the model calculates the pressure and the duct where the properties are measure in the experiment. The difference in the mass flows between the experiment and model was concerning. However, given the suspected problems with the mass flow measurements discussed in Section 3.3, comparing the measured mass flow to the modeled mass flow is not useful in this case.

Table 1. Percent Difference Between CFD Model and Experiment for the Plain Endwall[25]

Parameter	Simulated Value	Error
$P_{t_{AO}}$	167,128.9 Pa	12.52%
$P_{t_{EO}}$	62,949.1 Pa	0.08%
mf_{AO}	0.0285 kg/s	7.61%
mf_{EI}	0.0285 kg/s	-10.41%
mf_{EO}	0.0335 kg/s	-18.43%
T_{AO}	419.6 K	-3.46%
T_{EO}	765.1 K	9.07%
$P_{s_{EO}}$	52,193 Pa	-4.70%

When the simulation was re-run with pockets, it also showed that the wave rotor should perform better at all test conditions when pockets at the same location as the original Comprex® design. Since the pockets help with off-design point operation, they would also help with on-design point operation when the rotor speed is not maintained at exactly the right speed. Based on Dr. Paxson's recommendation, the pockets that were added to the design were matched to the original Comprex® pocket locations. The depth of the pockets was scaled from the Comprex® design based on the width of the rotor channels since the channel width would determine how long any given channel was exposed to a pocket. The decision to base the pocket design

on the Comprex® was made since the PWS tested here was based on the Comprex® cycle. The pocket endwall is shown in Figure 37 compared with the plain endwalls.

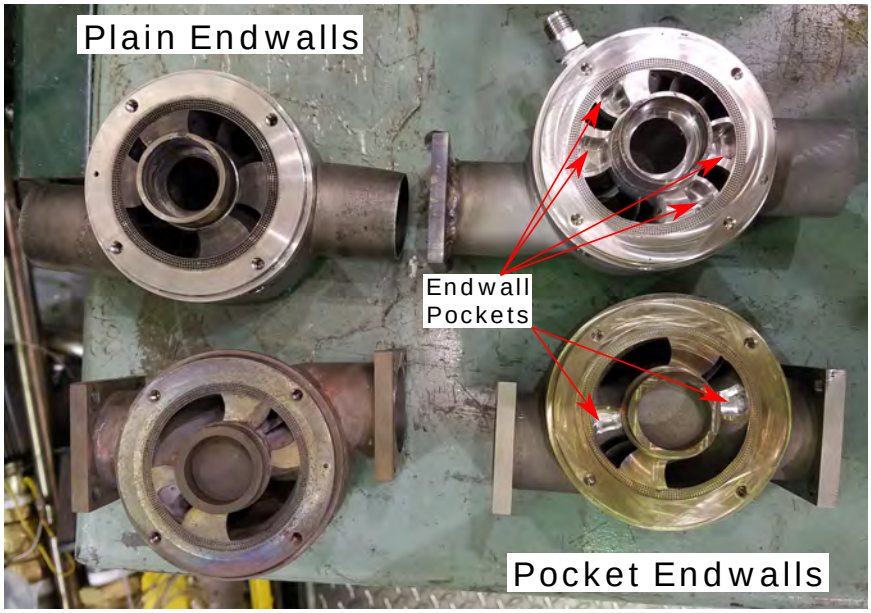

Figure 37. The Plain and Pocket Endwalls

The endwalls with pockets are shown in Figure 38. In order to add the pockets, it was necessary to change the routing of the ports so that the ports and pockets would not intersect. The re-routing of the ports changed the angles so that air and exhaust entered closer to perpendicular to the endwall face. This would result in less air-assist, and therefore less self-spinning of the rotor. This results in a greater load on the electric motor spinning the rotor, however, the increased load is within the limits of the electric motor used in this research. Since the endwall would need to be re-manufactured to change the port routing and include the pockets, a second water channel was also added to cool the bearing near the electric motor. The water channel connections are shown in Figure 39. The second water cooling channel was sized to match the existing channel so that the water flow should split evenly between the channels. The original Comprex® had a channel width of 6.0 mm and a pocket depth of 9.65 mm, which gave a channel width to pocket dept ratio of 0.623. Since

the tested rotor had a channel width of 5.96 mm, this meant that the scaled pocket depth for the new endwall needed to be 9.14 mm.

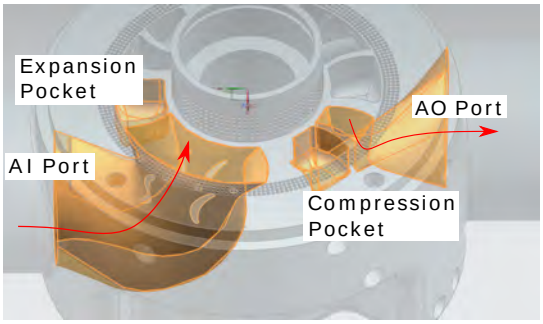

(a) AI and AO Ports of the Endwall with Pockets

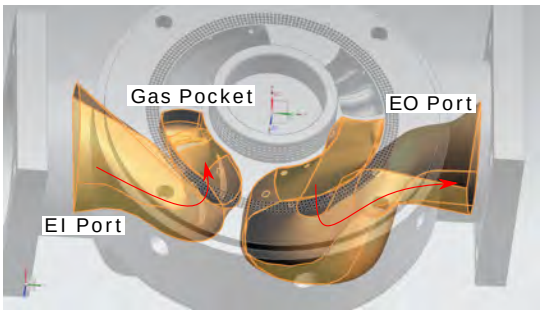

(b) EI and EO Ports of the Endwall with Pockets

Figure 38. The Endwalls with Pockets Included

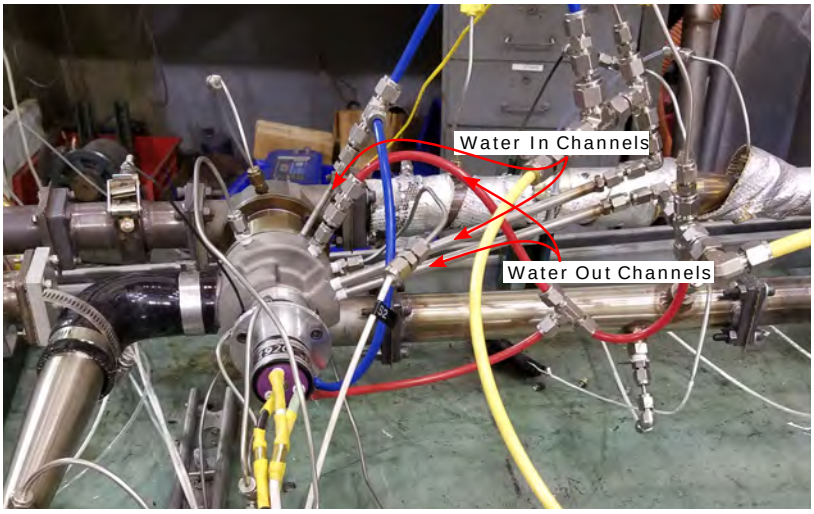

Figure 39. The Water Cooling Channel Connection Points on the Pocket Endwall

3.8 Re-Entry Port Configuration

The re-entry port endwalls were designed by Aerodyn Combustion for testing by Innovative Scientific Solutions at AFRL. The design was based off the work of Mataczynski and used the same size components and shared a common rotor and shaft design with the other two endwall configurations[10]. The hot side endwall was

also the same as the plain endwall design for the re-entry port endwalls. The cold endwall had additional ports just before the AI port and just after the AO port. These ports are shown in Figure 40. These ports were connected so that the high pressure gas still in the rotor channel after the AO port closed could provide some pre-compression of the fresh air in the rotor channels. The location of the ports in the re-entry port design is similar to the location of the pockets in the pocket endwall design. It would be expected that the extra ports would function similarly to the pockets if the ports were plugged instead of connected.

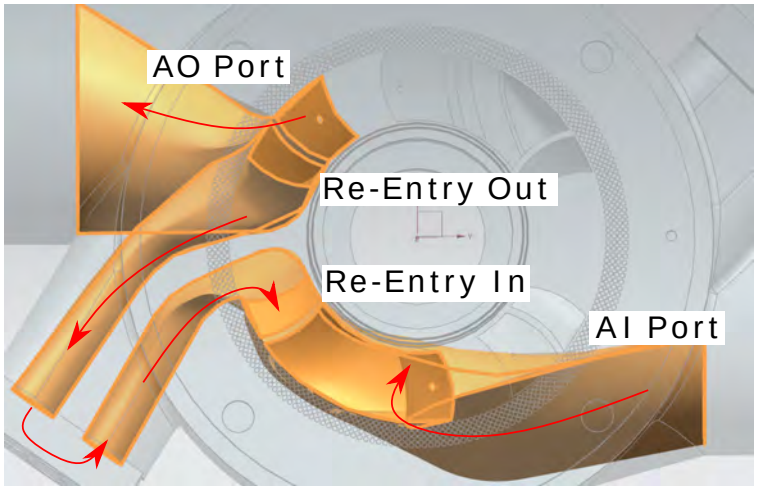

Figure 40. The Cold Endwall with Re-Entry Ports

The cold endwall of the re-entry configuration is shown in Figure 41. This configuration had four ports per cycle in the cold endwall, unlike the plain and pocket configurations that only had two ports per cycle. On the hot endwall, the re-entry configuration had two ports per cycle, which was the same as the other two configurations. Since one cycle only took 180°of rotation to complete, the number of ports per endwall is double the number of ports per cycle for each configuration. This is why there are eight ports shown in Figure 41. Since the wave rotor simulation code used by Dr. Paxson only allowed three ports per cycle for each side, that version of the code could not be used to simulate the re-entry configuration. To develop the

re-entry configuration, Aerodyn Combustion developed an alternate version of Dr. Paxson's code that was able to simulate the re-entry configuration[10], as discussed in Section 2.3.4.

The simulated wave structure for the re-entry endwall configuration is shown in Figure 42 and 43. Figure 42 is colored by temperature and Figure 43 is colored by pressure. The scales in Figures 42 and 42 are normalized, typically by 288 K for the temperature scale and 101325 Pa for the pressure scale, though these values could be changed based on the users needs. When Aerodyn Combustion was designing the re-entry port configuration, it was compared to the pocket configuration since the baseline simulation code Aerodyn Combustion was provided incorporated the endwall pockets. The difference between the re-entry and pocket configurations is shown in Figures 42 and 43. The chart on the left in each figure is the reference pocket configuration and the chart on the right is the re-entry configuration.

By comparing the wave structure charts in Figures 42 and 43, the differences between the cycles can be seen. The differences are quantified in Table 2. In Figure 42, the re-entry configuration on the right shows that the fresh air reaches the opposite endwall sooner. Also, the exhaust gas at the EO port was a lower temperature compared to the pocket configuration. The lower exhaust temperature implies a

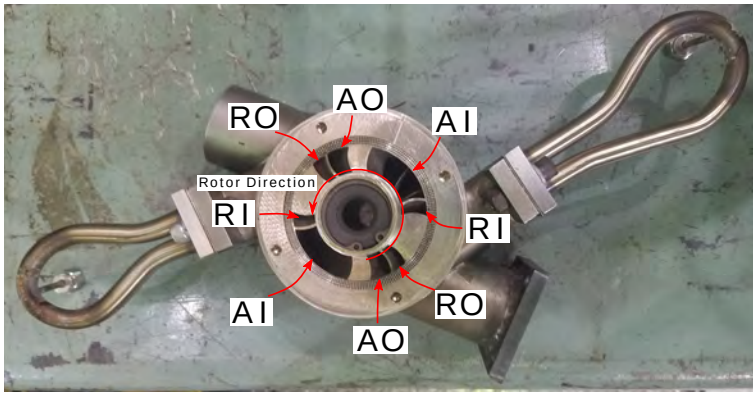

Figure 41. The Re-Entry Cold Endwall With the Ports Labeled

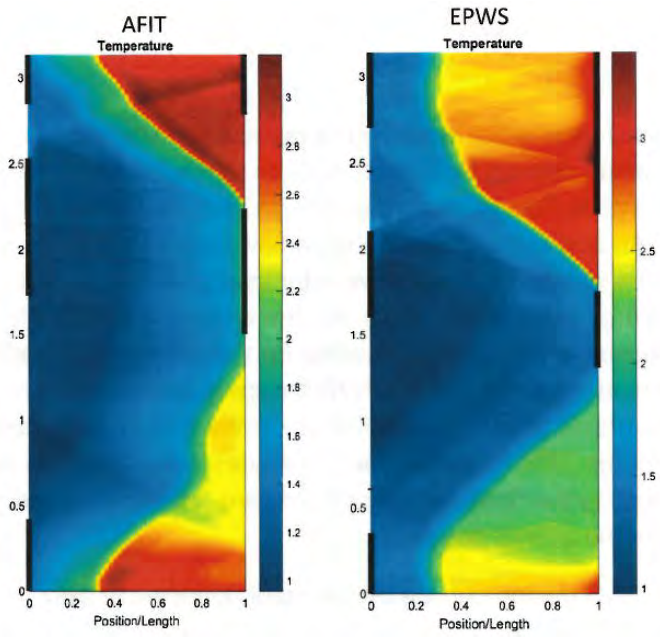

Figure 42. Comparison of the Wave Structure Simulation Results for the Re-Entry and Pocket Configurations Colored by Temperature[10]

stronger expansion wave that pulls the exhaust gas out of the rotor faster. The stronger expansion wave also pulls in more fresh air from the AI port so that both the AI and EO mass flows were about 20% higher in the simulation relative to the reference pocket design. The increased mass flow in the low pressure part of the wave rotor cycle was intended to forcefully scavenge the rotor and prevent EGR. Figure 43 shows the primary shock wave from the EI port has a much stronger reflection at the AO port in the re-entry configuration on the right compared to the pocket configuration on the left. Also, the maximum value of the pressure scale is slightly higher for the re-entry simulation than the pocket simulation. This shows that the re-entry configuration was able to achieve a slightly higher pressure at the AO port in the simulation than the reference pocket configuration. Overall, the simulation indicated that the re-entry configuration was expected to have slightly better performance than the pocket configuration as well as significantly increased mass flow through the low pressure ports.

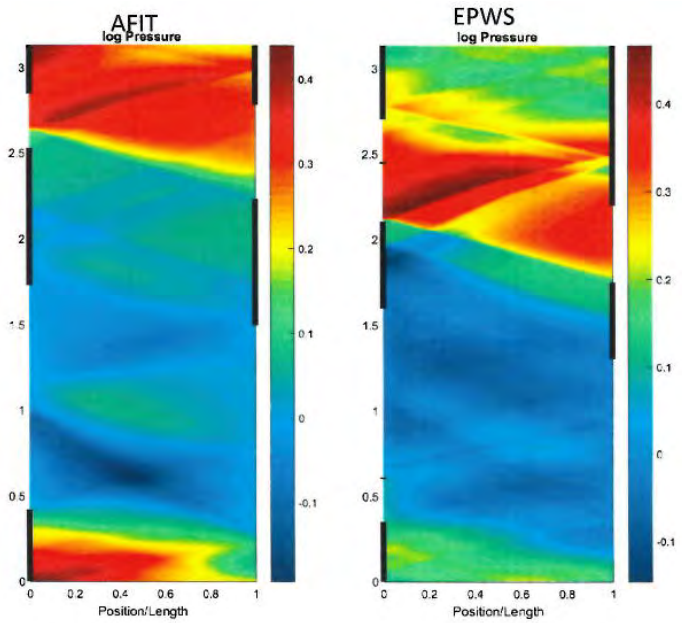

Figure 43. Comparison of the Wave Structure Simulation Results for the Re-Entry and Pocket Configurations Colored by Pressure[10]

Table 2. Difference Between Simulated Pocket Endwall and Re-Entry Endwall[10]

Dimensionless Performance Summary		Pocket Reference	Re-Entry	% Increase
AO/AI Ratio	Pressure	2.36	2.51	6.4%
	Temperature	1.37	1.41	2.9%
Mass Flow, Scaled	AI=EO	0.471	0.568	20.6%
	AO=EO	0.423	0.439	3.8%
EO/AI Ratio	Pressure	0.86	0.91	5.8%
	Temperature	2.96	2.96	0.0%
RI/AI Mass Flow Ratio		n/a	0.44	n/a

3.9 PWS Assembly Process

The components of the PWS are shown in Figure 44. The assembly process started by heating the rotor in an oven set to 490 K for one hour. Heating the rotor enabled it to be pressed onto the shaft. While the rotor was heating, the cold endwall assembly was prepared by first pressing the bearings onto the shaft. Shim rings were then inserted into the cold endwall. The total thickness of the shim rings was 0.508 mm. The shims set the proper spacing between the endwall and the bearings so that the

proper pre-load could be applied to the bearings using the wave washers. The shaft and bearing assembly was then inserted into the cold endwall so that the threaded end of the shaft protruded from the cold endwall on the rotor side enough so that the rotor could be pressed onto the shaft. Next the heated rotor was pressed onto the threaded end of the rotor shaft where the shaft protruded from the cold endwall. The rotor was pressed on until the clearance between the rotor and endwall was less than 0.254 mm. A nut was then tightened onto the threaded end of the rotor shaft to press the rotor onto the shaft to the final endwall clearance of 0.1524 mm as measured with a feeler gauge.

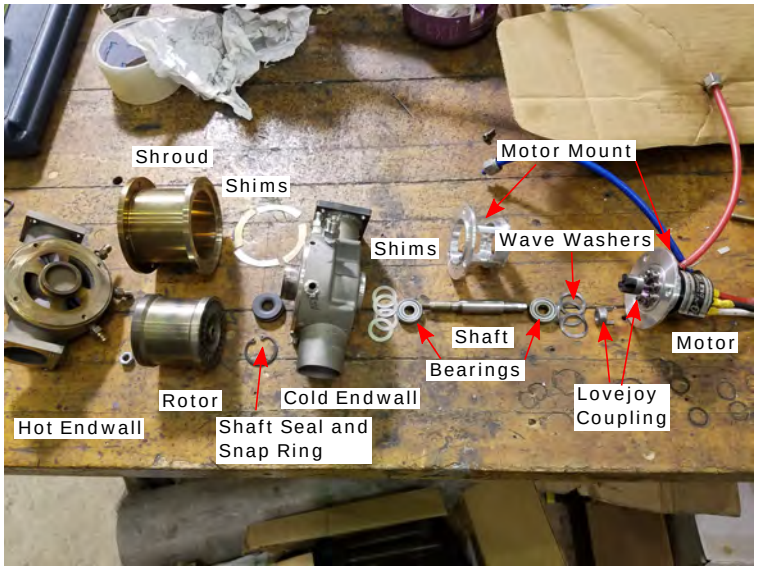

Figure 44. Disassembled PWS

The next step was to attach half of LoveJoy jaw type coupling to the rotor shaft so that the set screw was tightened down on the flat section of the shaft. Next, wave washers were added to apply the needed pre-load to the bearings. The bearings used here had a minimum pre-load of 20 N and a maximum pre-load of about 200 N. For this research, a pre-load of about 50 N was used. Three wave washers were used to achieve a pre-load in this range. The wave washers were placed in the cold endwall against the outer bearing. The upper half of the motor mount was then bolted into

place, securing the wave washers and rotor shaft. The motor was then secured to the lower half of the motor mount and the other half of the LoveJoy coupling was secured to the motor shaft. Washers were used with the bolts securing the motor to the motor mount to ensure that the bolts did not penetrate more than 3 mm into the motor, which could cause damage. The motor was not attached to the rest of the assembly until after the assembly had been mounted in the test rig. Figure 45 shows the cold endwall assembly with and without the shroud for the re-entry port endwall configuration. The other endwall configurations are nearly identical to Figure 45 except for the re-entry port duct.

(a) Without Shroud **(b) With Shroud**

Figure 45. The Re-Entry Cold Endwall Assembly

Once the motor mount was secured to the cold endwall, the shroud was secured to the cold endwall. Shims with a thickness of 0.3048 mm were placed between the cold endwall and shroud to ensure the rotor did not contact the hot endwall during operation. The shroud was then bolted on to the cold endwall. The hot endwall was then mounted in the test rig and the cold endwall and shroud assembly bolted onto the hot endwall. Then assembled PWS is shown mounted in the test rig in Figure 46. The assembly process for each endwall configuration was the same, and each configuration mounted into the test rig in the same manner.

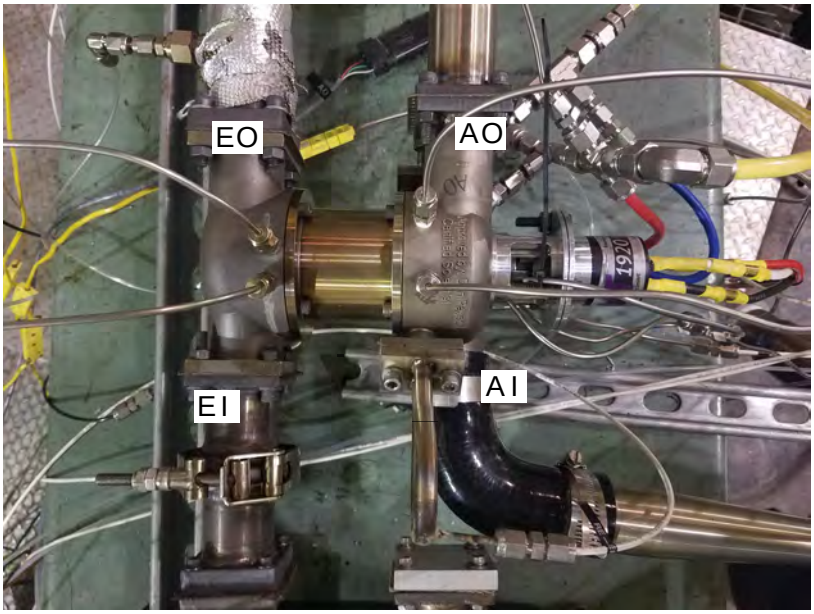

Figure 46. The Re-Entry Configuration Assembled and Mounted in the Test Rig

3.10 Bearing Survivability

During every bearing change or configurations change, the bearing grease had leaked out of the bearing. The lack of bearing lubricant was a main contributor to bearing failure. The bearing grease leaks when the temperature of the bearing increases. The increased temperature lowered the lubricant's viscosity so that it was able to leak past the bearing seals. The increased temperature of the bearing results from high speed operation and EGR increasing the temperature of the cold endwall. Though the speed and temperature never exceeded the limits of the bearing, it was likely the combination of operating near the limits at steady state that caused the lubricant to fail. The limits given by the manufacturer for the bearing speed and temperature were 34,000 rpm and 423 K. Typical rotor speeds were less than 90% of the maximum bearing speed, but were also above 70% of the maximum speed. Operating near the limit speed for extended periods of time is problematic for bearings due to the friction generated heat of the bearing. Also, when EGR occurred in the rotor, the temperature of the cold endwall would increase. Since the bearing

temperature was not measured directly in this research, it is unknown exactly how close the bearing temperatures came to the maximum temperature published by the manufacture. Based on the increase in the temperature in the AO duct when EGR occurred, it is likely that the water cooling system used here was insufficient to prevent overheating the bearings.

Figure 47 shows TAO plotted against AO valve position. For the plain and pocket endwall configurations, as AO valve position increases, TAO also increases until an AO valve position of 0.6, where the temperature starts to level off. The re-entry port endwall also shows this trend, but with much smaller magnitude. This increased temperature in the AO port is indicative of EGR. Therefore, in order to help prevent bearing failure, the AO valve position should be kept below 0.6 to prevent EGR from heating the cold endwall which could lead to premature bearing failure.

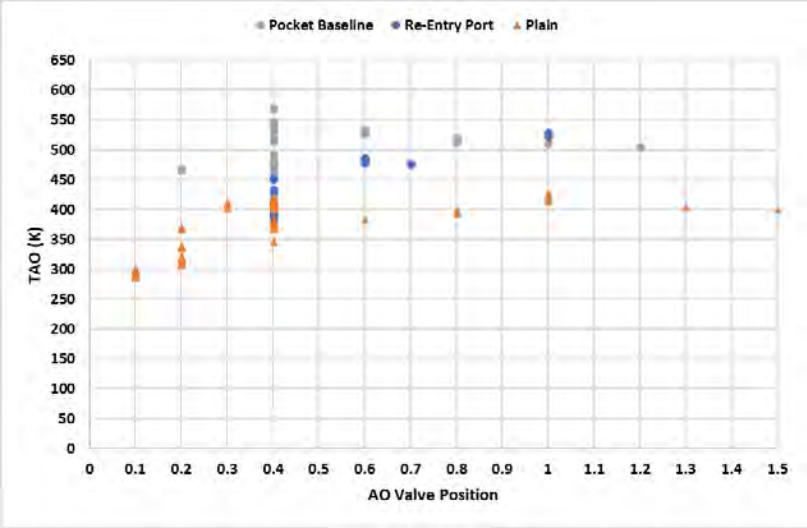

Figure 47. TAO vs AO Valve Position for Each Endwall Configuration

When looking at AO valve position of 0.4 in Figure 47, there is a large group of data points with high AO temperatures. This is due to the change in the exhaust temperature between the different data points. As discussed near the end of Section 4.2, increased exhaust temperatures can cause an increase in the AO temperature.

This is what is seen in vertical grouping of points at the AO valve position of 0.4. The re-entry port endwall also seems much less sensitive to changes in the AO valve position than the other two configurations and slightly more sensitive to changes in the exhaust temperature. As the AO valve position drops to 0.2, the re-entry port does seem to follow the same pattern at the other two configurations, but at a higher AO temperature than either the pocket or plain endwalls.

IV. Results and Discussion

The tests conducted in the D-Bay facility were all conducted with the procedures outlined in Appendix A. The tests were separated into four sets in order to meet the research objectives outlines in Section 1.2. The research objectives can be summarized to comparing the performance of the three different endwall configurations. The performance was measured by determining the compression efficiency, the pressure ratio, and the AO mass flow for each configuration. The first set of PWS tests refined the procedures and established the baseline performance of the plain endwall. These are discussed in Section 4.1 and Section 4.2. Next the baseline performance of pocket endwall configuration is discussed in Section 4.3 and the with-pocket performance of the pocket endwall in Section 4.4. The results of the re-entry endwall configuration are discussed in Section 4.5, and the performance of each configuration is compared in Section 4.6.

4.1 Initial Testing

Initial testing of the PWS was conducted with the plain endwalls in an open loop configuration. Testing in this configuration allowed for some comparison to previously collected open loop test cart data collected by Mataczynski[17] and to iron out any procedural issues with the testing before evaluating the modified endwalls. The open loop configuration used for the initial tests was the configuration described in Section 3.6. Two people were required for each test run according to AFRL safety requirements. The test team consisted of the author and one other AFRL member, usually Mr. Rice. This configuration had the mass flow through the burner set by the test team using the test facility's air supply. For the first test, this was set to 0.0302 kg/s. The mass flow was metered using the 0.201 inch diameter sonic nozzle.

The flows of ethylene and hydrogen were also metered with sonic nozzles. The mass flow through the burner fed the EI port while the AI and EO ports were left open to ambient conditions in the test facility. The AO port was backpressured by the gate valve which vented to ambient. The mass flow of the hydrogen was set before the test started by setting a feed pressure from the hydrogen bottle to the upstream side of the sonic nozzle. For the first test, this hydrogen pressure was set to 413,600 Pa. The ethylene flow was controlled manually from the control room by turning a knob to adjust the pressure on a dome loader. The dome loader controlled the pressure in the ethylene line proportional to the pressure selected in the control room. The range of ethylene pressure used for the initial test was 689,500 to 965,300 Pa.

The first step to run was to turn on the air flow through the EI port and turn on the electric motor that spun the rotor. The air flow and motor speed were increased gradually so that the rotor reached and operating speed of 26,000 rpm in three to five seconds. Next, the spark on the hydrogen torch was turned on so that it sparked twice per second. Once the air flow, rotor speed, and spark were at the correct settings, the 5.57e-5 kg/s flow of hydrogen was started by opening the LAST CHANCE 2 valve. Initial starting parameters for the air flow, rotor speed, and spark timing were 0.02268 kg/s, 26,000 rpm, and actively sparking at a frequency of 2 Hz. The hydrogen lit, and a temperature rise of about 100 K was confirmed. Next the flow of ethylene fuel was started by opening the LAST CHANCE 1 valve and the ball valve in the control room, then adjusting the control knob in the control room. The ethylene flow was adjusted until a steady EI temperature of about 890 K was reached. This temperature was typically reached with about 499,181 Pa, which corresponded to an ethylene flow rate of 6.43e-5 kg/s. In order to maintain flame stability, the flow of hydrogen was maintained for the entire test run. The temperature and speed sweeps were conducted by setting at EI temperature and then increasing the rotor speed until

the top end of the speed range was reached. The EI temperature was then adjusted to a new value before the rotor speed swept back down to the bottom of the test range. Battery life limited testing to about 30 to 45 minutes per test run. The test would then be paused and the batteries changed or charged before testing would resume.

The initial test successfully spun the rotor to 28,000 rpm with 0.0302 kg/s mass flow though the burner without bearing failure or encountering rotodynamic modes. However, a procedural issue was discovered with how the burner was started. On this first test, the flow of ethylene was set higher than anticipated on the hand control knob so that as soon as the ethylene valve opened, fuel flow suddenly increased. This caused a sudden increase in the temperature at the EI port. The sudden temperature rise subsequently caused a change to the wave structure in the rotor. The end result was that the electric motor decoupled from the rotor so that the rotor began free-spinning and the motor speed spiking since there was no longer a load on the electric motor. At this point the test was stopped. The test rig was then disassembled and inspected for damage. It was found that the motor had disconnected from the rotor shaft, but otherwise there was no damage found. The test rig was then reassembled and test runs continued. Following this test, the procedures were updated to include confirming that the ethylene hand control knob was closed before opening the LAST CHANCE 1 and ethylene ball valves. Also, later analysis revealed that 0.0302 kg/s of air flow was above the design flow for the rotor and also above the flow rate through the engine at maximum engine speed. Therefore, subsequent tests used a reduced flow rate of 0.0227 kg/s of air flow that was within the range for both the engine and wave rotor.

4.2 Plain Endwall Tests

The first test run collected data used the plain endwalls. These were the original endwall designed by Mataczynski[6] and discussed at the end of Section 2.3.1. A CAD rendering of the endwall can be seen in Figure 36. The range of data collected was for a EI mass flow of 0.0265 kg/s and a AO valve position of 4.0, which corresponds to the valve being 40% open. The AO valve was controlled from wave rotor control program by adjusting the input value in the AO Bleed field in the program. This signaled the control board on the valve to open or close the valve. The 0.0265 kg/s of EI mass flow corresponds to a diesel engine speed of about 3600 rpm, which is the upper speed limit of the engine. The rotor speed ranged from 25,000 rpm to 31,000 rpm. The exhaust temperature at EI ranged from 890 K to 1090 K.

The next test runs were an additional success in that the test continued until the batteries ran out of power instead of stopping due to equipment failure. The first test run gathered 9 data points before the battery died. The battery was replaced and the second test run began where the first test ended. The second test run also continued until the battery died and collected 18 more data points. Upon inspection of the test rig, it was determined that the bearings were still functional, and that other components were also in working order.

The mass flow through the EI port for this test was set at 0.0277 kg/s. The mass flow was decreased further from previous test since flow had been observed flowing out the AI port as well as the EO and AO ports. The decision was made to decrease the mass flow in order to have a better chance of setting up the proper wave structure in the rotor for the range of EI temperatures and rotor speed that were tested. A mass flow of 0.0277 kg/s corresponds to about 3000 rpm for the diesel engine the PWS was sized for, which is about the middle of the speed range for the engine. For this test, the EI temperature was set at 810 K and the AO gate valve was incrementally

closed until the pressure in the AO port was greater than the pressure in the EI port, which occurred at an AO valve position of 0.4, or 4% open. At this point the final set of batteries died and the test run was stopped before the planned temperature and speed sweeps could be ran. The rotor speed and EI temperature sweeps were then conducted in the next test run with the AO valve position at 0.4.

Figure 48 shows the compression efficiency plotted against the rotor speed for the plain endwalls. The data in Figure 48 was binned by valve position. The chart shows that the efficiency increases with decreased valve position independent of the rotor speed. It can also be seen that there was a slight increase in the efficiency as the rotor speed increased for a given AO valve position. This is most noticeable in the group of data where valve position was 0.4.

Figure 48. Compressor Efficiency vs Rotor Speed Binned by AO Valve Position

The efficiency can also be plotted against the AO valve position, as seen in Figure 49. The rotor speed and exhaust temperature vary for the data points in Figure 49. However, the change in efficiency is fairly constant up to an AO valve position of 0.4

where a collection of data points with a small spread in efficiency is seen. This shows that the AO valve position dominates the compression efficiency compared to the rotor speed and exhaust temperature. Since AO valve position has the largest effect on the performance of the PWS, it was chosen as the primary x-axis for plotting the performance.

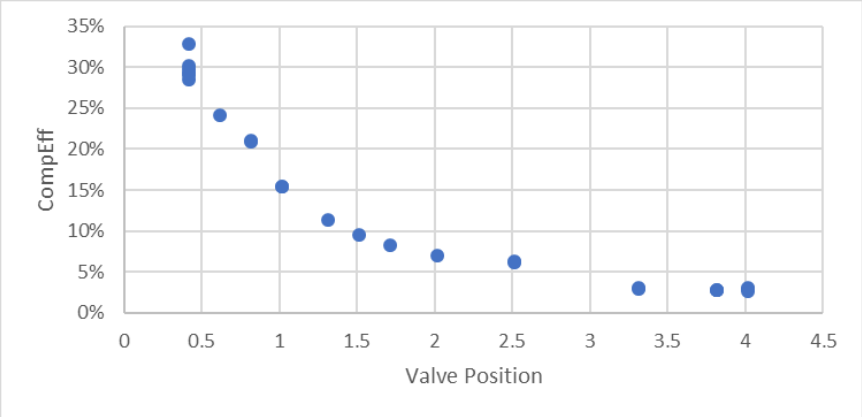

Figure 49. Compression Efficiency Plotted Against AO Valve Position

The compression efficiency increased at low AO valve positions due to the increase in backpressure on the AO port caused by the closing of the AO valve. Since the compression efficiency is directly proportional to the APR, as seen in Equation 5, increasing the pressure in the AO port will cause an increase in the compression efficiency. It is the relative pressures in the ports that allow the wave structure inside the wave rotor to be set up. In this case, that means there must be some back pressure on the AO port in order to prevent the generation of an expansion wave at the AO port opening, which would break the wave structure in the rotor. Instead, there need to be sufficient pressure in the AO port so that the flow into the port from the rotor is dominated by the effects from the primary and secondary compression waves. This issue is self-solving in a closed loop configuration since the required back pressure is provided by the wave rotor from the EI port through the engine or burner. However, in an open loop configuration such as what was tested here, the AO valve is open to

ambient conditions. Therefore, the AO valve is needed to provide the required back pressure. The trade off is that closing the AO valve to provide the needed pressure also restricts the mass flow out the AO port. This means that balancing the mass flows between the ports are much more difficult to balance. In a closed loop configuration, this is again a minimal issue since the AO port feeds the EI port through the engine and the only mass flow balancing that is required is to avoid EGR. However, in the open loop configuration where the mass flow is restricted through the AO port, the mass flows are typically unbalanced, which can degrade the wave structure in the rotor and subsequently impact the overall performance of the PWS. Comparisons between open loop and closed loop configurations are therefore less useful since the mass flow balances are significantly different between the configurations.

The results of the plain endwall baseline testing is shown in Figure 50. The efficiency and mass flow are plotted on the secondary axis for each chart in Figure 50 with the efficiency expressed as a decimal and the mass flow value multiplied by 10 so that it was easily observed on the same scale as the efficiency. Each subfigure shows the APR, compression efficiency, and mass flow through the AO port for a constant rotor speed. When the data is plotted this way, some trends in the plotted values can be seen. In Figure 50a, the efficiency and pressure ratio both started at very low values when the AO valve was open, but increased as the valve reached a position of one, or 10% open. At this point the pressure ratio and efficiency both increased to a pressure ratio of just over two and an efficiency of about 0.6 at a valve position of 0.1, or 1% open. These values made sense because as the AO valve is closed, the back pressure to the AO port is increased, so the pressure in the AO port increased, which in turn increased the pressure ratio. The efficiency also increased since there was meaningful compression as the pressure in the AO port rose.

The AO mass flow in Figure 50a also shows an interesting trend. At valve positions

above 10% open, the mass flow is mostly constant and is somewhat high. This is expected since the open AO valve is allowing a lot of mass flow through the AO port. As the AO valve position reaches 10% or below, the mass flow drops off as expected since the closing valve is restricting the flow. However, as the AO valve position is reduced, there is much more scatter in the AO mass flow data, with a possible increase in the mass flow at very low AO valve position values. The slight increase can be seen more clearly in Figures 50c - 50e which only show valve positions between 0 and 0.5. At first this seems unusual, but upon further examination, it is determined that at the lower AO valve positions, there is sufficient back pressure in the AO port to properly set up the wave structure inside the wave rotor. The properly set up wave structure then is able to force more mass flow out the AO port compared to a improperly set up wave structure. The properly set up wave structure does not increase the mass flow to the same level as with the AO valve wide open, but it is above the expected value for low AO valve positions.

For piston engines, the exhaust pressure is always slightly higher than the intake pressure. This is due to the nature of the engine as the piston pulls air in and pushes air out. However, wave rotors work better when the pressure at the AO port going to the engine is higher than the pressure at the EI port coming from the engine. The pressure ratio P_{tEI}/P_{tAO} is referred to as the Engine Pressure Ratio (EPR). It is desirable that the EPR be greater than one for integrating the wave rotor with a piston engine. In Figure 51, the ratio of EI total pressure to AO total pressure drops below one at an AO valve position of 0.6. At this valve position the efficiency for the plain endwalls is only about 20% and the APR is about 1.6. This means that the PWS is providing some compression to the AO port, but it is not the best that the wave rotor can do and it is not compressed very efficiently. The overall goal of adding pockets or a re-entry port to the endwall is to increase the efficiency and APR when

(a) Rotor Speed = 26,000 rpm

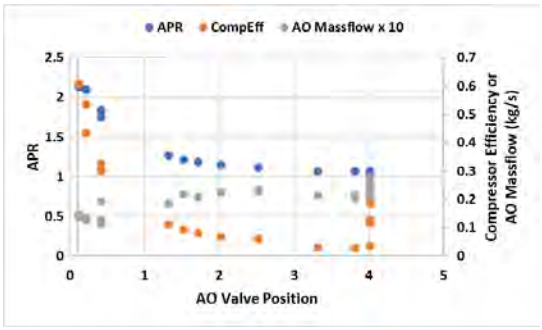

(b) Rotor Speed = 27,000 rpm

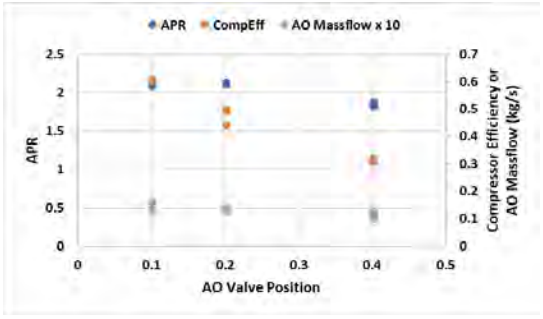

(c) Rotor Speed = 28,000 rpm

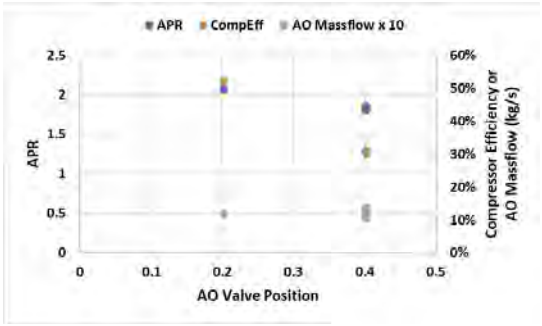

(d) Rotor Speed = 29,000 rpm

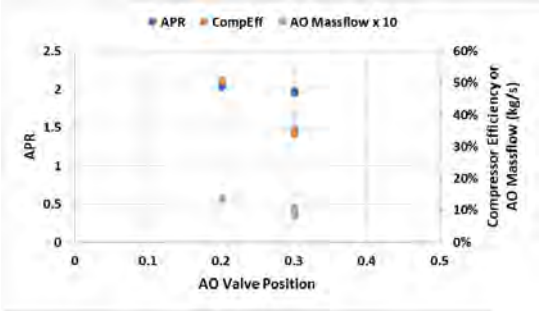

(e) Rotor Speed = 30,000 rpm

Figure 50. APR, Efficiency, and AO Mass Flow for Various Rotor Speeds

the EI total pressure to AO total pressure ratio reaches one.

The point where the EPR is equal to one is better visualized by plotting vertical lines on the performance plots at EPR=0.9 and EPR=1.0, as shown in Figure 52a. Only the points to the right of the EPR=1 line are compatible with a real engine, but the points to the left of the EPR=0.9 line are where the PWS has the best performance. Integration of a PWS with a real engine requires a compromise on the PWS cycle performance in order to allow it to integrate with the engine.

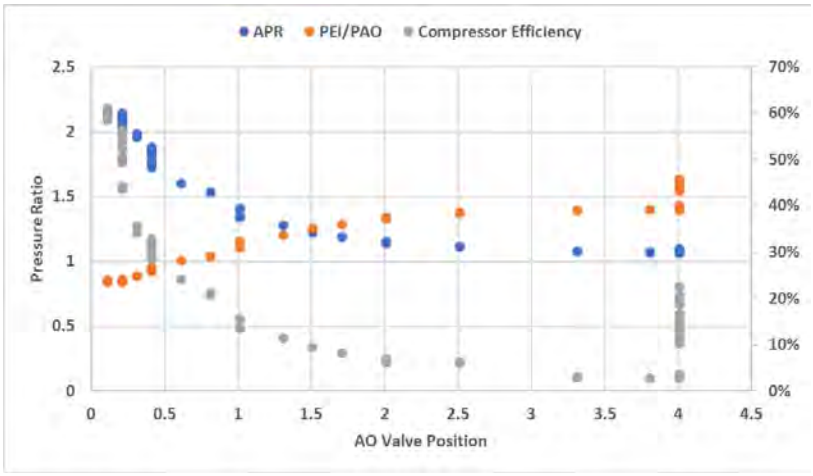

Figure 51. Air Pressure Ratio, EI Total Pressure over AO Total Pressure, and Compressor Efficiency vs. AO Valve Position

Also in Figure 52a, the data points are colored by rotor speed, with low speed in blue and high speed in red. This shows that the rotor speed by itself does not have a large effect on the performance of the PWS. Figure 52b is formatted the same way as Figure 52a and shows that the rotor speed by itself also does not have a significant effect on compression efficiency. Lines of EPR=0.9 and EPR=1 are shown on Figures 52 and 53 to show a possible range of PWS performance that is a compromise between EPRs that are compatible with a real engine and EPRs where the PWS performs well. This range is between the two lines, where the EPR is between 0.9 and 1.0.

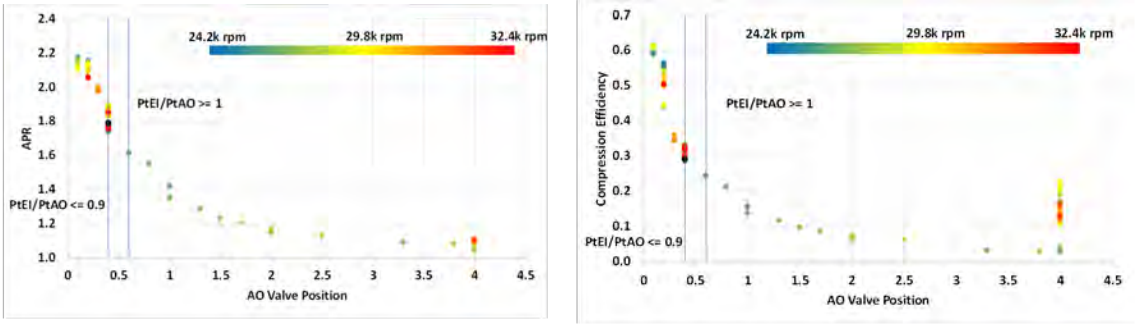

(a) APR **(b) Compression Efficiency**

Figure 52. Plain Endwall Performance Colored by Rotor Speed

Figure 53 shows the same data as Figure 52, but with the data points colored by

TEI. The charts show that TEI has an impact on the performance of the wave rotor. For both the compression efficiency and the APR, increased exhaust temperatures show an increase in performance for AO valve positions of less than about 1, or 10% open. For the series of data points at an AO valve position of 4, increasing TEI leads to a decrease in wave rotor efficiency with minimal effect on the APR. The decrease in efficiency is due to an increase in the AO temperature, which is shown in Figure 54.

As mentioned in Section 2.4, the efficiency calculation is dependent on the temperature in the AO port, shown as T_{AO} in Equation 6. The temperature in the AO port in turn is dependent on the amount of compression of the fresh air and the temperature of the exhaust gas if a significant amount of EGR is present. Figure 54 shows the compression efficiency of the PWS colored by AO temperature. As expected, a decrease in efficiency is seen as AO temperature increases. AO temperature also has an effect on the expected useful life of the bearings. This effect is discussed in more detail in Section 3.10. To achieve accurate efficiency reading and extend the life of the bearings, it is desirable to keep the AO temperature low. In this case, a "low" AO temperature means it is not influenced by EGR, though the actual temperature may be 100 K or more above ambient conditions.

The temperature in the AO port was primarily influenced by the AO valve position

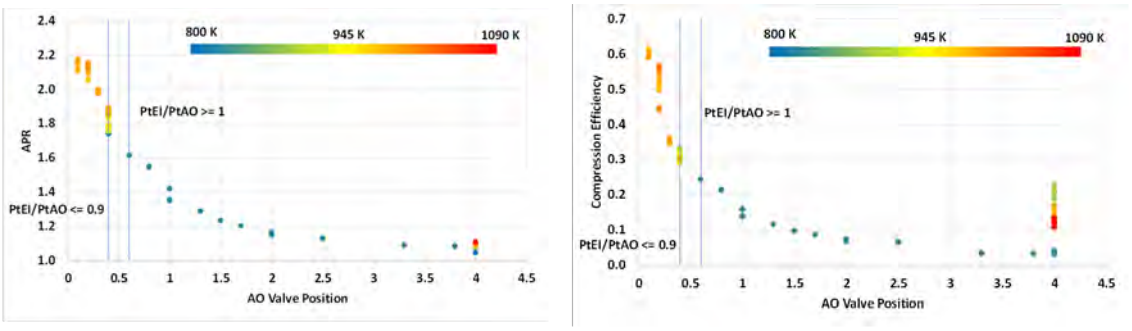

(a) APR **(b) Compression Efficiency**

Figure 53. Plain Endwall Performance Colored by Exhaust Temperature TEI

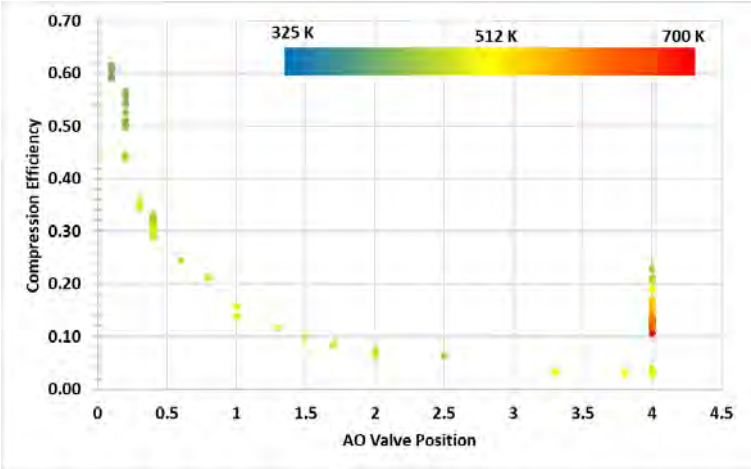

Figure 54. Compression Efficiency vs AO Valve Position, Colored by TAO

and the temperature of the exhaust if EGR was present. The presence of EGR was also dependent on the AO valve position. Figure 55 shows the AO temperature plotted against the AO valve position with data points colored by TEI. For a constant AO valve position of 4, as the exhaust temperature increased, the temperature in the AO port also increased. This was due to the significant amount of EGR present when the AO valve was this open. As the AO valve closed, the influence of TEI through EGR decreased so that at an AO valve positions of less than 0.6, the AO temperature remained relatively low even though TEI increased. This indicates that there was much less EGR at these test conditions, and so the temperature in the AO port reflected only the temperature of the compressed fresh air, resulting in a more accurate efficiency calculation. EGR influences the efficiency though the temperature in the AO port, T_{AO}. By breaking out T_{AO} in Equation 5, it is seen how the EGR can impact the efficiency. This is shown in Equation 15 where $T_{AO_{EGR}}$ is the portion of the temperature in the AO port that is due to EGR and $T_{AO_{Compression}}$ is the portion that is due to compression of the fresh air. The effect is to increase the temperature in the AO port, which lowers the calculated compression efficiency. In reality, it is not a pure addition between $T_{AO_{Compression}}$ and $T_{AO_{EGR}}$. Instead, it is a mass weighted

average between the two temperatures and depends on the relative mass flow of the compressed fresh air and the EGR as discussed in Section 2.4.2.

$$\eta_c = \frac{\left(\frac{P_{AO}}{P_{AI}}\right)^{(\gamma-1)/\gamma} - 1}{\frac{\left(T_{AO_{EGR}} + T_{AO_{Compression}}\right)}{T_{AI}} - 1} \tag{15}$$

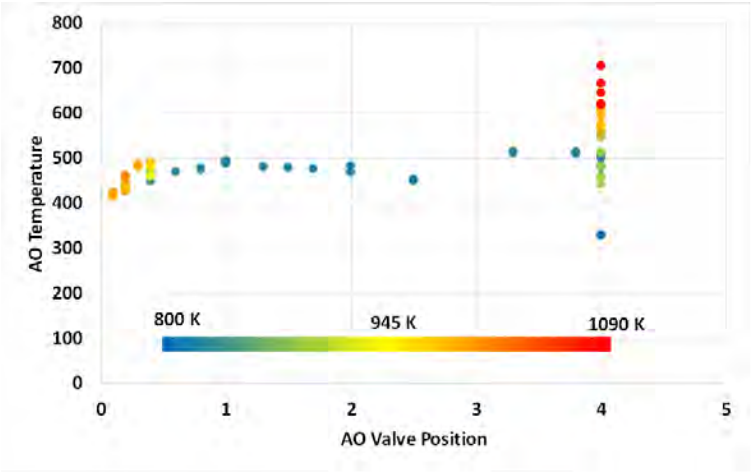

Figure 55. AO Temperature vs AO Valve Position, Colored by TEI

4.3 Pocket Endwall Baseline Results

Due to the change in the port angles caused be the addition of pockets to the endwalls as discussed in Section 3.7, the endwalls with pockets was tested before the pockets were added in order to establish a baseline performance and determine whether the changing of the port angles had any effect on the PWS performance. Figure 56 shows the APR, efficiency, and AO mass flow for the plain endwalls and the pocket endwall baselines for a rotor speed of 26,000 rpm. The plot of APR vs AO valve position in Figure 56a shows that there was no difference between the APR of the plain endwall and the APR of the baseline pocket endwalls. Similarly, Figure 56b shows that the efficiencies of the different endwall configurations are nearly the

same.

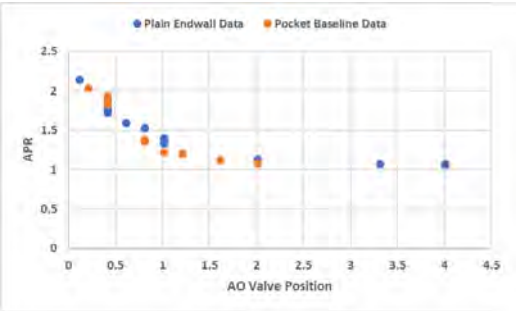

(a) APR

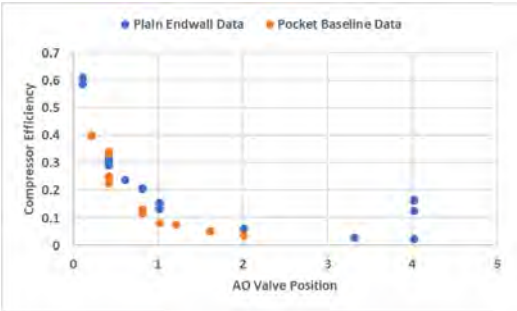

(b) Compressor Efficiency

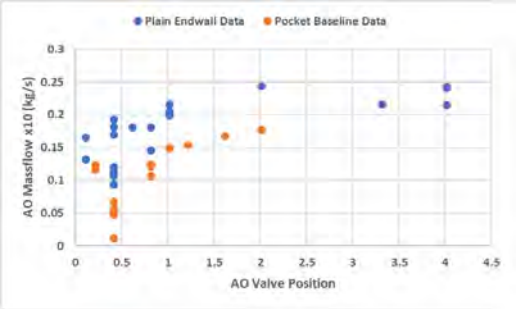

(c) AO Mass Flow (kg/s)

Figure 56. Plain Endwall and Pocket Endwall Baseline Data for Rotor Speed = 26,000 rpm

Unlike the compression efficiency and APR, Figure 56c shows a difference in the magnitude of the mass flow out the AO port, though the data follows the same trend. The test setup between the plain endwall and the pocket baseline tests were the same, so a possible cause of the difference in AO mass flow was the change in the port angles. It was also possible that the difference in mass flow was caused by an unknown change to the amount of leakage from the rotor. Leakage in the wave rotor occurred due to the gap between the rotor and the endwall, and small differences in the amount of clearance between the rotor and endwall in different configurations can change how much leakage occurs, which then changes the mass flow through each port. The charts in Figure 57 show the same trends as those in Figure 56 but for a rotor speed of 27,000 rpm. Since the trends are the same between the two figures, the rotor speed does not have an effect on the difference in performance between the

two endwall configurations.

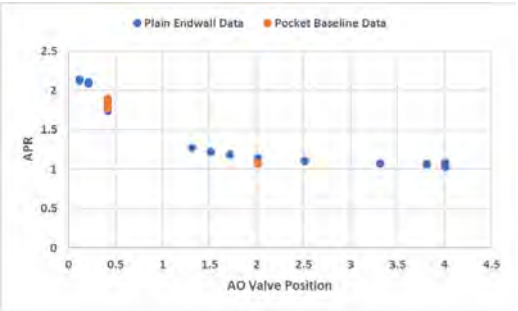

(a) APR

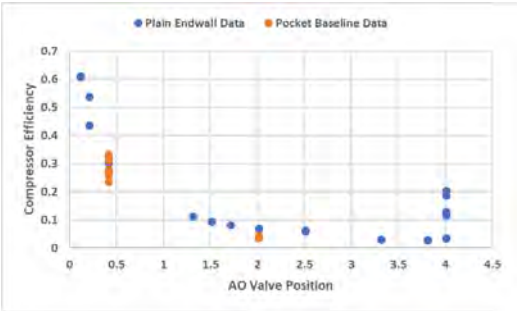

(b) Compressor Efficiency

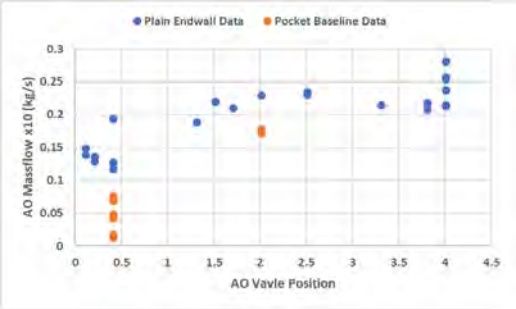

(c) AO Mass Flow (kg/s)

Figure 57. Plain Endwall and Pocket Endwall Baseline Data for Rotor Speed = 27,000 rpm

4.4 Pocket Endwall Test Results

After the baseline test, the pocket endwalls were sent back to the shop to have the pockets machined out of the endwall face. Only one test run of the pocket endwalls was completed. The parameters for this test run were an AO valve position between 1 and 0.4, rotor speed ranging from 23,500 rpm to 28,000 rpm, and exhaust temperature from 800 K to 1000 K. Figure 58 shows the APR and compression efficiency for the pocket configuration with the data points colored by rotor speed, while Figure 59 shows the same data colored by TEI. Again decreasing the AO valve position increased both the APR and the compression efficiency. Again, the rotor speed by itself does not have a significant effect on the performance of the wave rotor. When the data points are colored by exhaust temperature as shown in Figure 59, both the

compression efficiency and APR increase as TEI increases. This trend matches the trend of the other endwall configurations.

Figure 58 and 59 also have a vertical line depicting where the pressure ratio across the engine equals one. Data points to the right of this line have an EPR of greater than one and are compatible with the engine, while points to the left of the line have an EPR of less than one and are not compatible with the engine. The EPR equaled one at an AO valve position of 0.6, which was the same as the plain endwall. There was one data point that was an exception. The test point of 23,585 rpm rotor speed and 994 K had an EPR of 1.01 at an AO valve position of 0.4 and so is to the left of the vertical line. As before, the PWS only achieved marginal performance with a maximum APR of about 1.6 and a maximum compression efficiency of about 35% at an EPR of one. The pocket endwall did not improve on the APR compared to the plain endwall APR of 1.6. However, the compression efficiency was improved by about 9%.

A sample of the pocket endwall data is shown in Figure 60. This sample is for a constant exhaust temperature of 811 K and covers a range of rotor speeds from about 24,000 rpm to 28,000 rpm and a range of AO valve positions from 0.4 to 1.0. The pocket endwall data sample is compared in Figure 60 to the plain endwall data that

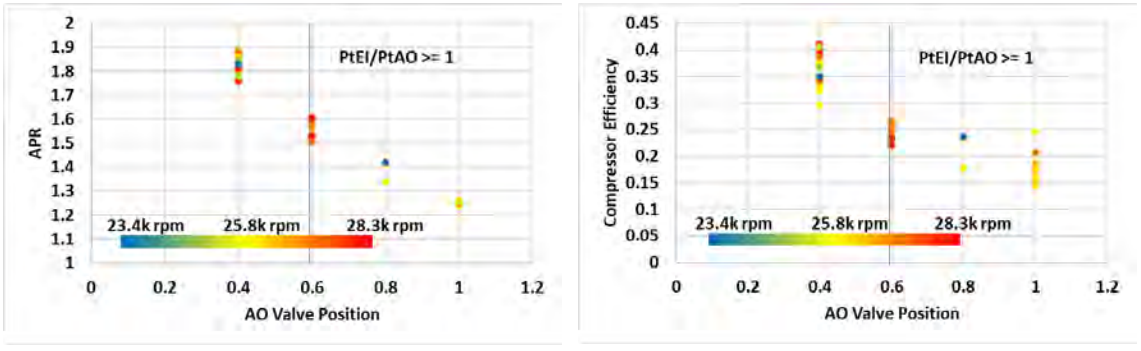

(a) APR **(b) Compression Efficiency**

Figure 58. Pocket Endwall Performance Colored by Rotor Speed

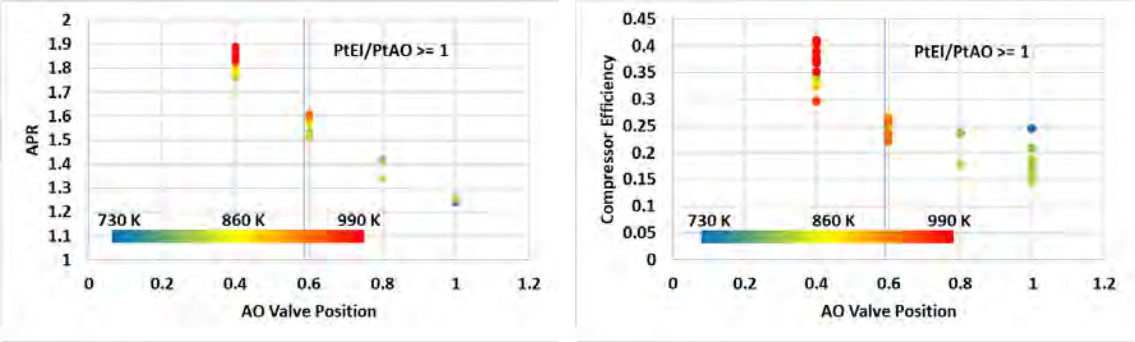

(a) APR **(b) Compression Efficiency**

Figure 59. Pocket Endwall Performance Colored by TEI

meets the same criteria. The data in Figure 60 is colored by rotor speed. The chart shows that the pocket endwall has slightly better efficiency than the plain endwall for these test conditions, which include both on and off design point test conditions.

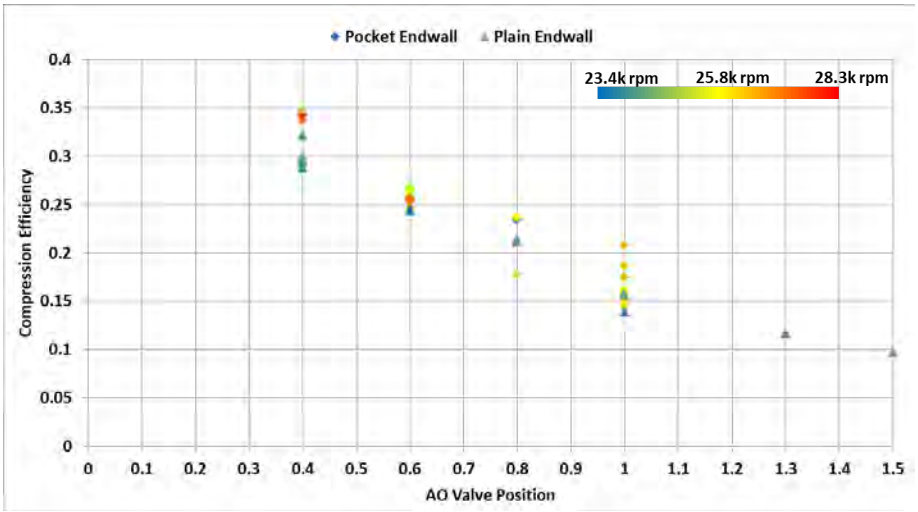

Figure 60. Pocket Endwall Performance Compared to the Plain Endwall for 811 K

Figure 61 shows a different sample of the pocket and plain endwall data. In this case, the data is limited to points with a rotor speed of 26,000 rpm. The pocket endwall data in this sample had a range of AO valve positions from 1.0 to 0.4 and a range of exhaust temperatures from 990 K to 800 K. The plain endwall data sample covered a range of AO valve position from 1.0 to 0.1 and exhaust temperatures from 990 K to 730 K. For this data sample, the pocket endwall again had slightly higher

efficiencies that the plain endwall for the same test conditions, though the difference in performance was smaller for the data in Figure 61 than the data in Figure 60.

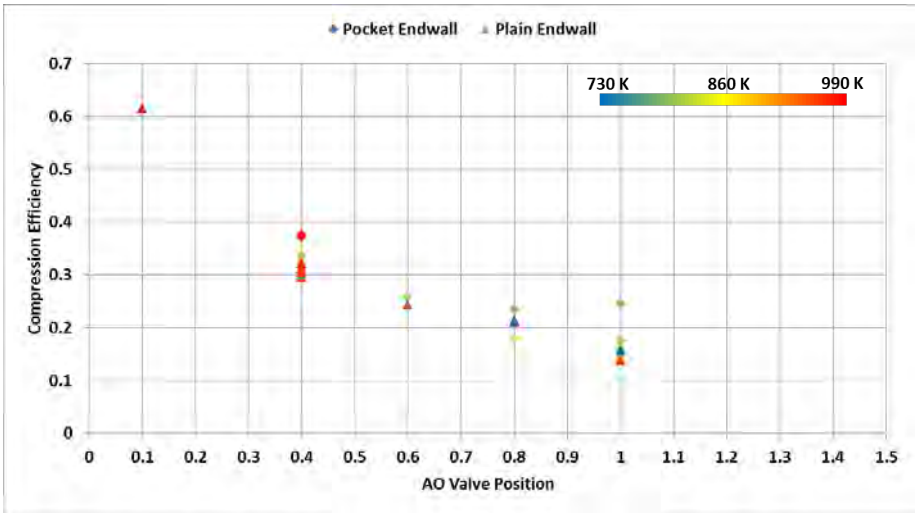

Figure 61. Pocket Endwall Performance Compared to the Plain Endwall for 26,000 rpm

4.5 Re-Entry Port Endwall Test Results

The data for the re-entry port endwall configuration was analyzed in the same way as the plain endwall configuration. The data points were collected using the same test matrix, shown in Appendix **??**, as the plain endwall and so cover the same range of exhaust temperature, rotor speed, and AO valve position ranges as the plain endwall test data. Figure 62 shows that the re-entry port configuration has the same trends as the plain endwall for the efficiency, APR, and AO mass flow. The maximum APR of about 2.2 is also the same between the plain and re-entry port configurations. However, the re-entry port reaches the maximum APR at a higher AO valve position of 0.5 compared to 0.1 for the plain endwall. This should imply a higher mass flow out the AO port when the maximum APR is reached, except that the AO mass flow is about the same between the re-entry and plain configurations for all AO valve positions. Also, the re-entry port endwall reached a higher maximum compression

efficiency of 75% compared to the 62% of the plain endwall. This is due to pressure waves from the re-entry port before AI pre-compressing the fresh air in the rotor before the primary compression wave from the EI port reaches the fresh air. The primary compression wave then compresses the fresh air further and directs it out the AO port. This causes the re-entry port to have a larger pressure rise for the same exhaust temperature and rotor speed compared to the plain endwall.

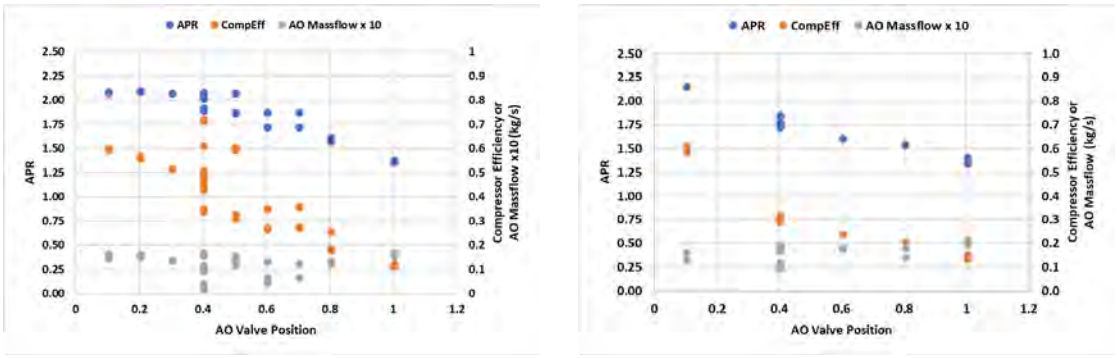

(a) Re-Entry Port **(b) Plain**

Figure 62. APR, Efficiency, and AO Mass Flow for 26,000 rpm Rotor Speed

Similar to the plain endwall data, further insight can be gained by coloring the data point by TEI and rotor speed. Figure 63 shows the compression efficiency and APR for the re-entry endwall configuration colored by rotor speed. The APR and compression efficiency follow the same overall trends as the plain endwall where both the APR and compression efficiency increase as the AO valve closes. Also, similar to the plain endwall, the rotor speed by itself does not have a large effect on the performance compared to the AO valve. However, the EPR for the re-entry configuration was less than one for nearly all the test conditions. This was a design choice of the re-entry configuration in order to promote scavenging of the engine cylinders[10] as discussed in Section 2.3.4. However, these pressure ratios may not be compatible with a real engine, and the performance of the re-entry configuration would likely suffer as a result. Some possible workarounds to the pressure ratio compatibility problem are

discussed in Section 5.2 and would apply to all the PWS configurations.

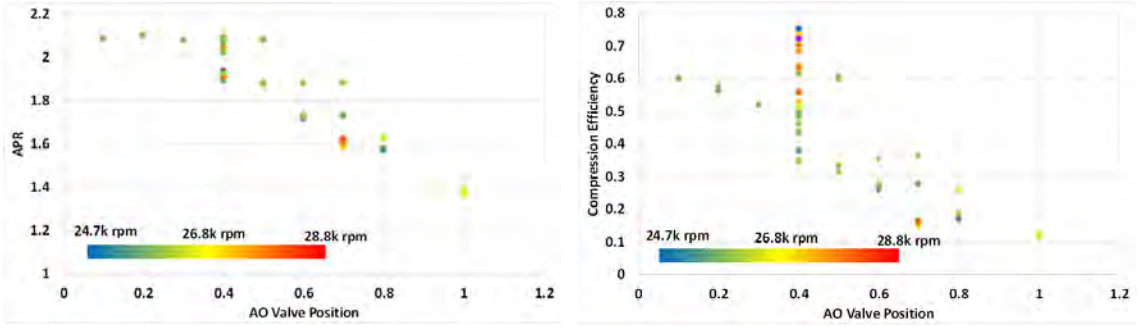

(a) APR **(b) Compression Efficiency**

Figure 63. Re-Entry Endwall Performance Colored by Rotor Speed

As with the plain endwall performance data, the performance data for the re-entry configuration was also colored by exhaust temperature shown in Figure 64. Similar to the plain endwall, increased exhaust temperature caused an increase in the compression efficiency and APR. The effect is most notable in the collection of data points at the AO valve position of 0.4.

Further insight can be gained by examining the data where the AO valve position is 0.4, as shown in Figure 65. In Figure 65, the APR and compression efficiency are plotted against TEI on the horizontal axis and colored by rotor speed. This shows how both temperature and rotor speed together affect the performance of PWS at a constant AO valve position. Figure 65a shows that an increase in the exhaust

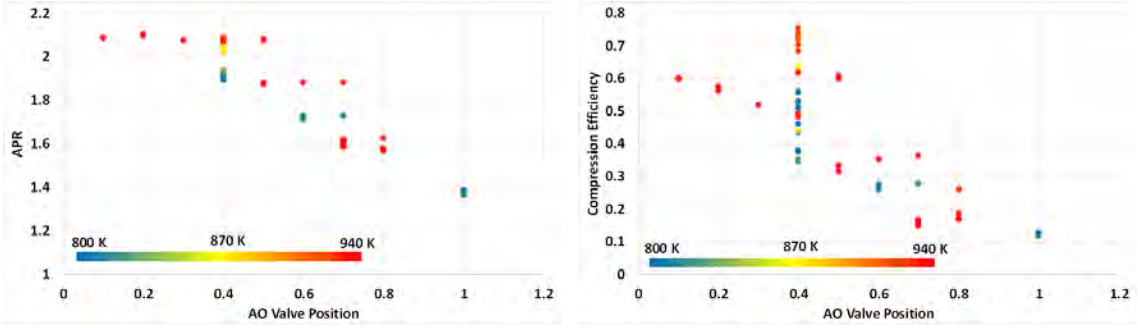

(a) APR **(b) Compression Efficiency**

Figure 64. Re-Entry Endwall Performance Colored by TEI

temperature increases the APR. The clusters of data points at 800 K and 925 K each have high and low rotor speed data points within the cluster, implying that the rotor speed does not have a significant effect on the APR compared to the exhaust temperature. Figure 65b shows that the exhaust temperature does have an effect on the compression efficiency, though the effect is not as pronounced as with the APR. The efficiency is sensitive to both the rotor speed and the exhaust temperature, and has the best performance when the rotor speed and temperature are matched. Also, the efficiency is highest when both the rotor speed and TEI are matched at a high-speed and high-temperature conditions. These trends match the engine coupled test results discussed in Section 3.4.1.1.

A sample of the re-entry data with the exhaust temperature limited to data points with an exhaust temperature of 811 K. This sample of data is plotted in Figure 66 with the plain endwall data that also meets the same criteria. In this data sample, the AO valve position ranged from 0.4 to 1.0 for the re-entry endwall and 0.4 to 1.5 for the plain endwall. For both the plain and re-entry data samples the rotor speed ranged from 23,500 rpm to 28,000 rpm. For this sample the re-entry and plain endwall had similar performance until the AO valve position reached 0.4. At this AO valve position, the re-entry endwall started to have significantly better performance than the plain endwall. At an AO valve position of 0.4 there began to be sufficiency

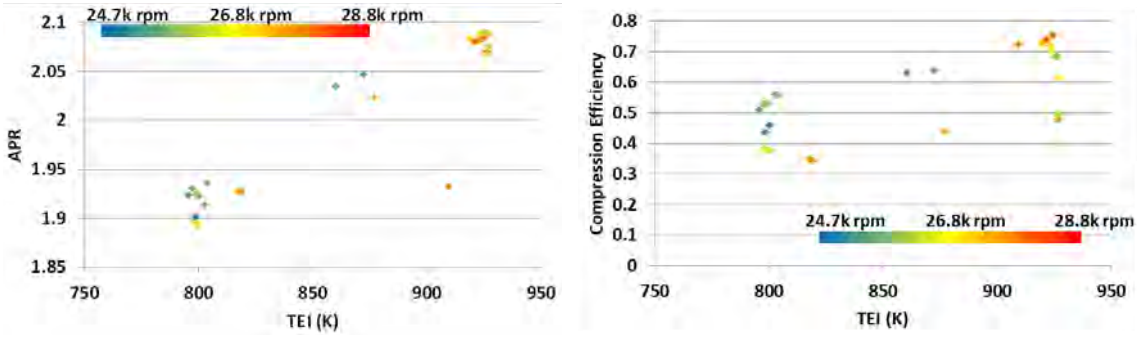

(a) APR **(b) Compression Efficiency**

Figure 65. Performance of the Re-Entry PWS for AO Valve Position of 0.4

back pressure at the AO port to properly set up the wave structure. Figure 66 shows that for very far from the design point, the re-entry and plain endwall have similar performance, at least at the sampled test conditions. However, when the PWS is operated much closer to the design point, the re-entry configuration has much better performance than the plain endwall for the sampled test conditions.

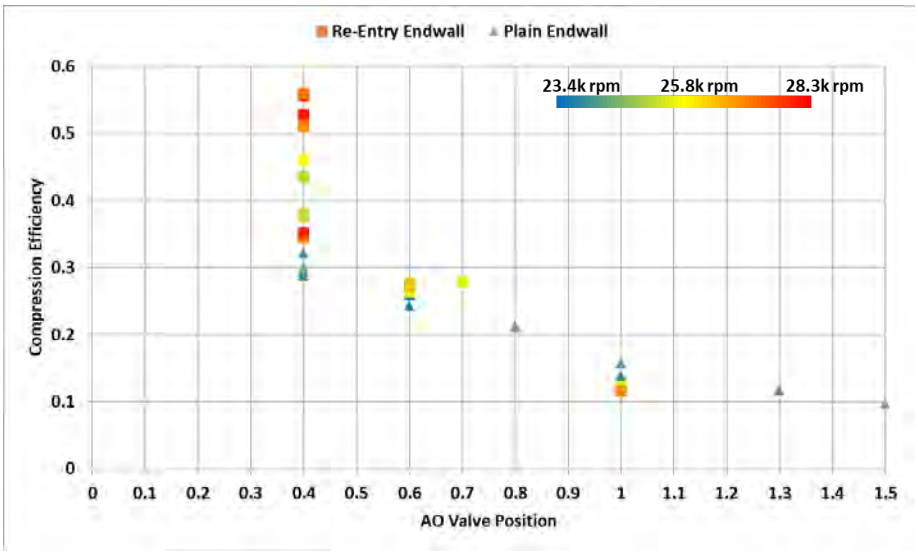

Figure 66. Re-Entry Endwall Performance Compared to the Plain Endwall for 811 K

A second sample for a constant rotor speed of 26,000 rpm was taken from the re-entry and plain endwall data. For this data sample, the exhaust temperature ranged from 800 K to 990 K and the AO valve ranged from 0.1 to 1.0. This data sample is plotted in Figure 67. As with the previous sample, the re-entry and plain endwalls had similar performance at AO valve positions of 0.8 or greater. Also, at the AO valve position of 0.4, the re-entry endwall performed much better than the plain endwall. For this specific sample, the plain endwall performance rises to match the re-entry endwall performance for an AO valve position of 0.1. At this AO valve position, the duct from the AO valve is nearly closed, and so a lot of back pressure can be built up in the AO port regardless of test condition or endwall configuration. At this test point, the effect of closing down the AO port overwhelmed any difference

in performance between the re-entry and plain endwall configurations.

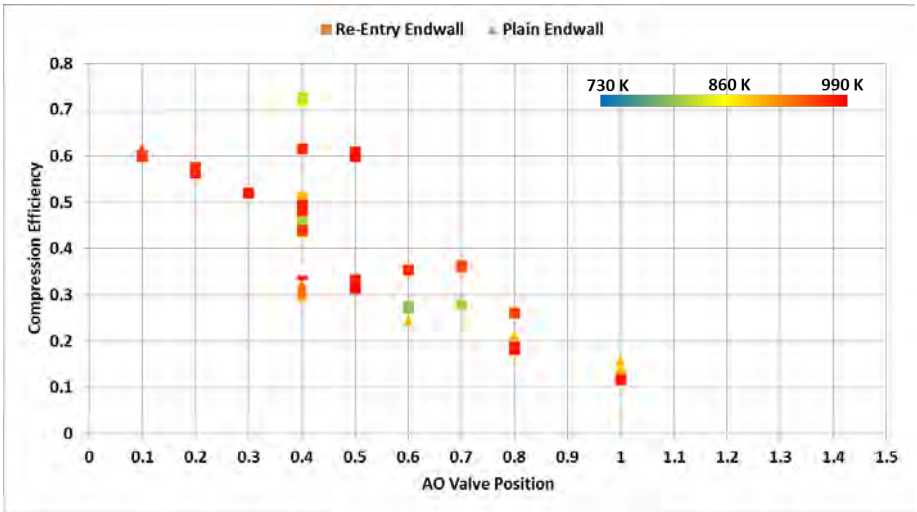

Figure 67. Re-Entry Endwall Performance Compared to the Plain Endwall for 26,000 rpm

4.6 Comparison of Configurations

In order to compare the performance of each configuration, the efficiency and pressure for each configuration were plotted. The data in each figure is for a constant rotor speed on 26,000 rpm and 0.0227 kg/s air mass flow through the burner. The exhaust temperature and AO valve position were varied in Figures 68 and 69, though only the change with AO valve position is shown. The re-entry endwall configuration performed better than the other configurations, as shown by the gray points in Figures 68 and 69. Conversely, the pocket endwall configuration did not perform significantly different than the plain endwall configuration. While the improved performance of the re-entry configuration was expected, the lack of performance improvement for the pocket configuration was unexpected. This may partially be due to a lack of pocket endwall data since only one test run was performed with the pocket endwall, so test conditions where the pockets improved performance may not have been hit in that test run. Additional test runs would fill out the test matrix and determine if the

pockets improve performance at other test conditions.

It is also possible that the pockets were not designed to be deep enough to have the desired effect of absorbing unwanted pressure waves. In order to test this idea, new endwalls would need to be designed and manufactured, which is a time and money intensive process. It is unlikely that the pocket depth is the cause of the unexpected performance since the pocket depth was scaled from the original Comprex® design. The final possible cause of the unexpected performance was an unknown error in the test rig setup that allowed for an unexpected amount of leakage and thus changed performance. Disassembly and careful reassembly of the test rig would mitigate this issue.

Table 3 shows the maximum performance of each endwall configuration compared to a turbocharger that is sized approximately for the same three cylinder diesel engine for which the PWS was originally sized. The performance data used for the comparison is the data collected and published by Mataczynksi et al. [30]. The re-entry configuration showed the best overall efficiency when the EPR was not limited to on or greater. However, when the performance analysis was limited to data with an EPR equal to 1 or more, the pocket endwall configuration had the best performance.

Overall, the performance of the PWS was not as expected. Previous testing had indicated that efficiencies as high as 50% could be achieved with the plain endwall configuration, even with an EPR greater than one. However, the highest efficiency

Table 3. Comparison of PWS Configurations with a Turbocharger[30]

	Maximum APR	Maximum Compression Efficiency
Garret GT06	2.6	65%
Plain Endwall	2.2	61%
Plain Endwall $EPR >= 1$	1.6	24%
Pocket Endwall	1.9	41%
Pocket Endwall $EPR >= 1$	1.8	35%
Re-Entry Endwall	2.1	75%
Re-Entry Endwall $EPR >= 1$	1.3	13%

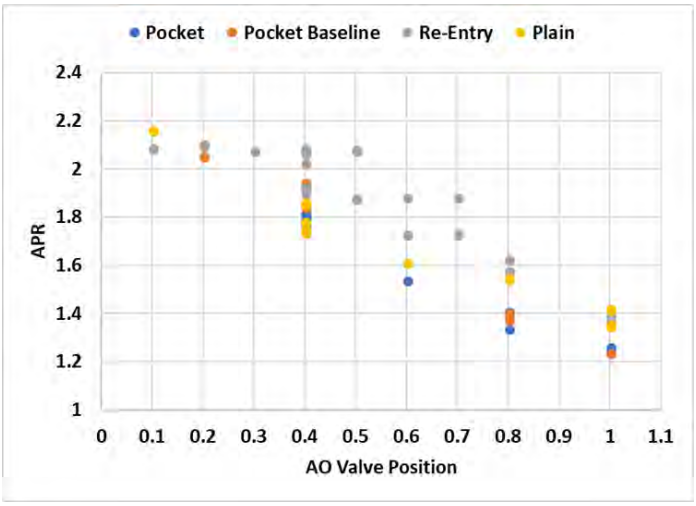

Figure 68. APR vs AO Valve Position for Each Endwall at 26,000 rpm Rotor Speed

observed during the open loop testing that had an EPR greater than one was 35% for the pocket endwall configuration. It is unknown what exactly caused the difference in performance between the previous testing and the current research as every effort was made to match the test configuration and to ensure the wave rotor was assembled correctly.

The pocket endwall configuration had the best performance of the three configurations when only the test points with EPR$\geq$1 are examined, as can be seen in Table 3. This supports the idea that the pockets improve the off design performance of the wave rotor as discussed in Section 2.3.3. The pocket endwall configuration may be the most promising for coupling to a real engine since it had the best performance when the EPR was limited to greater than one. Since the pocket endwall was not tested with the full test matrix, the maximum overall APR and compression efficiency presented in Table 3 are based on the limited data available. It is expected that the actual maximums are closer to the maximum values for the plain and re-entry endwall configurations.

The re-entry port configuration shows the greatest overall performance when the EPR was not restricted. The re-entry configuration was designed to have an EPR of

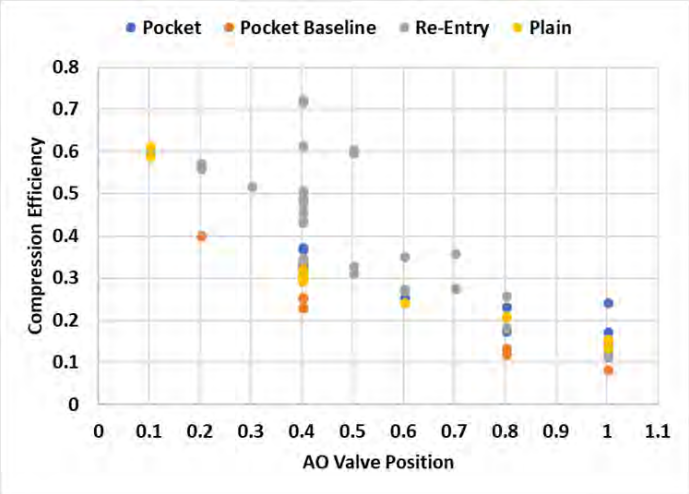

Figure 69. Compression Efficiency vs AO Valve Position for Each Endwall at 26,000 rpm Rotor Speed

less than one in order to promote scavenging of the cylinder. This design choice may render the re-entry configuration incompatible with an actual engine, though more likely the re-entry configuration would simply have reduced performance instead of becoming unusable. It may be possible to adjust the engine design parameters, such as the valve timing, to make the engine compatible with an EPR of less than one.

None of the configurations were able to match the pressure ratio achieved by the example turbocharger as measured by Mataczynski[30]. Some of the other turbochargers measured by Mataczynski had slightly lower maximum pressure ratios than the example used here. Though none of the PWS configurations matched the APR of the turbo charger, the plain endwall and re-entry endwall configurations came close. The plain endwall also came close to matching the turbocharger's efficiency while the re-entry endwall improved the efficiency over the turbocharger by about 11%. However, these maximum performance values for the PWS were with an EPR of less than one, which is not compatible with an actual engine. If the engine could easily be modified to be compatible with and EPR of less than one, then the PWS would be a competitive option for coupling with the diesel engine.

V. Conclusions

Reciprocating engines lose power as air density and pressure decrease with increased altitude. Traditionally, turbochargers and superchargers are used to compensate for the reduced ambient pressure. However, these mechanical compression devices suffer from reduced efficiency when scaled to fit small engines. One way to avoid the efficiency loss due to scaling is to use a wave rotor in place of the turbocharger or supercharger. A wave rotor avoids the efficiency losses at small scale since the hot exhaust gasses do work directly on the fresh air to compress it without any mechanical parts separating the flows. This research tested a wave rotor designed for a three cylinder diesel engine, including testing three different endwall configurations.

5.1 Review of Objectives

This research aimed to expand on the characterization of a pressure wave supercharger for an industrial diesel engine. This was accomplished by examining existing data and by open loop testing of the PWS. Different endwall configurations were also compared in order to determine what changes to the endwall design would be used to improve the PWS performance. The performance of the PWS was measured by calculating the compression efficiency and the boost pressure ratio. This research program attempted to achieve these goals by following these specific research objectives.

1. Establish baseline performance using the plain endwall to fill in gaps in previous open loop testing and confirm that the test rig worked as intended

2. Understand the performance impact of the pocket endwall configuration to the plain endwall to determine if the pockets increase the performance compared to the baseline configuration

3. Study the impact on performance of the re-entry port endwall configuration and compare to the plain endwall to determine if the re-entry port increases the performance compared to the baseline configuration

The test rig consisted of the wave rotor coupled to a burner in an open loop configuration. The plain endwall was tested first and established the baseline performance for comparison to the other configurations as well as confirming that the test rig worked as intended. Next the pocket endwall was briefly tested without the pockets machined into it in order to determine a baseline performance of that endwall so that the effect of adding pockets to the endwall could be isolated from any other effects. After the testing with the plain endwall and pocket baseline configuration was completed, the test rig was fitted with the re-entry endwall wave rotor. The re-entry endwall configuration was tested while the pocket endwalls were at the shop having the pockets cut in. The same test matrix that was used to test the plain endwall was also used for the re-entry port endwall. Finally, the re-entry endwall was replace with the pocket endwall after the pocket endwall came back from the shop.

The testing with the plain endwall confirmed that the test rig worked as intended and provided a good baseline for comparing the performance of the re-entry and pocket endwall configurations. Both the re-entry and pocket endwall configurations showed improved performance over the plain endwall configuration. The limited pocket endwall data showed an increase in compression efficiency over the plain endwall while achieving about the same APR as the plain endwall. The biggest advantage of the pocket endwall was that it had the best performance when the data set was limited to EPRS greater than one. The re-entry configuration showed both increased compression efficiency and APR. However, it also had the worst performance when the data set was limited to EPRs greater than one.

5.2 Recommendations

The wave cycle used by the wave rotors studied here show promise for possibly achieving performance similar to a turbocharger for small engines. However, the internally mounted bearings could not be sufficiently cooled and subsequently often overheated and failed. Therefore, it is recommended that an improved bearing mounting or cooling system be devised before continuing research with these wave rotors. The bearing mounting system may be improved by externally mounting the bearings to keep them separated from the PWS as it gets hot. Also, the winding of each port channel inside the endwall likely caused aerodynamic losses that reduced the performance of the PWS. The addition of the pockets required that the port ducts internal to the endwall turn sharply in order to keep the same overall endwall dimensions. Future endwall designs should attempt to minimize the aerodynamic losses by keeping the port channels as simple as possible. Both simpler port channels and an improved bearing system should be achievable in one endwall configuration.

Future research should focus on accurate testing of the wave structure cycle used in this research. This type of testing would use the same port locations and rotor diameter as the current design, but would refocus on testing just the wave rotor cycle instead of also attempting to make the overall wave rotor unit small enough to fit in an engine compartment. In conjunction with focus on isolating and testing the wave cycle, future research should take into account the mechanical aspect of the design. This would include accounting for thermal growth of the rotor as well as cooling the bearings. To place less load on the bearing cooling system, the rotor length could be increased, allowing the rotor speed to decrease. A decreased rotor speed would reduce the amount of friction generated heat which could increase the bearing life. Other options for research include finding alternate wave structures that may be more tolerant of EPRs greater than one.

Future research may also focus on wave rotors designed for smaller engines than what was tested in this research. As discussed in Section 2.1, small turbochargers for small engines lose efficiency and effectiveness as the size decreases. The 898cc engine used to size this wave rotor is about the size where an appropriately matched turbocharger starts to lose efficiency. For engines larger than about 1 L (1000 cc), it does not make sense to use a PWS since the PWS technology is relatively immature and turbocharger technology is well understood and readily available. Instead, engine sizes roughly in the 400cc to 600cc range may be a promising area for matching to a PWS instead of a turbocharger.

5.3 Summary

This research has shown that a PWS could be a viable option for supercharging small engines. However, there are some technical issues that would need to be solved before a PWS could be coupled to a real engine. The tests performed in this research uncovered a significant issue with the current PWS design, which is that the PWS performs best at engine pressure ratios that are not compatible with an actual engine. Addressing the technical issues presented here would allow future research to move the design of the PWS closer to integration with an engine.

There could be two possible solutions to address the issue of the engine pressure ratio. The first possible solution would be to find a alternate wave structure cycle that is more compatible with engine pressure ratios of one or higher. This would be a time intensive process since there are many different design choices that influence the performance of a particular wave structure cycle. Alternatively, future research should investigate whether or not the engine could be easily modified to be compatible with engine pressure ratios less than one.

Appendix A. Procedures

START UP

1. Confirm that the control panel in the control room is set correctly
    a. PDE water turned on – pushed in is on, light indicates active
    b. Propane ISO is on – pushed in is on, light on indicates fuel able to flow. Light should be off while the door is open
    c. Last Change One and Two are on – button out is on, light indicated fuel able to flow. Light should be of while door is open
2. Power on the compressor
    d. In the compressor room, turn on the power to the compressor
    e. Ensure the compressor bleed valve is closed
    f. Open the drain valve to allow any condensate to drain. Visually confirm no drainage (takes approx. 5-10 seconds) and close the drain valve
3. Power on the data acquisition system. 2 power strips the power supply
    g. One power strip supplies the can combustor DAQ via an always on 12v power supply and the second power strip
    h. The second power strip powers the PWS DAQ, the motor controller, and the variable power supply for the pressure transducers
    i. Set the variable power supply to 24 V and press the "Out" button to supply the pressure transducers with power
    j. Optional: Confirm that the DAQ and LabVIEW are communicating by connecting the controlling laptop to the DAW using a short Cat-5 cable and adjusting the AO valve. The electric motor can also checked for proper spin direction by supplying only enough voltage to spin the rotor (about 0.07 V for the LMT 1920 currently used).
        i. If rotor spins wrong direction, switch the connecting terminal of any two of the three wires connecting the rotor to the speed controller
    k. Confirm that the DAQs and controlling laptops for both the can combustor and wave rotor are communicating from the Control Room.
4. Open the water valve near the T-63 rig – confirm that water is coming out the drain tube under the T-63 platform
5. Confirm that the spark box on the T-63 rig is switched on and the Air TESCOM Power box is switched on.

6. Check that the sonic nozzle on the air line is the 0.201-inch diameter nozzle and the air line valve is open

    l. If this is the first run after the weekend, leave air line valve closed and instead open the butterfly bleed valve near the floor about half way. Then confirm all personnel are out of the bay, sound the horn, and close the bay. Start the air flow using the facility control in order to blow any debris out of the air system (approx. 10-20 seconds). Stop the air flow and reopen the bay, then close the butterfly valve and open the air line valve.

7. Confirm that the nitrogen bottles for the last chance valves and door interlock valves are open and have sufficient pressure (approx.. 100-150 psi)

8. Open the fuel bottles fully. Set the hydrogen pressure to 60 psi by adjusting the regulator.

9. Start the LabVIEW programs on each control laptop

    m. The can combustor control program is called "Brayton Rotor" and runs on the docked laptop.

    n. The wave rotor control program is called "WaveRotor-Kubota Closed Loop3" and is loaded as an executable on any laptop that has the LabVIEW 2015 Runtime Environment and the NI Measurement and Automation Explorer loaded, both available free from NI

    o. Confirm that the control programs are communicating with the DAQs by running the program and observing that the data fields populate with appropriate values

10. Confirm that the bay is empty and sound the horn

11. Close the bay door

RUNNING

1. Begin the air flow using the facility control computer.

2. As the air flow comes up, provide power to the rotor. Without power, the rotor will free-spin due to the air moving through it.

    a. Apply approx. 0.07 volts to start the rotor turning and then increase the supplied power until the target speed is reached, typically about 1.5 volts for 26,000 rpm on the LMT 1920 motor currently being used.

3. Confirm that the spark is turned on

4. Begin the flow of hydrogen by opening the last chance valve. Hydrogen flow rate is pre-set by the pressure regulator on the hydrogen bottle

b. Confirm hydrogen flow by observing a pressure increase at the hydrogen sonic nozzle on the burner control program

c. Confirm the hydrogen is lit by observing the temperature increase at the Burner Downstream Temperature field on the burner control program

5. After the hydrogen is ignited, begin the flow of ethylene by opening the last chance valve on the facility control program then opening the control valve in the control room

d. Confirm that the ethylene control knob is set to zero

e. Open the last chance valve on the facility control program

f. Slowly increase the ethylene flow until the ethylene ignites, as indicated by a sudden increase in burner downstream temperature, typically about 300-400 F

g. The spark ignitor can be turned off at this point, but hydrogen must still be flowing in order to maintain stable combustion

h. Slowly increase the ethylene flow until the desired temperature is achieved

i. NOTE: the burner downstream temperature is very sensitive to adjustments to the control valve and can take several seconds to reach steady state. Therefore, make slow and small adjustments to the ethylene flow rate and wait for the temperature to reach a steady state before making further adjustments

6. Once the desired burner temperature is reached, adjust the power to the motor to correct any speed deviations that are likely to occur.

7. Adjust the temperature, rotor speed, AO valve position, air mass flow, or any other parameters to collect the required data

8. When all data points are collected, shut down the ethylene and hydrogen fuel flows by closing the Last Chance valves.

9. Continue to flow air through the test rig to cool the components. When the temperature has reached an acceptable level, shut down the air flow and the bay can then be opened.

SHUTDOWN

1. General Overview: undo everything that was done in setup

2. Turn off the safety valves in the control room – Propane ISO and Last Chance One and Two, and PDE Water

3. Close the valves on the fuel bottles

4. Close the air line valve if no one else using the compressed air for the day
5. Close the water valve near the T-63 stand
6. Turn off the spark box and the Air TESCOM power
7. Disconnect the battery from the ESC and turn off the power to the second power strip
    a. Leave the first power strip on since this powers the battery charger
8. Connect the battery to the charger and use the auto charge LiPo setting to charge the battery.
    b. Battery is a 4 cell lithium polymer battery (4S LiPo) and takes approx. 2 hours to reach full charge
    c. Auto charge setting will automatically shut off when the desired charged is reached or when the preset time expires
9. If at end of day or if confirmed that no one else is using the compressors, turn of power to the compressor, fully open compressor bleed valve, and open drainage valve half way

Appendix B. Bearing Speed Limit and Other Lessons Learned

One of the issues that has plagued wave rotor research at AFIT and AFRL is that the bearings used to hold the shaft frequently fail, requiring the test to stop and the bearings to be replaced. Because of the way the rotating assembly is designed and mounted in the cold endwall, the entire rotor, shaft, and cold endwall assembly needs to be disassembled in order to replace the bearings. In order to increase the robustness of the design, future wave rotor work should examine how traditional automobile turbochargers mount and cool the bearings and how this could be adapted for a wave rotor design.

Equation 16 shows how the limiting bearing speed is calculated[31]. In Equations 16 and 17, B is the bore diameter of the bearing, and D is the outer diameter of the bearing so that d_m is the average of the bore and outer diameter. The Speed Limit Factor is dependent on the type of bearing, the bearing material, and also the type of lubrication used. It should be given by the bearing manufacturer. The resulting N_{lim} is the limiting speed for that particular bearing. This limiting speed is based solely on the geometry of the bearing. Other bearing design features may further reduce the permissible operating speed, such as the type of lubrication used or if the bearing is sealed or not.

$$d_m = \frac{B + D}{2} \tag{16}$$

$$N_{lim} = \frac{SpeedLimitFactor}{d_m} \tag{17}$$

Based on experience working with the wave rotor test rig, it became apparent that several updates to the design would greatly improve the ease of testing. Firstly, the PWS needs to be designed with maintainability built in from the beginning. Specifically, bearing integration needs to be redesigned. The bearings need to be

open instead of sealed and cooled with a circulating oil bath, similar to how bearings in turbochargers are cooled. This will allows for much higher running speeds and will increase bearing life significantly. Alternatively, the cold endwall could be redesigned to allow for the bearings to be easily changed. This is not the optimal solution due to the cost of constantly replacing bearings, the downtime required to replace the bearings, and the likely possibility of bearing failure during a test run that cuts the test run short.

Also, the control program and data acquisition system were cumbersome to work with. This made it difficult to update the control program when a change to the test rig was made and to troubleshoot the instrumentation when a sensor wasn't working correctly. To improve the control program, it would be necessary to rewrite the program from scratch to have the same functionality but a more streamlined and straightforward structure. This would not be a difficult task, but would take a lot of time. Rewriting the control program would also allow for the two control programs and data acquisition systems to be consolidated and redundancies eliminated.

As mentioned in Chapter III, the PWS used a battery to spin the electric motor that spun the rotor. This worked well to control the rotor speed, however, limitations in battery life limited the test time to about 45 minutes. While the test duration was typically limited by the bearing life, battery life was a concern. It is possible to have spare batteries. Spare batteries were on hand to replace the depleted battery so that testing could continue, but the test must be stopped temporarily to open the test bay and swap the depleted battery for the fresh one. Also, it is possible to procure a battery with more storage capacity. However, this may be cost-prohibitive since high-quality and specialty batteries can be expensive. The optimal solution may be to wire the electric motor and speed controller directly to the power supply for the data acquisition system. This would require creating some custom connections and

research into the current and voltage requirements and outputs of the motor, ESC, and power supply. Wiring the motor this way would mean that the test time is only limited by the ability of the bearings to run at the test conditions for extended periods of time.

To address the problems with bearing failure, the endwall could be redesigned to use an open bearing with a recirculating oil bath instead of a sealed bearing. The use of an open bearing would require a high quality shaft seal to separate the gasses in the wave rotor from the bearings as well as a careful design to make sure the lubricating oil can circulate freely without foaming. However, these requirements should be somewhat easy to meet since this is similar to the bearing cooling system used in commercially available turbochargers. The other alternative is to remove the bearing mount location from the endwall so that the bearing is not exposed to the hot environment in the PWS. This solution would also require a good shaft seal, but the consequences of a shaft seal failure are much less severe in this case.

Bibliography

1. Japikse, D., "Efficiency: The Silent Partner of Machine Performance," *Turbomachinery Symposium*, College Station, TX, 1982.

2. Akbari, P., Nalim, R., and Mueller, N., "A Review of Wave Rotor Technology and Its Applications," *Journal of Engineering for Gas Turbines and Power*, Vol. 128, No. 4, 2006, pp. 717–735.

3. Spinner, F. W. and Jaussi, F. A., "The Fully Self-Regulated Pressure Wave Supercharger Comprex for Passenger Car Diesel Engines," *The Third International Conference on Turbocharging and Turbochargers*, Birdcage Walk, London, May 1986.

4. Lei, Y., Zhou, D. S., and Zhang, H. G., "Investigation on Performance of a Compression-Ignition Engine with Pressure-Wave Supercharger," *Energy*, Vol. 35, No. 1, January 2009, pp. 85–93.

5. Mataczynski, M. R., *Design and Simulation of a Pressure Wave Supercharger for a Small Two-Stroke Engine*, Master's thesis, Air Force Institute of Technology, 2014.

6. Mataczynski, M. R., McClearn, M. J., Schauer, F. R., Paxson, D. E., and Hoke, J. L., "Design and Testing of a Small Pressure Wave Supercharger for an Industrial Diesel Engine," *55th AIAA Aerospace Sciences Meeting*, No. AIAA 2017-1624, Grapevine, TX, January 2017.

7. McClearn, M. J., *Design, Manufacturing, and Testing of a Small Through-Flow Wave Rotor for Use Within the Brayton Cycle*, Master's thesis, Air Force Institute of Technology, 2016.

8. Haidinger, C., Kriegler, W., Millward-sadler, A., and Eder, P., "Feasibility and Design Analysis of a Pressure Wave Supercharger Adaption on a 600 cm 3 Spark Ignited Engine," 2017.

9. Smith, B. D., *Scaling Study of Wave Rotor Turbo-Normalization of a Small Internal Combustion Engine.*, Master's thesis, Air Force Institute of Technoloty, 2012.

10. Aerodyn Combustion LLC, "Final Report: Oct 21, 2016 revised. Wave Rotor Reentry Port Project PO1601587," Report from Aerodyn Combustion to Innovative Scientific Solutions. Stored on AFRL shared drive.

11. Chan, S. and Liu, H., "Defining the Thermodynamic Efficiency in a Wave Rotor," *Journal of Engineering for Gas Turbines and Power*, Vol. 138, No. 11, 2016, pp. 112601.

12. "Indirect Injection vs Direct Injection," `http://www.dieselhub.com/tech/idi-vs-di.html`, 2009, Accessed: 2017-10-01.

13. Schruf, G. M. and Kollbrunner, T. A., "Application and Matching of the Comprex Pressure-Wave Supercharger to Automotive Diesel Engines," *Society of Automotive Engineers International Congress & Exposition*, No. 840133, Detroit, MI, 1984.

14. Kubota Engine American, *Kubota Super Mini Series D902-E4B*.

15. Lapp, K. P., *Design and Testing of a Micro-Scale Wave Rotor System*, Master's thesis, Air Force Institute of Technology, 2017.

16. Gyarmathy, G., "How Does the Comprex Pressure-Wave Supercharger Work?" *Society of Automotive Engineers International Congress & Exposition*, No. 830334, Detroit, MI, 1983.

17. Mataczynski, M. R., Paxsion, D. E., Polanka, M. D., and Hoke, J. L., "Performance and Design Improvements for a Small Scale Pressure Wave Supercharger," *54th AIAA Aerospace Sciences Meeting*, No. AIAA 2016-0768, San Diego, CA, January 2016.

18. Anderson, J. D., *Modern Compressible Flow with Historical Perspective*, McGraw-Hill, New York, NY, 2003.

19. Smith, B. D., Polanka, M. D., Paxson, D. E., and Hoke, J. L., "Scaling Study of Wave Rotor Turbo Normalization of an Internal Combustion Engine," *48th AIAA/ASME/SAE/ASEE Joint Probulsion Conference and Exhibit*, No. AIAA 2012-3837, 2012.

20. Mataczynski, M. R., Polanka, M. D., Paxson, D. E., and Nees, J. B., "Testing and Simulation of a Small-Scale Pressure Wave Supercharger," *53rd AIAA Aerospace Sciences Meeting, Kissimmee, FL*, No. AIAA 2015-1345, January 2015.

21. Reinhart, J. T., Beasley, B. A., Hoke, J. L., McClearn, M. J., and Schauer, F. R., "Experimental Observations of a Small-Scale Pressure Wave Supercharger Coupled to a Compression Ignition Engine," *56th AIAA Aerospace Sciences Meeting*, Kissimmee, FL, 2018.

22. Paxson, D. E., "A General Numerical Model for Wave Roter Analysis," Tech. rep., NASA Glenn Research Center, 1992, NASA Technical Memorandum 105740.

23. Paxson, D., Wilson, J., and Welch, G., "Comparison Between Simulated and Experimentally Measured Performance of a Four Port Wave Rotor," *43rd AIAA/ASME/SAE/ASEE Joint Propulsion Conference & Exhibit*, No. AIAA 2007-5049, Cincinnati, OH, 2007.

24. Kurec, K. and Piechna, J., "Numerical and experimental investigations of pressure changes in a stationary passage of a pressure wave exchanger," 2016.

25. Paxson, D. E., 2017, Personal Communication about Endwall Pockets.

26. Kerr, J., "Direct vs. Port Injection," `http://thechronicleherald.ca/wheelsnews/26226-direct-vs.-port-injection`, 2011, Accessed: 2017-10-2.

27. Baines, N. C., *Fundamentals of Turbocharging*, Concepts NREC, White River Junction, VT, 3rd ed., 2005.

28. Curless, T., *Turbochargers: Theory, Installation, Maintenance & Repair*, TAB Books Inc., Blue Ridge Summit, PA, 1st ed., 1985.

29. Moffat, R. J., "Describing the uncertainties in experimental results," *Experimental Thermal and Fluid Science*, Vol. 1, No. 1, 1988, pp. 3 – 17.

30. Mataczynski, M. R., Litke, P., Naguy, B., and Baranski, J., "Characterization of Small-Scale Turbochargers for Unmanned Aerial Systems," *SAE/JSAE 2016 Small Engine Technology Conference and Exhibition*, 2016.

31. American Roller Bearing Compandy, "Bearing Speed Calculation - Bearing Speed Limit Factors," `https://www.amroll.com/speed-limits.html`, 2018, Accessed: 2018-05-20.

REPORT DOCUMENTATION PAGE

Form Approved
OMB No. 0704–0188

1. REPORT DATE *(DD–MM–YYYY)*	2. REPORT TYPE	3. DATES COVERED *(From — To)*
13–09–2018	Master's Thesis	Sept 2016 — Sept 2018

4. TITLE AND SUBTITLE

INVESTIGATION OF A PRESSURE WAVE SUPERCHARGER FOR AN INDUSTRIAL DIESEL ENGINE

5a. CONTRACT NUMBER

5b. GRANT NUMBER

5c. PROGRAM ELEMENT NUMBER

6. AUTHOR(S)

Brian A. Beasley

5d. PROJECT NUMBER

5e. TASK NUMBER

5f. WORK UNIT NUMBER

7. PERFORMING ORGANIZATION NAME(S) AND ADDRESS(ES)

Air Force Institute of Technology
Graduate School of Engineering and Management (AFIT/EN)
2950 Hobson Way
WPAFB OH 45433-7765

8. PERFORMING ORGANIZATION REPORT NUMBER

AFIT-ENY-MS-18-S-055

9. SPONSORING / MONITORING AGENCY NAME(S) AND ADDRESS(ES)

AFRL/RQTC
1790 Loop Rd
WPAFB OH 45433-7765
DSN 785-6462, COMM 937-255-6462
Email: frederick.schauer@us.af.mil

10. SPONSOR/MONITOR'S ACRONYM(S)

AFRL/RQTC

11. SPONSOR/MONITOR'S REPORT NUMBER(S)

12. DISTRIBUTION / AVAILABILITY STATEMENT

DISTRIBUTION STATEMENT A:
APPROVED FOR PUBLIC RELEASE; DISTRIBUTION UNLIMITED.

13. SUPPLEMENTARY NOTES

This material is declared a work of the U.S. Government and is not subject to copyright protection in the United States.

14. ABSTRACT

Internal combustion engines suffer from decreased performance as altitude is increased. This performance decrease can be overcome by increasing the pressure in the engine's intake manifold. Typically, this is accomplished with a turbocharger or supercharger. However, mechanical compression devices such as these suffer from decrease compression efficiency as the size of the device decreases. The size of the compression device scales with the amount of mass flow through the device, and the amount of mass flow is proportional to the size of the engine. This means a small turbocharger for a small engine is less efficient than a larger turbocharger coupled with a larger engine. An alternative means to compress fresh air sent to the engine is a wave rotor. The wave rotor avoids the efficiency loss of small mechanical compression devices by transferring energy from the exhaust gas to the fresh air by means of pressure waves. This research characterized the performance of a wave rotor sized for a 898cc industrial diesel engine. The wave rotor was initially tested while coupled to a burner instead of an engine in order to match and compare with previous testing. The results showed that the wave rotor had a maximum compression efficiency of 60% and that the efficiency depended on the exhaust temperature and rotor speed. The efficiency also depended heavily on the relationship between exhaust temperature and rotor speed since the rotor performance depends on the proper matching of these properties. Three different endwall configurations were also tested and compared. The results of the endwall comparison show that adding pockets to the endwalls increases the efficiency of the wave rotor at both on design and off design point conditions.

15. SUBJECT TERMS

Wave Rotor, Pressure Wave Supercharger, Diesel Engine, Performance

16. SECURITY CLASSIFICATION OF:			17. LIMITATION OF ABSTRACT	18. NUMBER OF PAGES	19a. NAME OF RESPONSIBLE PERSON
a. REPORT	b. ABSTRACT	c. THIS PAGE			Dr. M. D. Polanka, AFIT/ENY
U	U	U	U	129	19b. TELEPHONE NUMBER *(include area code)* (937) 255-3636, x4714; marc.polanka@afit.edu